Investigating an Inverse Finite Element Approach for Characterising Soft Materials

by

Franciena Helena Bresler

Thesis presented in partial fulfilment of the requirements for the degree of Master of Engineering (Mechanical) in the Faculty of Engineering at Stellenbosch University

Supervisor: Dr JH. Muller
Co-supervisor: Prof. G. Venter

March 2020

Declaration

By submitting this thesis electronically, I declare that the entirety of the work contained therein is my own, original work, that I am the sole author thereof (save to the extent explicitly otherwise stated), that reproduction and publication thereof by Stellenbosch University will not infringe any third party rights and that I have not previously in its entirety or in part submitted it for obtaining any qualification.

Date: March 2020 .....

Abstract

Investigating an Inverse Finite Element Approach for Characterising Soft Materials

FH. Bresler

Department of Mechanical and Mechatronic Engineering,
University of Stellenbosch,
Private Bag X1, Matieland 7602, South Africa.

Thesis: MEng (Mech)

March 2020

Micro-indentation was investigated as a method for characterising soft materials. This research characterised a soft silicone rubber using an inverse finite element (FE) approach with six different indentation tests. Four tests consisted of a cylindrical indenter, with the variability factors being the number of indenters and orientation of the indenter. Two tests consisted of a spherical indenter, with the difference between the tests being the number of indenters used. Each indentation test consisted of two FE models, one containing a known Mooney-Rivlin three parameter material model and one which needed characterisation. MSC Marc Mentat (2019) was used to perform all FE analysis. The remeshing feature within Marc was implemented within the FE analysis to minimise the element distortion present when deforming a non-linear material to a complex deformation field. Python was used to develop a numerical pipeline, which controlled and linked the different software and procedures. Two optimisation algorithms were investigated, Sequential Quadratic Programming (SQP) and Sequential Linear Programming (SLP). Radial Basis Functions (RBF) were used to interpolate the FE analysis results. The root mean square (RMS) error of the displacement fields, was minimised as objective function within the optimisation procedure. It was found that one cylindrical indenter, applied in a diagonal orientation across a square test sample, obtained the best material model using the SQP optimisation algorithm. From the observations within the results, it was concluded that a material model either matched the displacement field or the engineering vs. stretch nearly perfectly, but not both simultaneously.

Uittreksel

Die Ondersoek van ’n Inverse Eindige Element Metode om Sagte Materiale te Karakteriseer

(“Investigating an Inverse Finite Element Approach for Characterising Soft Materials”)

FH. Bresler

Departement Meganiese en Megatroniese Ingenieurswese,
Universiteit van Stellenbosch,
Privaatsak X1, Matieland 7602, Suid Afrika.

Tesis: MIng (Meg)

Maart 2020

Mikro-indentasie is ondersoek as ’n metode om sagte materiale te karakteriseer. ’n Sagte silikoonrubber is ondersoek waarvan die meganiese gedrag gekenmerk is deur ses verskillende indentasietoetse te gebruik. Vier toetse het bestaan uit ’n silindriese indentator, met die veranderlikheidsfaktore, die aantal indentators en oriëntasie van die indentator. Twee toetse het bestaan uit ’n sferiese indentator, met die aantal indentators, die verskil tussen die toetse. Hierdie tesis was gebaseer op twee eindige element modelle per indentasie toets. Een met ’n bekende materiaalmodel en een wat gekarakteriseer moet word. ’n Inverse eindige element benadering is gebruik om die een eindige element model volgens die bekende materiaal veranderlikes te karakteriseer met behulp van die Mooney-Rivlin drie parametermodel. Die "remesh"metode, vanuit MSC Marc Mentat (2019), is binne die eindige elementanalise geïmplementeer, om die element verdraaiings wat voorkom in ’n komplekse vervormingsveld van ’n nie-lineêre materiaal, tot ’n minimum te beperk. ’n Numeriese pyplyn is ontwikkel om die verskillende sagteware en metodes met mekaar te verbind. Twee beperkte gradiënt gebaseerde optimeringsalgoritmes is vir elke indentasietoets ondersoek naamlik, Sekwensiële Kwadratiese Programmering (SQP) en Sekwensiële Lineêre Programmering (SLP). ’n Latin Hypercube (LHC) -ontwerp van eksperimente is gebruik om uitvoerbare veranderlikes vir die optimaliseringsprosedure te verkry. ’n Radiale basisfunksie (RBF) het die resultate vanaf die twee eindige element analise geïnterpoleer om bymekaar te pas. Die fout, bepaal vanaf die verskil tussen die twee eindigende element modelle se verplasingsvelde, word geminimaliseer

tydens die optimaliseringsprosedure. Daar is gevind dat een silindriese indentator, toegepas in ’n diagonale oriëntasie oor ’n vierkantige toetsmonster, die beste materiaalmodel verkry met behulp van die SQP-optimeringsalgoritme. ’n Finale gevolgtrekking vanuit die resultate het voorgestel dat die materiaal model of die verplasingsveld perfek pas of die ingenieurs stress teenoor strek, maar nie albei gelyktydig nie.

Acknowledgements

I would like to express my sincere gratitude to the following people:

Thank you to Dr Cobus Müller, for the guidance and support throughout the project. Thank you for challenging me with difficult questions, concepts and methods. It improved my knowledge and understanding of the different techniques, methods and literature required to complete the project to the level it is presented.

Thank you Prof. Gerhard Venter, for your never-ending guidance, availability and support throughout the whole project. I acquired a lot of technical knowledge and a better understanding of the FE analysis field. Without you, the numerical pipeline would have taken much longer to develop and not close to the efficiency it did in the end.

I would like to thank both Dr Müller and Prof. Venter for taking me as a student and welcoming me to Stellenbosch University by making me a part of the respective research groups. Thank you both for giving me this opportunity by sponsoring my study fees.

Thank you to Mr. Gerrit Visser from SIMTEQ Engineering, for your knowledge and advise regarding the simulation issues encountered with Marc. Thank you to Mr. Paul Naudé and his team from SIMTEQ Engineering for providing myself and some colleagues with offline licenses for the different software during the loadshedding when the servers were not available.

Thank you to my family back home for all your long-distance love and support and continuous motivation. Thank you Kaitlyn, for being my support line during the late nights in the office and your amazing friendship.

Lastly, thank you to our Heavenly Father for giving me the strength and ability to complete my master's degree.

Dedications

Hierdie tesis word opgedra aan mamma en pappa. Baie dankie vir julle oneindige liefde, ondersteuning en motivering deur al die jare. Sonder julle was alles wat ek bereik het, nie moontlik nie.

Contents

List of Figures

List of Tables

Chapter 1

Introduction

1.1 Background

The classical way of characterising a material is by means of uni-axial and biaxial tensile and compression tests. Soft materials have been characterised with these methods, but have shown to provide sub-optimal results in small sample sizes. Soft materials, such as biological tissue, generally have sample sizes of 10 mm x 10 mm or smaller, which do not feasibly work in conjunction with the clamping methods associated with uni-axial and biaxial tensile tests (Holzapfel and Ogden, 2009). The clamping methods cause unwanted stress concentrations in the captured data and lead to inaccurately derived stress vs. strain curves.

Vastmans *et al.* (2018) and Abbasi *et al.* (2016) both used biaxial tensile testing to characterise respective biological tissue. A BioTester testing rig, obtained from CellScale Biomaterials Testing, was used for the physical tensile testing. The tissue samples mounted in the BioTester use small scale hooks, or rakes as described by the manufacturers, to secure the samples in place by penetrating the boundaries of the samples with these hooks. Vastmans *et al.* (2018) used the Gasser-Ogden-Holzapfel (GOD) model for the parameter fitting procedure. The GOD model aims to serve as a constitutive model for three-dimensional curve fitting procedures of arterial walls (Holzapfel *et al.*, 2000). One of the parameters predicts the fibre orientation within the biological tissue sample. The results obtained from Vastmans *et al.* (2018), found it difficult to fit this parameter due to the penetrating rakes causing inhomogeneity within the captured data.

Liu *et al.* (2009) conducted nanoindentation tests, using a circular flat punch as indenter, to characterise polymer gels through inverse finite element (FE) analysis. The proper indenter diameter and shape play a big role in determining the viscoelastic material parameters of soft tissue. The material modulus is one of the main factors which needs to be considered when deciding on an indenter shape and diameter. Liu *et al.* (2009) recommended that a stiff material with a modulus of approximately 100 kPa and above, can yield acceptable results with an indenter diameter of around 500 μm. Softer materials with a decrease in mod-

ulus around 1 kPa, will deliver better results with indenter diameters closer to 2 mm. This recommendation was evidently true in the results, since the error between the simulated and experimental tests increased with a factor of approximately five as the material modulus increased with the indenter diameter increasing from 750 μm to 1750 μm.

The characterisation of soft materials, especially biological tissue, has been an increasing interest over the last two decades and there is an increasing interest in using indentation to characterise the mechanical properties. The studies can be used as valuable guidance in investigating further possible contributions in this field. An example is to investigate how different indenter shapes and orientations and number of these indenters, perform in characterising soft materials. Another possibility is to use inverse FE analysis to determine the predictability of the material models obtained from these different indenters, in not only the compression but tensile range as well. This thesis aimed at investigating both these examples as a contribution to the research in using indentation to characterise the mechanical response of soft materials. The methods, indenters and constitutive model used in this thesis, will be discussed in detail.

1.2 Aim and Objectives

This thesis aimed to develop an inverse FE approach for characterising soft materials on mm scale samples, using micro-indentation to generate a complex strain field.

In order to accomplish the aim of this thesis, the following objectives need to be met:

- Define the indenter shape and orientation of each indentation test, as well as the number of indenters.
- Create two identical FE models for each test.
- Create the numerical pipeline to link all the software.
- Determine which indentation method was the best according to the best objective function.
- Extrapolate each model into different strain regions to determine the predictability of the material model.

A soft silicone-rubber, Smooth-Sil-950, was used as the soft material to test the approach. This silicone-rubber has been investigated as a possibility for use in soft robotics and will therefore serve as a good test material for the approach in this thesis (Case *et al.*, 2015). Soft materials and the silicone-rubber used in this thesis, have a non-linear material behaviour; it was thus decided to use MSC

Marc Mentat (2019) as the non-linear FE solver for the FE simulations. Six indentation methods were tested, two using a spherical indenter and four using a cylindrical indenter. Between the six methods the orientation and the number of indenters were the variability factors. The inverse FE approach designed in this thesis was unique in the sense that no physical experimental set-up or data was present. Each indentation method had two FE models, one serving as the "Experimental" model and one being the "Numerical" model used during the optimisation method. Two gradient based, constraint optimisation algorithms were used for each indentation method, Sequential Linear Programming (SLP) and Sequential Quadratic Programming (SQP). Each method's material properties were described using the Mooney-Rivlin three parameter constitutive model. This model has been proven to have the most convenient accuracy with least computation time (Wex *et al.*, 2015; Tobajas *et al.*, 2016). Design Optimization Tools (DOT) was obtained as a wrapper to be used within Python for the optimisation procedure. Python (v3.6.3) was the coding language used within Visual Studio Code to develop and control the numerical pipeline for optimisation and linking the different software.

1.3 Thesis Outline

This thesis consists of seven chapters, which follow the logical steps used to obtain the aim and objectives set out in the section above. Chapter 2 contains the necessary research and concepts needed to reach the aim set out for this thesis. Chapter 3 explains the necessary FE procedures and methods used to obtain the acceptable FE models for the inverse FE approach. Chapter 4 explains in detail the numerical pipeline created to implement the inverse FE approach. Within chapter 5 the uni-axial compression method is explained for the Mooney-Rivlin three parameter model and a validation test was done for each of the indentation tests between the FE models. Chapter 6 discusses the results obtained from the indentation tests. The thesis is concluded with chapter 7, providing a general discussion on the results, conclusion and some advise for future work.

Chapter 2

Literature and Concepts

2.1 Silicone Rubber

The soft materials mentioned thus far can be defined as a material which have large elastic deformation characteristics at relatively low-loading rates (hyper-elastic and non-linear) and are considered isotropic and incompressible (Kim *et al.*, 2012). In soft robotics, elastomers are chosen for their highly deformable, stretchable and non-linear behaviour, which matches the definition of soft materials in this thesis (Case *et al.*, 2015). One of the these elastomers is the silicone-rubber Smooth-Sil-950 from AMT composites. Soft biological tissue is considered hyper-elastic, non-linear and anisotropic, but is modelled mostly as isotropic for characterisation methods (Tobajas *et al.*, 2016; Wex *et al.*, 2015). Soft biological tissue can therefore also be classified as a soft material and be considered for characterisation in future studies. Chai *et al.* (2014) investigated the stiffness of different atherosclerotic plaques within the different types of arteries in the human body. The results varied from <10 kPa within the aortic artery, to as high as 5 MPa in the carotid artery. Smooth-Sil-950 possesses a stiffness of 1.88 MPa (Smooth-On, 2012). It can be assumed that the Smooth-Sil-950 possesses the equivalent definition of softness as these atherosclerotic plaques. Therefore, using Smooth-Sil-950 as test material will allow for a reasonable indication if the proposed indentation tests in this thesis can be applied to biological tissue for characterisation (Holzapfel, 2016). Within this thesis the silicone-rubber will be characterised from −60% to 300% strain, which is 0.4 to 3.0 stretch. This range will serve as a wide description of how well the sets of material model parameters obtained from the different indentation tests, predict the behaviour of the silicone-rubber.

2.2 Material Models

Since hyper-elastic materials have exhibited non-linear behaviour between load and deformation, linear stress-strain theory cannot accurately describe these

materials' behaviour under a load. This was proven through a series of measurements of stress-strain relationships from experimental data by Mooney (1940) and Rivlin (1948). The famous Mooney-Rivlin material model was developed using a strain-energy density function (W) to describe the mechanical behaviour of non-linear materials through energy terms. It was Mooney (1940) who proposed the original strain energy density function in terms of the principle stretches, the modulus of rigidity and a new elastic constant. It was only later that Rivlin (1948) described the function in terms of Cauchy-Green tensor invariants. Over the last century, many different hyper-elastic material models have been developed to obtain a better curvature fit over a wider strain range. It was concluded that no single model can be considered the best for all materials, but rather each hyper-elastic material is unique and that different material models describe different hyper-elastic materials better (Wex *et al.*, 2015; Tobajas *et al.*, 2016). The strain-energy density function can be described in terms of the strain invariants as:

$$W = W(I_1, I_2, I_3) \tag{2.1}$$

where:

$$\begin{aligned} I_1 &= \lambda_1^2 + \lambda_2^2 + \lambda_3^2 \\ I_2 &= \frac{1}{\lambda_1^2} + \frac{1}{\lambda_2^2} + \frac{1}{\lambda_3^2} \\ I_3 &= (\lambda_1 \lambda_2 \lambda_3)^2 \end{aligned} \tag{2.2}$$

where λ_1, λ_2 and λ_3 represent the principle stretches. If the material is assumed to be incompressible, $I_3 = 1$ and Eq. 2.1 becomes:

$$W = W(I_1, I_2) \tag{2.3}$$

The principle Cauchy stresses can be expressed next as:

$$\sigma_i = \lambda_i \frac{\partial W}{\partial \lambda_i}, \quad i = 1,2,3 \tag{2.4}$$

Viljoen (2018) aimed to find material coefficients for Smooth-Sil-950 through three different experimental tests namely, uni-axial tensile testing, biaxial bubble inflation tests and unconstrained uni-axial compression tests. The Mooney-Rivlin two parameter model failed to produce feasible results for the stress state in all three tests. The final decision was between the Mooney-Rivlin three parameter model and the Ogden three parameter model. The Ogden three parameter model failed to produce feasible results for the uni-axial compression test. The Mooney-Rivlin three parameter model failed to produce feasible results for the uni-axial tensile test without forcing the model parameters to take on positive values. The final conclusion was that the Mooney-Rivlin three parameter model obtains the best results for all three tests, given that the initial parameters are valid. Therefore it was decided to only use the Mooney-Rivlin three parameter hyper-elastic constitutive model during this thesis, with Viljoen (2018) as reference for material parameters.

The Mooney-Rivlin three parameter model can be described using the strain-energy function as:

$$W = C_{10}(I_1 - 3) + C_{01}(I_2 - 3) + C_{20}(I_1 - 3)^2 \tag{2.5}$$

where C_{10}, C_{01} and C_{20} represent the material constants which are empirically determined.

2.3 Inverse Finite Element Method

Direct and inverse methods exist for obtaining material models. The direct method determines the sample's constitutive model by means of a physical experimental test. An FE analysis that replicates the experimental test, is then created by directly using the results obtained from the experimental relationship into the material model of the FE model. The inverse FE method is a procedure commonly used to obtain material models for not only rubber-like materials, but also biological tissue (Perotti *et al.*, 2017; Abbasi *et al.*, 2016; Garbowski *et al.*, 2012; Buljak *et al.*, 2017). During this procedure the experimental test is duplicated within an FE analysis environment. The design variables, for example the material properties, are optimised within the FE model by reducing the error between the results obtained from the experimental test and the FE analysis. Typically the displacement results from both data sets are used to calculate a root-mean-square (RMS) error in order to determine the difference between the results (Jekel *et al.*, 2016). It is assumed that if the problem is optimised by matching the displacements between the two sets of results, any other data measured from the nodal points will be matched as well. During the optimisation procedure, this RMS error is used as the objective function to be minimised. Eq. 2.6 is a general representation of calculating the RMS error using the displacement data:

$$RMS = \frac{1}{M}\sum_{m=1}^{M}\left(\sqrt{\frac{1}{n}\sum_{j=1}^{n}\left(d_{FEM_j} - d_{EXP_j}\right)^2}\right) \tag{2.6}$$

where the number of nodes are represented by $j = 1, n$ and the number of iterations of the non-linear FE solution, represented as $m = 1, M$ within the FE analysis. Inverse FE analysis proves to be the most robust method in characterising material properties (Jekel *et al.*, 2016; Viljoen, 2018) and will therefore be implemented within this thesis.

Digital Image Correlation (DIC) is one of the widely used methods to capture the deformation of a sample during an experimental test by capturing images during the deformation process (LaVision, 2014). The test sample is covered with a random configuration of speckled paint. Splitting each image into subsets of $N \times N$ pixels and adding this speckled pattern, create a unique contrast pattern within each individual image. The full field displacement is obtained by applying a least squares method alongside an iterative optimisation procedure to fit linear

transformations to each of the contrast patterns in the subsequent images. A subset deformation is thus created when the subset changes shape and location.

The data point locations within DIC data are therefore not easily repeatable, especially within a FE analysis. The nodal data for the two sets of results are therefore not aligned and the nodal results for the FE model need interpolation to fit to the experimental results. Once the nodal data for both sets of results are aligned after interpolation, Eq. 2.6 can be used in order to determine the RMS error. $d_{FEM\,j}$ and $d_{EXP\,j}$ are the displacements at the specified nodes for the FE model and the experimental test respectively.

Within this thesis the DIC data was represented by a second FE model. This allows for better control over the indentation tests. Since the aim is to determine the best indenter shape and orientation, a second FE model allows for quicker analysis and flexibility in the indentation test design, compared to rebuilding a physical experimental setup each time. It is also not yet known if the indentation methods will work, therefore the complete theoretical and simulation based setup will give an indication if the methods work within an ideal case first. This second FE model will still be modelled to represent the complexity of the DIC data. A finer mesh will be used within the second FE model to represent the mismatch of the data points and nodal points between the two sets of results, as well as the larger number of data points found in the DIC data. This will allow for an easier switch from the FE model to actual DIC data in future work.

2.4 MSC Marc Mentat

This section focusses on the Newton-Rahpson method used by Marc to solve for the implicit non-linear FE models. A feature called remeshing, was also introduced within the FE models and some background on this feature will also be explained.

2.4.1 Newton-Rahpson method

Equation 2.7 is the non-linear FE analysis equation used to solve the system of static equations, where K represents the stiffness matrix, u the incremental nodal displacement vector, f the external nodal-load vector and r the internal nodal-load vector (MSC Software, 2017*a*).

$$K(u)\,\delta u = f - r(u) \tag{2.7}$$

K and r are functions of u, but it should be noted that f can also be a function of u in many cases. Considering δu^i is the most recent approximated solution for iteration i in the current increment n, then Eq. 2.7 can be rewritten in iterative form as:

$$K\left(u_{n+1}^{i-1}\right)\delta u = f - r\left(u_{n+1}^{i-1}\right) \tag{2.8}$$

Using Eq. 2.8 to solve for δu^i, the next appropriate solution is determined by:

$$\begin{aligned} \Delta u &= \Delta u^{i-1} + \delta u^i \\ u^i_{n+1} &= u_n + \Delta u^i \end{aligned} \tag{2.9}$$

The solution to these equations represents one iteration, which is repeated until convergence is reached. Figure 2.1 graphically illustrates how the Newton-Raphson method iteratively finds the roots for the one-dimensional function $F(u) - 1 = \sqrt{u} - 1 = 0$. Starting at increment 1 and ending at increment 2, results in the solutions $F(u_0) = 0.2$ and $F(u_{last}) = 1.0$ respectively. Three different convergence criterion exist within Marc:

1. Residual checking
2. Displacement checking
3. Strain energy checking

Residual checking minimises the out-of-equilibrium force by normalising the maximum residual load $F_{residual}$ with the maximum reaction load $F_{reaction}$ to a user defined tolerance Tol_1 and can be expressed by Eq. 2.10 as:

$$\frac{\|F_{residual}\|_\infty}{\|F_{reaction}\|_\infty} < Tol_1 \tag{2.10}$$

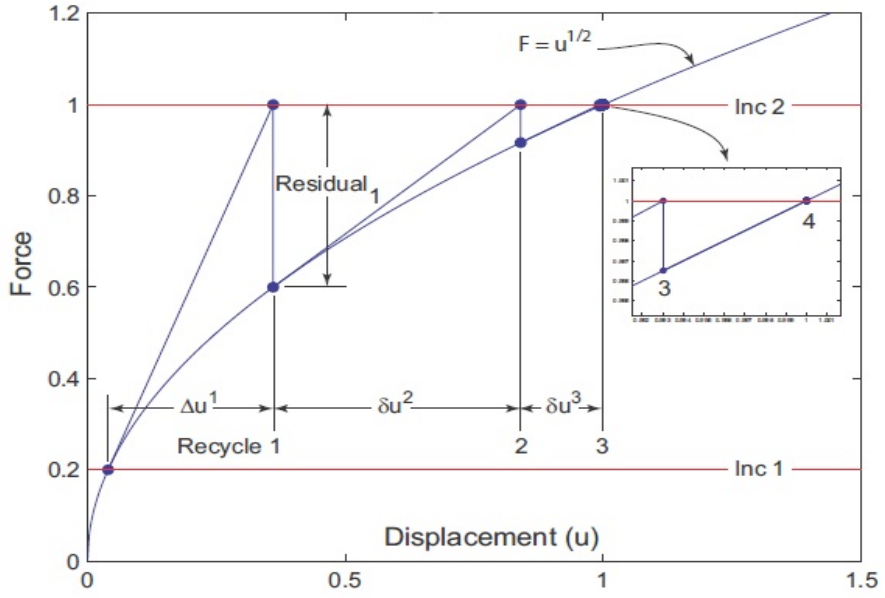

Figure 2.1: Newton-Rahpson method for a non-linear FE analysis (MSC Software, 2017*a*)

with F being the component of the force vector with the highest absolute value. The reaction forces depend on kinematic boundary conditions and contact constraints. If kinematic boundary conditions are applied to the node, then the maximum reaction force can be related to the corresponding component in the force vector. If a contact constraint is applied to the node, the contact algorithm controls the convergence testing. Two contact algorithms exist in Marc and during both algorithms the maximum reaction force can be related to the contact force, but with the following differences during the residual calculation procedure:

1. Node-to-segment: The node in contact is neglected during the residual calculation procedure.

2. Segment-to-segment: The maximum residual force can be related to the unbalanced force components.

Displacement checking minimises the ratio between the maximum nodal displacement of the latest iteration δu and the actual nodal displacement change of the increment Δu to a user defined tolerance Tol_1 as shown in Eq. 2.11:

$$\frac{\|\delta u\|_\infty}{\|\Delta u\|_\infty} < Tol_1 \tag{2.11}$$

with δu representing the correction to incremental displacement vector, Δu the displacement increment vector.

Strain energy checking uses the same procedure as displacement checking where the global strain energy of the latest iteration is compared against the global strain energy of the increment to minimise the ratio to a user defined tolerance Tol_1:

$$\frac{\delta E}{\Delta E} < Tol_1 \tag{2.12}$$

with ΔE representing the global strain energy of the increment and δE representing the correction to incremental global strain energy of the iteration.

It can be noted that both residual and displacement checking are local convergence criteria where as strain energy checking is the only global criteria checking scheme. In Marc two combination checking criteria are available:

1. Residual or displacement checking: Here both checking criteria are used for convergence, but final convergence is reached when only one criterion is satisfied.

2. Residual and displacement checking: Again both criteria are used for convergence, but both criteria need to be satisfied for final convergence to occur.

There is not an option available for using strain energy checking in conjunction with residual and/or displacement checking, but having an option for residual with displacement checking, is considered more than sufficient. During this thesis all FE analyses were performed using the combination between residual and displacement checking according to Eq. 2.13, using the full Newton-Rahpson method.

$$\begin{aligned} \frac{\|F_{residual}\|_\infty}{\|F_{reaction}\|_\infty} &< Tol = 0.01 \\ \frac{\|\delta u\|_\infty}{\|\Delta u\|_\infty} &< Tol = 0.01 \end{aligned} \tag{2.13}$$

2.4.2 Automatic Global Remeshing

A complication associated with non-linear FE analysis of hyper-elastic models is the frequent encounter with distorted elements, mainly caused by the large deformations. A quick solution is to reduce the mesh size in order to create a finer mesh. The finer mesh contains more elements, therefore more nodes, to improve the quality of defining and representing the complexity of the deformed shape. The drawback of resolving to a finer mesh is the exponential increase in computation time, which is not desirable. Marc has introduced a solution to this complication. The computation time will still increase, but not with an exponential factor. Global Remeshing is a method where the FE analysis replaces the distorted mesh with a better quality mesh. An example, when the deformation complexity increases or the strain gradient becomes too large for the element size, distortion is encountered. When elements lack the ability to define the complex deformed shape, a new mesh with a smaller element size is created to have the ability to define the complex shape. Another example is when the elements turn inside out during the analysis, the old mesh is replaced with a new mesh but not necessarily a finer mesh. Global Remeshing cuts down the computation time by only changing the mesh in a user defined region where the most distortion is expected. The computation time therefore only increases due to the extra calculations within the new region instead of the whole sample (MSC Software, 2017*a*).

Remeshing can only be defined within the Marc FE analysis through a contact body, due to the position and location change of nodes between remeshing instances. A contact body ensures that node associated boundary and initial conditions get transferred correctly between meshes (MSC Software, 2017*a*). Since more than one type of distortion triggers remeshing, different types of remeshing exist to solve for each type of distortion trigger. The manner of how the remeshing should occur to solve for the specified distortion, gets specified through a contact body as well. Unfortunately this means a dummy body needs to be created for the remeshing part, if contact is not needed in the analysis. It is required to specify the type of mesher, when remeshing needs to occur and the mesh size

controls and other settings need to be defined in order to perform global remeshing. The basic steps how remeshing does occur are (MSC Software, 2017*a*):

1. The specified remeshed body's surface or outline is extracted from its current, deformed shape.
2. A new mesh is created according to this outline after it has been cleaned from any unwanted distorted instances.
3. Data from the old, deformed mesh is transferred to the new mesh through data mapping.
4. The new mesh possesses a new outline and new tolerances with refined contact parameters.
5. If there are boundary conditions present, they will also be transferred to the new mesh.
6. Marc will continue with the analysis, using the new mesh.

Global remeshing offers a work around to improve the distorted complications associated with non-linear FE analysis, but it does possess limitations and drawbacks and complications (MSC Software, 2017*a*):

1. Supported analysis includes mechanical analysis, thermal-mechanical, electrostatic-structural coupled and thermal Joule mechanical.
2. For 3D cases only lower order hexahedral, lower and higher tetrahedral element types are supported.
3. Remeshing only occurs for a meshed contact body, therefore boundary conditions and other contact information need to be defined through contact definitions for re-calculation based on the new mesh. An advantage is that Rigid-Deformable contact and Deformable-Deformable contact are supported features.
4. Boundary definitions are supported on a remeshed body and get transferred to the new mesh after remeshing, but a new table style input format, called a contact table, is required.
5. Global remeshing and local adaptivity cannot be used together.
6. Using full mesh density control, the mesh density can be based upon the results.
7. If domain decomposition is required, the remesh body needs to be included in a single domain.
8. Pre-state initial conditions and model sections are supported.

9. Cyclic symmetry is supported

10. Flow lines and particle tracking (node tracking) are only supported for certain element types.

Two main limitations stand in the context of the present study. These are the boundary conditions that need to be specified through a contact body and the limited use of node tracking with only certain elements. Both of these limitations were taken into consideration during the FE modelling stage of the thesis.

2.5 Numerical Optimisation

The inverse FE method is built on the concept of using an optimisation algorithm to find the best solution to a mathematically designed problem, where Eq. 2.14 serves as a general constraint optimisation problem typically used in engineering practices. The optimisation algorithm iteratively solves for the mathematical problem until the best combination of values for the unknown design variables, x_i, $i = 1,...,N$, is found. This mathematical equation serves as the optimisation algorithm's objective function and the aim of the algorithm is to minimise the objective function, represented by $f(x)$, which is dependent on the design variables. The feasibility of the optimisation problem can be controlled by a number of inequality constraints, g_j, $j = 1,...,M$, or equality constraints, h_k, $k = 1,...,L$, or a combination of both. The side constraints, x_i^L and x_i^U, serve as the lower and upper bounds respectively for each of the design variables to define the design space for these variables (Vanderplaats Research & Development Inc., 2001).

$$\begin{aligned} \text{Minimise:} \quad & f(x), \quad x = [x_1, x_2, ..., x_N]^T \\ \text{Subject to:} \quad & g_j(x) \leq 0, \quad j = 1, M \\ & h_k(x) = 0, \quad k = 1, L \\ & x_i^L \leq x_i \leq x_i^U, \quad i = 1, N \end{aligned} \tag{2.14}$$

Optimisation algorithms can mainly be categorised as gradient based- or non-gradient based. Gradient based algorithms find the optimum design point by starting at a single design point within the design space. A search direction is typically obtained by using gradient information at this point. Many gradient based optimisations make an improvement from the previous design point by using a line search technique based on the search direction. As soon as the best objective function is obtained along the current search direction, the process repeats and a new search direction is obtained through a new set of finite difference steps from the current position. The process comes to a stop when convergence is reached according to a predefined criterion (Venter, 2010; Jan A. Snyman, 2005). Non-gradient based algorithms do not use gradient information for finding the optimum design point. Unlike gradient based algorithms, non-gradient based algorithms do not only use a single starting point, but rather utilise a set of points.

The next iteration's set of points is obtained by evaluating the quality of each point in the current iteration with a user defined fitness function. Meta-heuristic techniques are then used for the selection process to the new iteration's set of points (Chai-ead *et al.*, 2011).

Even though some optimisation algorithms are more robust than other, they are all problem specific and therefore there is no best algorithm for all problems. The best way to determine if gradient based or non-gradient based optimisation will be the best, is to take a closer look at the advantages and disadvantages of each. Venter (2010) suggests that gradient based algorithms are in general better when numerical noise is quite low, when the number of design variables are approximately above 50 and when the computational cost is expensive. These algorithms are also more prone to converging on a local minimum rather than the global minimum. The one starting point controls the direction of the optimisation and converges to the nearest minimum, local or global (Venter, 2010; Vugrin, 2005). Therefore if local minimum is not an issue, these algorithms generally perform better due to their ability in controlling the optimisation through the means of proving constraints. Non-gradient based algorithms work better for a problem with fewer than 50 design variables, for severe numerical noise, for computationally inexpensive problems and when the gradients are not available. These algorithms have a better chance of reaching a global optimum since they consider more than one starting point and are able to eliminate many local optimum values by taking all the points in consideration (Venter, 2010).

Keep in mind that the inverse FE method performs an FE analysis every time the objective function is evaluated, therefore the computational cost associated with the optimisation problem is quite high. In this thesis only FE models will be used, the numerical noise between the two models should theoretically be relatively low since both models will be modelled the same, lowering the discrepancy between the two sets of results (Vugrin, 2005). One FE model will however be modelled such that it represents DIC data by using a finer mesh and more data points. Numerical noise will be added due to the numerical approximations in calculating the objective function. Examples are the interpolation techniques in matching the two data sets and the gradient calculations within the optimisation procedure (Vugrin, 2005).

There will be only three design variables and local minimum values might be present. This thesis is not aimed at finding the best optimisation algorithms and comparing them, but rather to find one which will be able to optimise the problem efficiently. Due to the high computational cost of the problem and since the Mooney-Rivlin material model will be used, which requires valid initial variables to converge, constraint gradient based optimisation will be used in this thesis (Jekel *et al.*, 2016; Jan A. Snyman, 2005).

According to Venter (2010) three widely used constraint gradient based algorithms used for engineering problems are the Modified Method of Feasible Directions (MMFD), Sequential Linear Programming (SLP) and Sequential Quadratic Programming (SQP). All three algorithms were investigated in this thesis, but ul-

timately the SLP algorithm produced the best objective function value in most instances. The SQP algorithm was also used, due to interesting results obtained by the algorithm which will be shown in later chapters.

Vanderplaats Research and Development Inc. is a software company which specialises in providing commercially available optimisation software, mostly used in the automotive and aerospace industries. Over their range of different software packages, the main similarity is the Design Optimization Tools (DOT) library (Vanderplaats Research & Development Inc., 2001). DOT is a gradient based optimisation package developed for engineering optimisation problems. This library has been obtained as a simple wrapper to be used within Python as an efficient optimiser. A Python script is able to serve as the integration software to link the input and output files from Marc with DOT. The material model variables are used as the design variables given to DOT for optimisation. The aim of the optimisation problem is to minimise the RMS error between the two FE models displacements. Since DOT was designed for engineering applications, the algorithm aims to stay within the feasible region during the one dimensional search as much as possible and to reach a near optimum answer as quickly as possible. More on the optimisation pipeline will be discussed in Chapter 4.

Chapter 3

Finite Element Criteria, Techniques and Models

During this thesis FE analysis was used to perform different indentation tests. This resulted in a series of different techniques that were necessary for successful implementation and generation of results. This chapter presents the different techniques and criteria used to obtain the FE models.

3.1 Design Concepts for the Finite Element Models

A key difference in this project compared to other inverse FE characterisation optimisation projects found in literature, was that this thesis did not include any physical experimental setup and real time data. This project was completely simulation based and two FE models were created for each indentation test. One FE model, referred to as the "Experimental" model, contained the desired Mooney-Rivlin parameters obtained from Viljoen (2018), and consisted of a finer mesh. It is expected that future work will implement the methodology developed and proposed here with experimental work where displacement data is obtained using DIC. The finer mesh within the "Experimental" model serves as a representation of the large quantity of data points obtained from DIC. In future work the approach and numerical pipeline developed here, can directly be used by replacing the "Experimental" model with DIC data.

The second FE model, referred to as the "Numerical" model, consisted of a coarser mesh than that of the "Experimental" model and the Mooney-Rivlin parameters were the design variables during the optimisation process, which will be described in Chapter 4. These design variables are considered unknown, as with a characterisation process using experimental data. Through the optimisation process the design variables will be determined and compared to the desired parameters from the "Experimental" model in order to validate the credibility of the indentation test used. Throughout the whole optimisation procedure, the displacement field obtained from the "Numerical" model will be extrapolated to

match the displacement field of the "Experimental" model. In future work, this process will ensure that the optimisation procedure will optimise for the actual experimental results.

The indentation tests can be divided into two categories:

1. Cylindrical indenters
   Four indentation tests were performed using cylindrical indenters. Each test used a different orientation or number of indenters.

2. Spherical indenters
   Only two indentation tests were performed using spherical indenters. The difference between the two tests was the number of spherical indenters used.

In total, six different indentation tests were optimised during this thesis, with each test having an "Experimental" and "Numerical" model for optimisation. Figures 3.1a-3.1f are the preliminary design layouts for each indentation test. The front surface of the red squared sample, is the surface for data capturing. The surface is located within the XY-plane at $Z = 0$. The XY-plane serves as the parallel plane and the ZY-plane serves as the perpendicular plane, to the frontal surface used for data capturing. The different indentation tests are referred to the orientation of the indenter within the respective plane it is applied in, compared to the surface used for data capturing.

Within Figure 3.1 the yellow squares are the base on which the silicone samples are fixed. The blue cylinders or spheres are the indenter/s in each indentation test. All the cylindrical indenters have a radius of 3 mm and a length of 30 mm, except the cylindrical indenter in Figure 3.1d which possesses a length of 35 mm. The spherical indenters all have a radius of 3 mm. The red squares are the silicone-rubber samples, each having a size of 20 mm × 20 mm. The thickness of all the samples within each indentation test is 5 mm.

3.2 Element Types and Principles

This section describes the type of principles behind the element type used during the FE modelling. This will provide the necessary information to be considered for the choice of certain features and methods used in the FE models.

Marc provides an adaptive method to accurately formulate models with incompressible or nearly incompressible capabilities in the plane strain, axisymmetric and three-dimensional cases. The Herrmann formulation uses either the total Lagrangean or updated Lagrangean procedures to formulate large deformation analysis. The Lagrangean multipliers impose the incompressibility constraint. Lower order elements contain this multiplier on an extra 4th center node, while the higher order elements have a multiplier at each corner node (MSC Software, 2017*a*). Two types of elements are available for incompressible or nearly in-

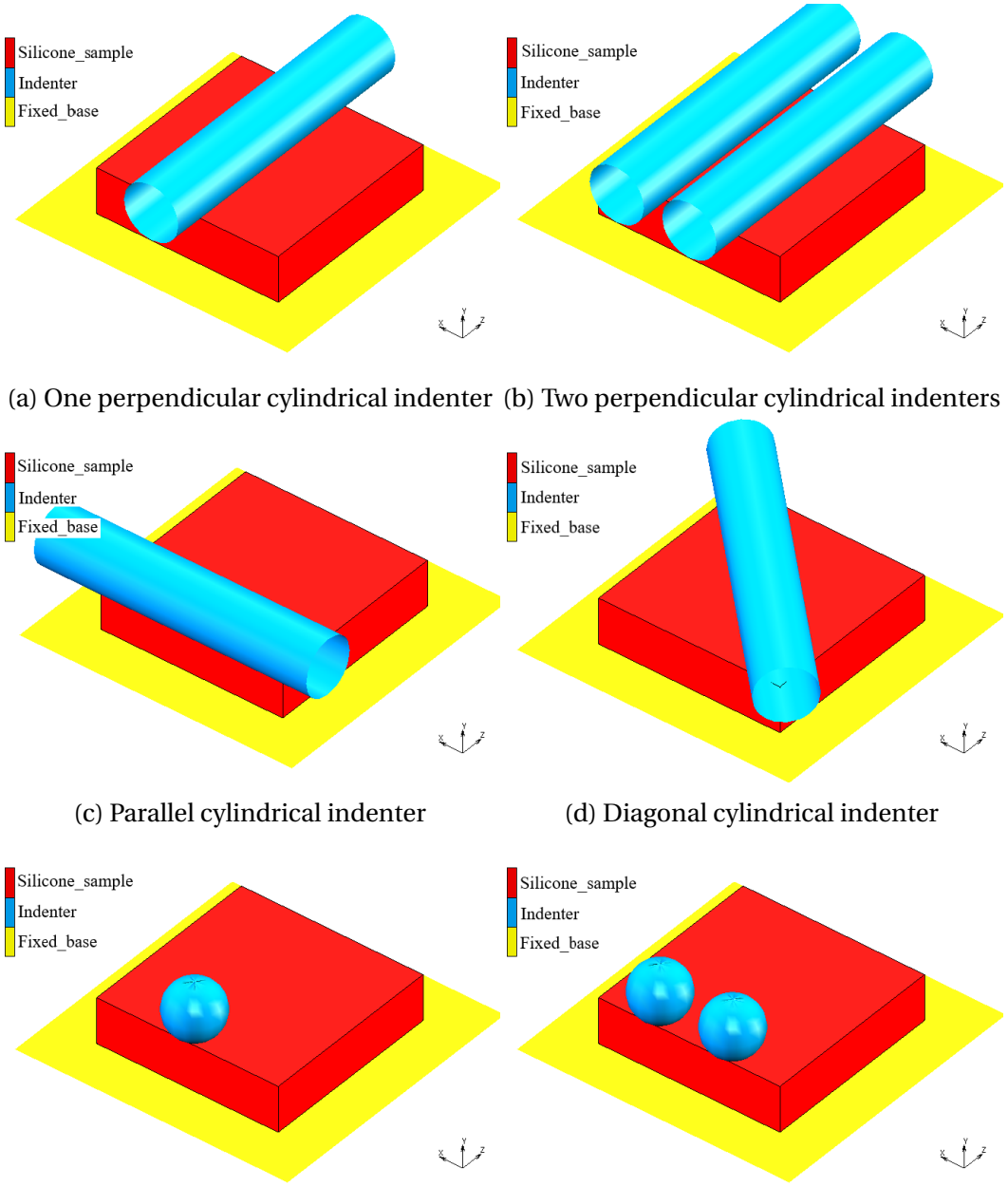

(a) One perpendicular cylindrical indenter (b) Two perpendicular cylindrical indenters

(c) Parallel cylindrical indenter (d) Diagonal cylindrical indenter

(e) One spherical indenter (f) Two spherical indenters

Figure 3.1: Design concepts for six indentation tests for the FE models

compressible rubber-like materials with Herrmann formulation capabilities (MSC Software, 2017*b*):

1. Second-order isoparametric tetrahedron (tet10 element)
   The coordinates and displacements are obtained through biquadratic interpolation functions, which favour higher accuracy strain field representations. It is the recommended element type to use for large strain behaviour.

2. Three-dimensional, isoparametric, 4 + 1-node, low-order tetrahedron (tet4 element)
   Along the element boundaries the displacements and coordinates are linearly distributed. This element tends to cause slow convergence during mesh refinement, which might also result in displacement distortion for large strain applications, depending on the level of deformation within the meshed body.

MSC Software (2017*b*) suggests that the updated Lagrange method is best suited for analysis involving incompressible rubber-like materials in the large strain cases. The numerical difficulties, due to volumetric constraints, are overcome in this method. This is done by using a mixed formulation where the displacements and hydrostatic pressure are independent variables. This thesis used the tet10 elements with the updated Lagrangean formulation for the higher accuracy results within the strain field.

3.3 Remeshing Settings

3.3.1 Criteria for when remeshing should occur

The remeshing criteria determine when and where remeshing will occur. Several user defined criteria exist, along with the automatic criteria. Automatic remeshing only occurs at the start of each increment and the increment is repeated until a solution is found. For automatic remeshing to be performed, one of the following two cases needs to occur (MSC Software, 2017*a*):

1. During the solution, the elements turn inside out.

2. Either crack initiation or growth is present in the solution.

Some of the more important user defined criteria are (MSC Software, 2017*a*):

- Increment - At this specified increment frequency, the model will remesh. During this thesis the default frequency was set to either 4 or 5 depending on the complexity of the model.

- Contact penetration - Penetration cannot be accurately detected if the contact body's curvature is distorted. When the penetration exceeds twice the contact tolerance and goes below the target element size, remeshing will occur. Unfortunately self-contact does not form part of this check. Here the penetration tolerance is set to 0.003.
- Immediate - Before any analysis occurs the contact body is remeshed. This feature is activated to ensure that the identified area where the indenter makes contact, has a finer mesh.
- Strain change - The strain change for each element is recorded after remeshing and the model is remeshed again if any element in the body experiences a strain change greater than the control limit. During this thesis a constant maximum limit of 0.3 was used.

3.3.2 Meshing Techniques

Marc only offers two types of techniques for 3D-solid meshing (MSC Software, 2017*a*).

- Overlay hexahedral mesher - This technique does not support any boundary condition constraints and does not allow for full access to mesh density control.
- Adaptive hybrid mesher - This technique is perfect for tetrahedral meshing and allows full access to all mesh density control settings and supports boundary condition specifications.

During this thesis the adaptive hybrid mesher was used due to its full access to both boundary conditions and mesh density control.

3.3.3 Mesh Density Control

The mesh density control settings allow the user to specify the variation in size and/or number of elements to be used during the new mesh. It also allows the user to specify how fine the mesh needs to be in certain areas. A number of mesh density control settings are available, but this subsection will only address the ones used in this thesis.

The background mesh is based on the current mesh's target mesh density and will be used throughout the meshing process. The current mesh consists of elements all provided with a variation of target edge lengths. The mesh generator tries to adhere to all the specified target edge lengths specified and allows for smooth transition between the regions of different mesh density.

Only three Global Density Controls were used during this thesis (MSC Software, 2017*a*)

- Remesh only designated regions (MSC Software, 2019)
  This control setting allows the user to specify which regions need a finer/coarser mesh due to large deformations. By applying this setting, the rest of the mesh will use the original mesh and only the assigned regions change as specified during remeshing. The size of this remesh region is specified by either a box or cylinder.

- Region
  This control setting allows the user to specify how fine/coarse the mesh needs to be in the specified region. The size of the element depends on an element node, by default the element complies by the region settings for a finer mesh, unless the region specifies coarsening if the element is in multiple regions. The region can move according to the movement of a specified node, a rigid contact body or by defining a velocity.

- Curvature
  The target edge length is controlled by either specifying a surface curvature to be defined by the surface of the contact body or an edge curvature defined by either the sharp edges of the a solid body or the boundaries of a shell.

A combination of all three settings was used in this thesis in the order of importance as specified above. The combination allows for remeshing only in the specified regions with a finer mesh and to give special attention to sharp edges.

3.4 Remeshing Drawbacks and Solutions

Remeshing allows new benefits of improving the complications associated with large strain deformations, but two main drawbacks exist. Firstly, a node tracking method is needed. With every remeshing instance, the new mesh contains either more, or fewer nodes than the previous mesh. This means the nodes firstly occupies a new location, secondly they get renumbered with each new mesh. Secondly, the boundary conditions are applied differently. In Marc, boundary conditions cannot be directly applied to FE models undergoing remeshing. This is due to the renumbering of the nodes with each mesh. Applying these boundary conditions to specific nodes in the first mesh, will cause them to be applied as random during the new mesh. Therefore boundary conditions can only be applied through the means of a contact body. Contact analysis comes with its own set of advantages and disadvantages. A disadvantage is the complex analysis associated with tracking the motion of multiple geometries and their motion due to the interaction with these contact bodies. These two drawbacks are quite important for the analysis and post processing for the FE models. Required work arounds for each problem are presented next.

3.4.1 Node Tracking Solution

A node tracking option is available within Marc, but it only works on lower tetrahedral elements. In order to use the tet10 elements a different method is needed.

In Appendix A remeshing was tested to indentify if it is worth using. The results showed that the remeshing model provided a more stable and quicker convergence for a finer mesh. It can be concluded that the remeshing feature is a beneficial addition towards the FE models. Appendix B compared the performance between the tet4 and the tet10 elements with the remeshing feature. The results showed that the tet10 elements have a larger computation time, but the distortion is a lot less and the curve fitting algorithm produced more accurate results with the tet10 elements. The goal of the FE models are to obtain accurate displacement fields, therefore the tet10 elements will be used.

A method is needed to track the tet10 elements iteratively instead of just obtaining the results within the last iteration. Shell or membrane elements can be used to track the nodes on the desirable surface for data capturing. This can be done by using a glue contact constraint to glue these elements to the surface. The glueing contact tolerance needs to be large enough to prevent separation between the two surfaces. The thickness of the elements in the shell/membrane tracking layer needs to be thin enough not to add stiffness to the model that will influence the results. The membrane/shell elements will not be remeshed and will therefore be able to serve as the nodes for data capturing. This is specified using a contact body. These elements will be given the same material properties as the sample.

During this thesis it was decided to use membrane elements with a thickness of 0.001 mm to track the nodes for data capturing. These elements tested to have very little influence on the results. The lower-order element type used for the membrane elements, is characterised by MSC Software (2017*b*) as a four-node, isoparametric, arbitrary quadrilateral element. This element type does not possess a bending stiffness and since bilinear interpolation functions are used, the strains can tend to be constant throughout the element. In contact analysis, this element type is preferred.

3.4.2 Contact Bodies and Boundary Conditions

Remeshing analysis needs contact bodies to define the boundary conditions which lead to some other considerations for the meshed bodies during the analysis. In order to apply boundary conditions through contact bodies, the meshed bodies need to be defined as deformable contact bodies and the boundary conditions as geometric contact bodies. Efficient searching algorithms are used by Marc to find the correct contacting procedures among all of these different bodies. To reduce computation time in the contact analysis a contact table can be used to define the contact procedures among these different bodies. The contact table allows for applying specific parameters and conditions at certain contact

regions for better detection. Additionally the table allows for certain default procedures to be overridden in special cases to ensure the correct contact parameters are applied to the different bodies. During this thesis the node-to-segment contact procedure will be used. This procedure specifies that all the nodes in the exterior surface are considered as possible contact nodes. The nodes in contact get specified by the boundary conditions and the remeshing feature.

The order of defining contact bodies, especially deformable bodies, is important for analysis. As a rule of thumb a deformable body with a finer mesh serves as the contact body, with the coarser meshed body being the contacting body. The deformable bodies are automatically selected as a contact or contacting body within Marc according to the defining sequence. If the finer meshed body is defined as a deformable body before the coarser meshed body, then the finer meshed body is the contact body and the coarser meshed body the contacting body.

In the models created within this thesis, the membrane elements glued to the sample for data capturing, called "skin" elements for identifying purposes, possess a finer mesh than the sample elements. It would make sense that the "skin" elements should be defined before the sample elements, but since the sample elements are the main body that undergoes the various boundary conditions, these elements will rather be defined first. This is where using a contact table becomes beneficial. The sample elements will be defined first, thus all the boundary conditions and parameters between the deformable and geometric contact bodies, will be applied to the sample elements as first priority. Another contact condition which is just as important, is the glued contact condition between the "skin" elements and the sample elements (deformable-deformable contact). Here it is advised that the "skin" elements should have been defined first to ensure that contact detection will occur correctly during the remeshing stages. In the contact table the glued contact condition between these two bodies can be defined to be applied from the second body ("skin" elements) to the first body (sample elements) instead of the default order.

During remeshing the contact table is considered a must, due to the renumbering and positional changes of the nodes. The contact table ensures that the correct nodes undergo the desirable contact conditions after the new mesh was generated. The contact table and the automatic remeshing feature ensure all contact conditions are checked by correcting the nodal position after the new mesh was generated.

The sample elements are the elements which will undergo remeshing and the "skin" elements will not be undergoing remeshing for data capturing. This is specified through the contact bodies. In the remeshing feature, the body that needs to undergo remeshing is specified through the specified deformable contact body. This is the reason why the sample elements and the "skin" elements are specified as two different deformable contact bodies instead of one.

All the boundary conditions within the FE models are modelled as three-dimensional NURBS surfaces. These surfaces are defined as geometric contact

surfaces. The indenter's motion is prescribed through a positional condition to move 3 mm in the negative Y-direction. The indenter at its starting position, has its lowest point at the same level as the top surface of the sample. This ensures that the indenter applies a 3 mm deep indentation within the sample.

The models within this thesis consist of only two geometric bodies, the indenter and the fixed base on which the sample rests. The contact between the indenter and the sample is specified as a touching contact, which allows relative sliding with no friction. The node-to-segment procedure is used for contact detection and this means that all the nodes on the exterior surface are considered touching nodes. During the remeshing feature it can be specified which nodes should be considered touching nodes, by specifying a follower contact body. Here the indenter's geometric contact body is specified as the follower body. in every new mesh, the nodes in the sample which are within the contact tolerance from the indenter, are considered touching nodes and the rest of the nodes will only become contact nodes when they possibly come within the contact tolerance.

Between the fixed base and the sample, another glueing contact is specified. This ensures that the sample will be fixed upon the base to restrict any sliding motion. The idea of modelling these FE models is to ensure it can be carried out as a physical experiment. During a physical experiment surgical glue can be used to fasten the sample to the testing rig. This was a minor concern during the initial stages of the project, that a sample of this small size is prone to slide and move under an applied load. Another method of fastening for future work, can be to use sand paper as base material and restrict the sliding motion due to friction.

One method in order to reduce computation time and solve FE analysis quicker is by using symmetry. The FE models in this thesis can be divided into quarter models and therefore two symmetry surfaces will be applied to each model. These surfaces are not specified as geometric contact bodies, but as symmetry contact bodies. These contact bodies already contain the necessary touching contact conditions. The nodes in contact with these bodies are automatically constraint in the perpendicular plane of the applied symmetry surface (MSC Software, 2017*a*).

3.5 Final Designs of the Finite Element Models

All the sections within this chapter explained how the final FE models were modelled within Marc. Figures 3.2a-3.2f showcase the final "Experimental" models modelled within Marc, with all the applied meshes and contact bodies. The "Numerical" models looked exactly the same, but with coarser meshes.

Within the figures 3.2a-3.2f, the green bottom surfaces represent the fixed base the silicone sample is glued to. The pink and salmon-coloured planes are the two symmetry planes for each model. The red squares are the meshed "Experimental" samples at a current element edge length of 1.5 mm. The blue hue

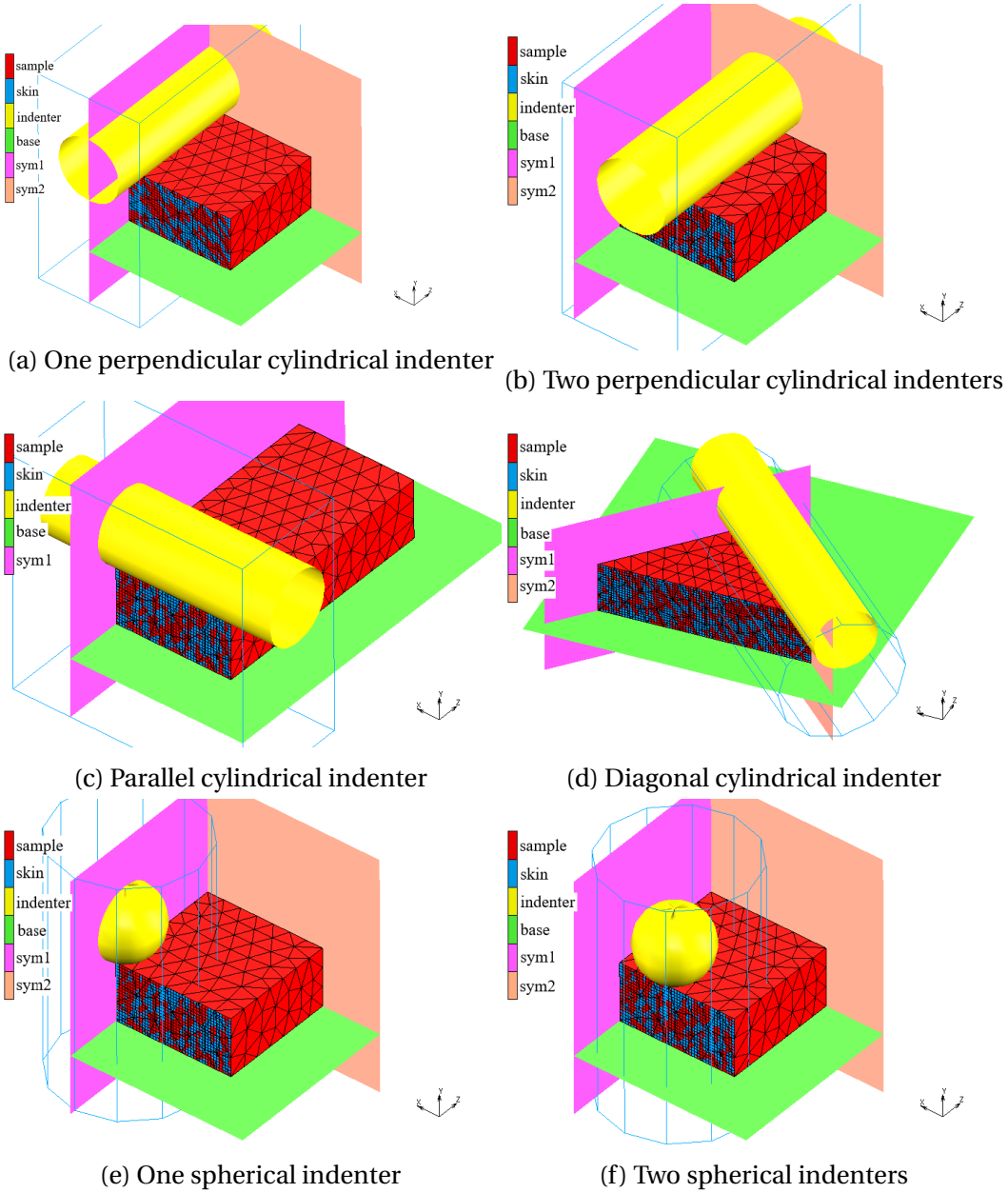

(a) One perpendicular cylindrical indenter

(b) Two perpendicular cylindrical indenters

(c) Parallel cylindrical indenter

(d) Diagonal cylindrical indenter

(e) One spherical indenter

(f) Two spherical indenters

Figure 3.2: Meshed and symmetrical representation of final "Experimental" FE models

on the front surface of the red square, represents the "skin" samples. Around each of the yellow indenters, a blue box or cylinder is outlined. These outlined cylinders or boxes are the regions identified for remeshing.

3.6 Summary

This chapter discussed the various techniques and methodologies used to create the FE models inside Marc. Six different indentation tests were modeled, each with two FE models. Each indentation test was modeled with a 20 mm × 20 mm × 5 mm square sample specified as a deformable geometric body and meshed with tet10 elements. The sample rests on the base surface, specified as a rigid geometric body. A linear position ramp of 3 mm was applied to the sample through the indenter/s in the negative Y - direction over a time period of one second, which represents the indentation depth as a function of time. The cylindrical indenters possess a diameter of 3 mm and a length of 30 mm, except for the diagonal indenter that possesses a length of 35 mm. The spherical indenters possess a diameter of 3 mm. Two contact conditions are applied between these three bodies. A glued contact is specified between the sample and the base to limit the movement of the sample during analysis. A touching contact is specified between the indenter and the sample to simulate the applied indentation load and the deformation of the sample.

The remeshing feature causes the number of nodes to change with each remeshing instance and therefore to be renumbered. This restricts the ability to track the nodes throughout the analysis and obtain the absolute nodal displacement with each analysis. To track the nodes, a layer of four-noded, isoparametric, quadrilateral membrane elements, were glued to the surface of interest for data capturing. This layer is called the "skin" elements, specified as a deformable geometric body. A glued contact condition is specified between the sample and the "skin" elements so that the "skin" elements deform with the sample elements.

The sample within the "Experimental" models were meshed with a minimum element edge length of 1.5 mm and a minimum remeshing element edge length of 0.9 mm. The "skin" layer were meshed with a minimum element edge length of 0.25 mm and a thickness of 0.001 mm to ensure the layer does not add to the stiffness of the sample. The samples within the "Numerical" models were meshed with a minimum edge length of 2 mm and minimum remeshing element edge length of 1 mm. The "skin" layer in this model had a minimum element edge length of 0.5 mm and a thickness of 0.001 mm. Since the node numbering do not stay constant after a remeshing instance, the boundary condition need to be applied through contact bodies. Each FE model had two boundary conditions specified for symmetry conditions, except for the parallel cylindrical indenter with only one symmetry condition. A symmetric contact body was specified for two surfaces, one in the XY - plane to restrict movement in the opposite z - direction, and another in the YZ - plane to restrict movement in the opposite X - direction. Another touching contact condition were applied between the symmetry planes and the sample.

Chapter 4

Numerical Pipeline

The two main parts in this thesis are firstly the indentation tests simulated as FE models and their FE analysis techniques described in Chapter 3. The second part is the numerical pipeline, which will be described in detail within this chapter.

4.1 Numerical Pipeline Process and Work flow

In figure 4.1, a flow chart shows the process of the numerical pipeline and the link between the different software. This section will explain in depth what happens between each step.

The optimisation procedure within this thesis aims to optimise the constitutive material model for the "Numerical" model to obtain results matching that of the "Experimental" model. This was done by using the Mooney-Rivlin three parameter model for both the FE model's material model. The three Mooney-Rivlin coefficients, C_{10}, C_{01} and C_{20}, served as the design variables within the optimisation procedure for the "Numerical" model. During the study conducted by Viljoen (2018), it was concluded that the Mooney-Rivlin material coefficients obtained in table 4.1, predicted the experimental data the best. A combination of uni-axial tensile and compression data was used to obtain these material coefficients through inverse FE analysis.

Table 4.1: Mooney-Rivlin three parameter material model used for the "Experimental" model (Viljoen, 2018).

	C_{10} [MPa]	C_{01} [MPa]	C_{20} [MPa]
"Experimental" model	0.2605676	0.0975498	0.0575007

The pipeline starts with a Latin Hypercube (LHC) model, discussed in section 4.2, to generate a set of 10 design points. This means that each indentation

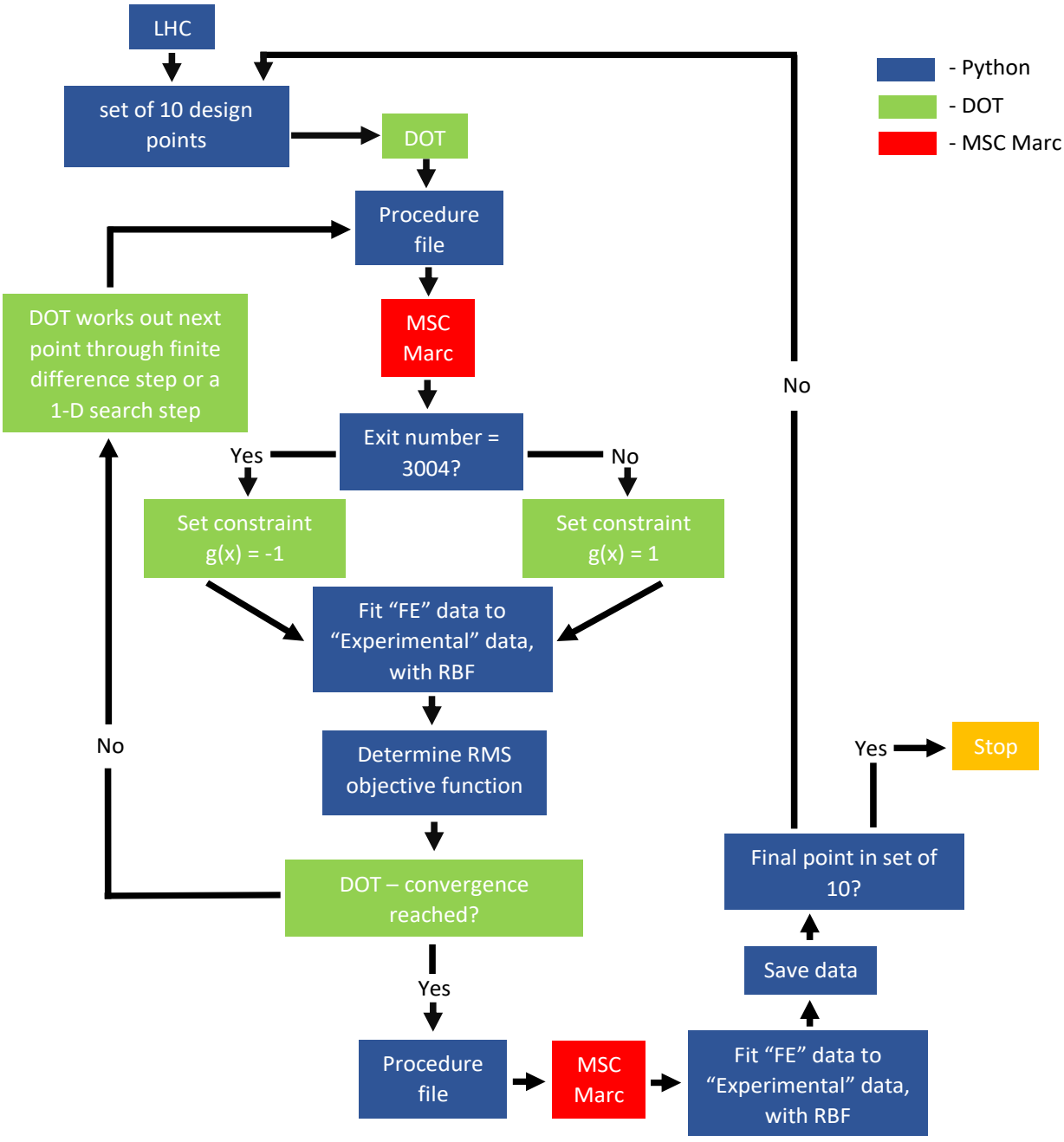

Figure 4.1: Flow diagram of the link between software within the numerical pipeline

test will be optimised 10 times, each time starting with a new design point. A `for` loop is created in Python to start the optimisation process for each design point.

Firstly three files are created:

- A Python file called `results(?).py`. This file stores the starting point's

design variables and after the optimisation, the optimised point along with a list of the objective function during each iteration. `(?)` Is a place holder for the design point number created through the LHC model, zero indexed.

- A file called `starting points.txt`. This file stores the set of design points obtained through the LHC model. This file is only created and accessed during the first loop.
- A file called `violated(?).py`. This file stores all the design points that caused a "Numerical" model not to converge. This will be used to discuss how sensitive the material model is.

DOT is called for the first time and the optimisation procedure within the loop starts, by either using the SLP or SQP constraint algorithm. Each starting point will be optimised with both optimisation algorithms, in total 20 optimisation runs will be done for each indentation test. There is a scaling difference between the three design variables; it was therefore decided to normalise the set of design variables throughout the optimisation procedure. This was done by dividing the design variables with itself during the first iteration to obtain a starting point with each design variable equal to 1. This allows DOT to optimise for each of the parameters to the same scale. Before the Marc procedure file is written, the parameters are denormalised by multiplying with the starting point's design variables.

Next, a Marc procedure file is created. The procedure file allows Python to call Marc and control the simulations. Marc is called with this procedure file, the Python script pauses momentarily while the following steps occur within Marc in the background:

1. The correct "Numerical" model is opened within Marc.
2. Each material constant within the material model is changed to the current iteration's corresponding design variable.
3. The FE analysis is started.
4. The post-file is accessed from Marc to save the file for Python to process.
5. The indenter's height, h_m, is saved for each increment in the "Numerical" model's FE analysis.
6. Marc is closed.

After Marc closes in the background, the Python script continues. A fail-safe was added within the code to ensure all the Marc output files are saved, by pausing the script for an additional five seconds. The status file from Marc is checked to ensure the "Numerical" model converged. This is done by checking if the exit

number equalled 3004. This exit number is used as the constraint for the optimisation procedure.

The objective function is obtained by calculating a single RMS value between the "Numerical"- and "Experimental" model's displacements. Linear interpolation and a radial basis function (RBF) are used to interpolate the nodal results for the "Numerical" model to the same positions of the "Experimental" model's nodal results, which is necessary for the comparison between the two models.

DOT evaluates the objective function and constraint values to determine if convergence was reached or if the constraint was violated. The objective function is saved within a list to visualise the convergence path after the optimisation converged. If convergence was not yet reached, DOT determines the next set of design points and the process restarts with the Marc procedure file.

If the optimisation process converged, the following process is followed:

- The list containing the objective functions for each iteration and the final design variables is saved within the `results.py` file.
- Another Marc procedure file is created with the optimised design variables and Marc is restarted. DOT backtracks to a previous iteration when the constraint is violated, thus it does not mean the latest Marc output files were for the optimised design variables. By restarting the "Numerical" model again, with the final design points after optimisation convergence was reached, ensures the data from the Marc output files are indeed the final design variables results.
- The results for the "Numerical" model are interpolated to the positions of the "Experimental" model's and the interpolated results are saved for the optimisation set.

At this point the first set of design variables is optimised and the optimisation restarts for the next set of variables.

4.2 Latin Hypercube Model

A Latin Hypercube (LHC) design of experiments is a statistical method to find a set of design points in a multidimensional design space. This method has been generally used to find a set of design points for computer aided optimisation algorithms. The LHC model is based on having a square, called a Latin square, that represents the design space. The idea of this model is to find points in this square so that each row and each column only occupy one point. The distribution between these points is based on the user's criteria and can be described as the user sees fit to find its own set of design points optimally spaced within the design space (Viana *et al.*, 2010; Viana, 2013). This method is becoming increasingly popular due to that there is no constraint or limitations involved with the data density or location as well as the size of the design space and the method

is model independent. One advantage of the LHC design is that the samples are non-collapsing, meaning that if one dimension is removed from the design space, the existing points can be reused without needing to use fewer sample points or re-evaluate the points in the smaller design space (Viana, 2013). This proves that the orthogonality of the design points is well spread out over the design space and a repeat of variables is almost non-existent. Due to the well-spread out space filling technique of the LHC model, this sampling method will be used within this thesis.

A set of 10 design points was obtained using the LHC sampling method, for the optimisation of each indentation test. A Python library is available, called Design of Experiments for Python (pyDOE), which contains a LHC function. The function is represented in Eq. 4.1 (Lee, 2013-2014).

$$\text{sample points} = lhs\left(n, [\text{samples}, \text{criterion}, \text{iterations}]\right) \tag{4.1}$$

where n is the number of design variables within a set, 'samples' is the number of design points to generate. The 'criterion' option specifies how the samples should be distributed within the design space and this function allows for four different spacing techniques. Firstly is the `center` criterion, which centres the points within the design space. The second method, `maximin`; the points are randomised within the design space but the minimum distance between each point is maximised. `Centermaximin` is a combination of the `center` and `maximin`, where the points are centred within the design space, but the minimum distance is maximised between the points. `Correlation` minimises the maximum correlation coefficient. All the points are then generated according to the criterion between 0 and 1. This allows the user to then scale the output to their specified set of variable's design space (Lee, 2013-2014).

During this thesis, $n = 3$ for the number of design variables, which are the Mooney-Rivlin coefficients, 'samples' = 10 for the set of 10 starting design points for each optimisation run and 'criterion' = `maximin`. The output was then scaled for each variable between its own given range shown in table 4.2.

Table 4.2: Lower - and upper bounds for each of the material model parameters

	C_{10} [MPa]	C_{01} [MPa]	C_{20} [MPa]
Lower bound	0.2084541	0.0780398	0.0460006
Upper bound	0.3126811	0.1170598	0.0690008

The lower and upper bound for each Mooney-Rivlin parameter were obtained by adding and deducting 20% from the original coefficients in table 4.1 respectively. These bounds were used as the side-constraints within the DOT optimisation algorithms as well.

4.3 Radial Basis Function

RBFs are used to approximate multivariate functions in any given direction by radialising the linear combination of terms in a single univariant function. According to Buhmann (2010), the approximations by these functions are considered to be mesh-free. The multidimensional Euclidean space is data-dependent and no triangulation between the data points is present. This allows for more accurate data interpolation of large scattered data sets due to the radially symmetric functions. The SciPy library within Python provides an interpolation section where one of the interpolation methods is a RBF. During this thesis this function was used to interpolate the data from the "Numerical" model to the same positions as the "Experimental" model's data. Since the FE analysis uses iterative procedures in solving the FE models, each analysis has a different amount of increments and time step for each increment in which the problem was solved. Before the RBF can be used, linear interpolation is required to obtain the incremental results from the "Numerical" model, at the same time increments as the "Experimental" model's results. A description of the data format received from both FE models are described below, to understand the interpolation process better.

4.3.1 Finite Element Model Data Format

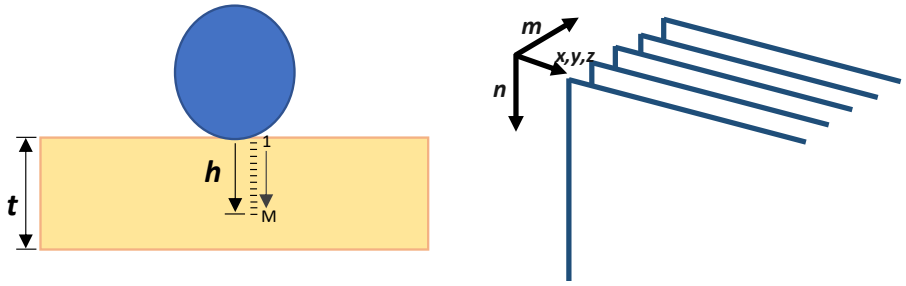

(a) Indenter increment representation (b) FE model data representation

Figure 4.2: Data format from the FE models for the interpolation scheme

During the FE analysis within Marc, the model is solved iteratively therefore the data is represented iteratively. Within this thesis the analysis is specified to solve for an indentation of 3 mm in one second. That one second is divided into M number of increments, with each increment the indenter is at a depth h_m ranging from 0 to 3 mm, as can be seen in figure 4.2a. Therefore the indenter's depth level h_m is directly correlated to the increment number.

For each increment m, the nodes n are specified at a specific location within the X-, Y- and Z-plane, with a specified absolute displacement in the X-, Y- and Z-directions. The data can be presented in a three-dimensional space, shown in figure 4.2b. For each increment or level m, the number of rows is equal to the

number of nodes n and the columns are equal to either the three-dimensional coordinates or displacements.

4.3.2 Interpolation steps

In order to obtain the "Numerical" model's data at the "Experimental" model's data positions, two interpolation steps need to take place. The reason for this is that between the two models, the number of increments, the number of nodes and the locations of the nodes differ, therefore the "Numerical" model's data need to be interpolated for all three cases in two steps:

1. Number of increments
   Generally the "Experimental" model has more increments in which the problem was solved, due to the finer mesh. The "Experimental" model represents DIC data, which would normally also have more increments than the corresponding FE model. It is still plausible that both FE models have the same number of increments, but the depth h_m for the indenter is not necessarily the same for the "Numerical" model as for the "Experimental" model. The first interpolation step is to find the coordinates and displacements for each node in the "Numerical" model at the same indenter depth h_{EXP_m} as the "Experimental" model. This is done by linearly interpolating each node's coordinate and displacement in the "Numerical" model to the corresponding depth h_{EXP_m} of the "Experimental" model's indenter. Numerically it can be represented by Eq. 4.2.

$$\begin{aligned} D_{NUM_m} &= \left(\frac{D_{NUM_{m+1}} - D_{NUM_{m-1}}}{h_{NUM_{m+1}} - h_{NUM_{m-1}}}\right) \times \left(h_{EXP_m} - h_{NUM_{m-1}}\right) + D_{NUM_{m-1}} \\ C_{NUM_m} &= \left(\frac{C_{NUM_{m+1}} - C_{NUM_{m-1}}}{h_{NUM_{m+1}} - h_{NUM_{m-1}}}\right) \times \left(h_{EXP_m} - h_{NUM_{m-1}}\right) + C_{NUM_{m-1}} \end{aligned} \tag{4.2}$$

   where D is the X-, Y- or Z-displacement at increment m, C the X-, Y- or Z-coordinate at increment m and h the indenter level at increment m.

2. Number and location of nodes
   The displacement of the nodes in the "Numerical" model will be predicted at the same location as the nodes in the "Experimental" model using a RBF interpolation. The number of nodes in the "Numerical" model IS increased by predicting it to the same number of nodes in the "Experimental" model and their displacements are predicted with this one interpolation function. The RBF is created by providing the X-, Y- and Z-coordinates with either/or the corresponding X-, Y- and Z-displacement values for the n number of nodes within the "Numerical" model. This function is then used to predict the X-, Y- and Z-displacement values at the given X-, Y- and Z-coordinates of the "Experimental" model. One function is created for each

of the three displacement directions. This process is repeated for each increment. This step is shown in Eq. 4.3.

$$\begin{aligned} RBF_{dx/dy/dz_m} = & Rbf\left[C_{NUM_X}(m), C_{NUM_Y}(m), C_{NUM_Z}(m), \right. \\ & \left. D_{NUM_{X/Y/Z}}(m)\right] \\ d_{NUM_{X/Y/Z}}(m) = & RBF_{dx/dy/dz_m}\left[C_{EXP_X}(m), C_{EXP_Y}(m), \right. \\ & \left. C_{EXP_Z}(m)\right] \end{aligned} \tag{4.3}$$

where $RBF_{dx/dy/dz_m}$ is the RBF function created to work out the interpolated "Numerical" displacements $d_{NUM_{X/Y/Z}}(m)$, at the "Experimental" model's nodal coordinates.

After these two steps the "Numerical" model's data have been interpolated to the same indenter height (increments), as that of the "Experimental" model and within each increment the nodes within the "Numerical" model have been interpolated and predicted to the same number of nodes in the "Experimental" model, at the same locations.

After the whole interpolation process, the only difference between the data sets is the nodes displacement values. It is these displacement values which are used to determine the Root Mean Square (RMS) error.

4.4 Objective Function

Inverse FE analysis uses an optimisation algorithm in order to determine the material properties of a given sample. This is done by minimising an objective function within the algorithm, using the data obtained from the FE models. The RMS error will be used as the objective function in this thesis.

The RMS error determines the error between the "Numerical" model and the "Experimental" model by comparing the nodal displacements. The displacements are functions of the increment m, since the displacement depends on the indenter's depth at the specified increment. The RMS errors for the directions are shown in Eqs. 4.4-4.6 as functions of the increment m, with n representing the total number of nodes.

$$e_X(m) = \sqrt{\frac{\sum_{j=1}^{n}\left(d_{NUM_{Xj}}(m) - d_{EXP_{Xj}}(m)\right)^2}{n}} \tag{4.4}$$

$$e_Y(m) = \sqrt{\frac{\sum_{j=1}^{n}\left(d_{NUM_{Yj}}(m) - d_{EXP_{Yj}}(m)\right)^2}{n}} \tag{4.5}$$

$$e_Z(m) = \sqrt{\frac{\sum_{j=1}^{n}\left(d_{NUM_{Zj}}(m) - d_{EXP_{Zj}}(m)\right)^2}{n}} \tag{4.6}$$

In total, about M number of RMS errors are calculated for each direction. A single RMS error can be calculated by summing all of these RMS errors together to obtain one value, but this causes a bias in the objective function. Since the sample is indented by 3 mm in the Y-direction, there could be a significant difference within the different direction displacement values, depending on the type of indenter. The nodes will also experience a higher displacement in the last few increments, compared to the first few increments, which causes the bias to get even larger. The bias can be minimised by normalising each direction's RMS error at each increment m, with the absolute maximum displacement value of the "Experimental" model at that increment m. This summation is represented by the Eq. 4.7. This single e value describes the entire fit between the known nonlinear Mooney-Rivlin material model from the "Experimental" model and the attempted material model from the "Numerical" model.

$$e = \frac{1}{M}\sum_{m=1}^{M}\frac{e_X(m)}{max\left(|d_{EXP_X}(m)|\right)} + \frac{e_Y(m)}{max\left(|d_{EXP_Y}(m)|\right)} + \frac{e_Z(m)}{max\left(|d_{EXP_Z}(m)|\right)} \tag{4.7}$$

The objective function for the optimisation procedure is expressed by minimising this overall e value for the particular material model in the "Numerical" model's results. One constraint is used to achieve this, the "Numerical" model needs to be successful, i.e. the Marc exit number must equal 3004. The objective function is presented by Eq. 4.8.

$$\begin{aligned} &\text{minimise}: \quad e \\ &\text{such that}: \quad \text{Marc Exit Number} = 3004 \end{aligned} \tag{4.8}$$

Within the optimisation procedure the constraint is controlled through a true-false boolean. If the Marc exit number equalled 3004, the constraint was adhered to and the algorithm was fed -1; if the constraint was violated the algorithm was fed 1. Normally this method would cause problems in a gradient based algorithm, but for DOT this method is not a problem, provided that the optimiser is started from a feasible point. As shown in figure 4.3, if the constraint was violated, represented by the red dots, DOT backtracks within the one dimensional search, shown by the darker arrows. The algorithm is backtracking until it finds a new feasible point, it will then stop there, shown by the yellow dots, before continuing with the next iteration as normal.

For any optimisation procedure a stopping criterion is needed for the algorithm to determine if a feasible solution was obtained. Four stopping criteria are checked simultaneously within DOT and the optimisation process is terminated as soon as one of these criteria is met (Vanderplaats Research Development, 2001):

1. Maximum iterations: If no solution is found within the defined maximum allowed number of iterations, the process will be stopped. The default value is specified to be 100 iterations.

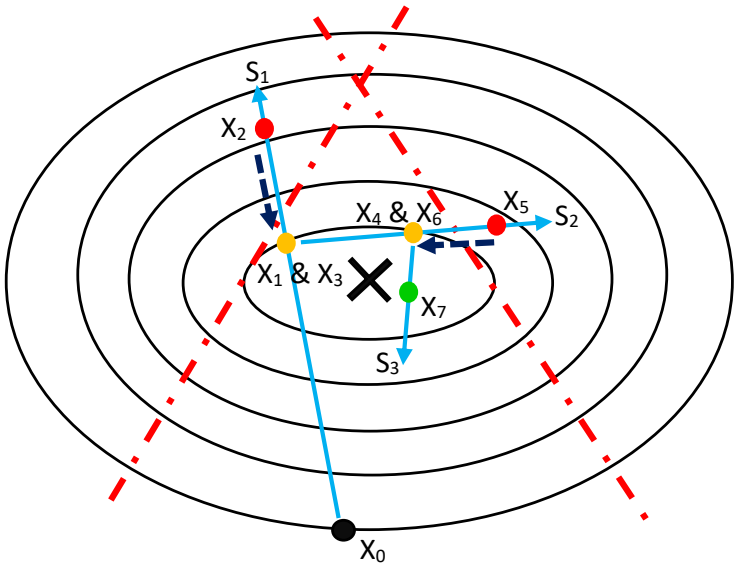

Figure 4.3: Boolean constraint non-convergence backtracking visualisation within DOT

2. No feasible solution: In the case of an infeasible starting point, a feasible solution needs to be found within a user defined number of iterations otherwise the process will be stopped. DOT uses a default value of 20 iterations.

3. Point of diminishing returns: Here one of two criteria will cause the process to stop. Firstly, the relative change in the objective value between iterations is smaller than the user specified tolerance, for a user specified number of consecutive iterations. Secondly, the absolute change in the objective value is less than a user specified tolerance, for a user specified number of consecutive iterations. The default number of consecutive iterations for both criteria is 2. The default relative tolerance is specified as 0.001 and the default absolute change tolerance is 0.0001.

4. Satisfaction of Kuhn-Tucker Conditions: In short, the Kuhn-Tucker conditions require that the sum of the gradient of the objective and the scalars, multiplied with the active constraints associated gradients, must vectorially add up to zero. Optimality is satisfied when these conditions are satisfied and the process will terminate.

The second criterion, point of diminishing returns, is the most general reason for convergence within the optimisation algorithm.

Chapter 5

Validation of Finite Element Models

Uni-axial tensile testing is one of the most common methods for obtaining the material model of a hyper-elastic material. The Mooney-Rivlin material model is a popular material model used during a uni-axial tensile test to predict the behaviour of a material(Wex *et al.*, 2015). This means the Mooney-Rivlin material model has been adapted to use in the uni-axial tensile case and it can be applied to a uni-axial compression case as well. The indentation tests used in this thesis are uni-axial compression loading cases, but the form and size of the indenters cause a multi-axial response. This chapter discusses how the Mooney-Rivlin material model is applied in a uni-axial compression case and how the multi-axial strain response can be investigated. Sensitivity studies were performed on each of the FE model's results for the original Mooney-Rivlin material model from table 4.1.

5.1 Mooney-Rivlin Three Parameter Model

In a uni-axial tensile test, the stress vs. stretch relationship is derived by considering a volume element under a uni-axial tensile stress (σ), shown in figure 5.1. The stretch deformations can be derived as shown in Eq. 5.1 for the case where the stretch is parallel to the uni-axial stress:

$$\begin{aligned} \lambda_1 &= \lambda \\ \lambda_2 &= \lambda_3 = \frac{1}{\sqrt{\lambda}} \end{aligned} \tag{5.1}$$

When substituting Eq. 5.1 in Eq. 2.2, the strain invariants for an incompressible uni-axial tension case become:

$$\begin{aligned} I_1 &= \lambda^2 + 2\lambda^{-1} \\ I_2 &= \lambda^{-2} + 2\lambda \end{aligned} \tag{5.2}$$

For an incompressible material under uni-axial tension, the relationship between engineering stress and stretch can be simplified to (Rivlin, 1948):

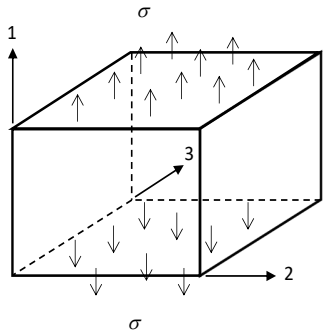

Figure 5.1: Cubic volume element within a Cartesian coordinate system

$$\sigma_e = 2\left(\lambda - \frac{1}{\lambda^2}\right)\left(\frac{\partial W}{\partial I_1} + \frac{1}{\lambda}\frac{\partial W}{\partial I_2}\right) \tag{5.3}$$

Substituting Eq. 2.5 in Eq. 5.3, the engineering stress for the Mooney-Rivlin three parameter material model can be obtained as:

$$\sigma_e(\lambda) = 2C_{10}\left(\lambda - \frac{1}{\lambda^2}\right) + 2C_{01}\left(1 - \frac{1}{\lambda^3}\right) + 4C_{20}\left(\lambda - \frac{1}{\lambda^2}\right)\left(\lambda^2 + \frac{2}{\lambda} - 3\right) \tag{5.4}$$

During a uni-axial tensile test, the material model gets extrapolated to the compression region to determine the feasibility of the material model during another deformation mode. The degree of compression is the same as stretch (λ_y) and can be determined by:

$$\lambda_y = \frac{h}{h_0} \tag{5.5}$$

where h_0 is the initial height of the sample and h is the height at that instant during any point of the compression analysis (Meunier *et al.*, 2008).

During this thesis, indentation tests with cylindrical and spherical indenters, with a radius of 3 mm, are used to obtain the material model of silicone rubber. The shape of the indenter causes the sample to undergo a complex deformation mode, which cannot be described by a pure uni-axial compression/tension case. However, using Eq. 5.5 the theoretical smallest stretch at any point, which can be obtained from a circular shaped indenter, for a maximum indentation of 3 mm, is 0.4 stretch. The approximate maximum stretch obtained by Viljoen (2018) for the Smooth-Sil-950 silicone rubber, was 2.5 stretch. It was therefore decided to use a stretch range of 0.4 to 3.0 to extrapolate the material models in this thesis within a uni-axial test. This is to determine how well the material models obtained through the FE analysis, predict the engineering stress vs. stretch response of the sample. Typically the uni-axial tensile test data extrapolated in the compression region, or vice-versa, increases in error as it moves further away from

the range it was tested in (Holzapfel, 2016). This is due to the fact that uni-axial testing data is insufficient in characterising a material with multi-axial loading conditions (Sasso *et al.*, 2008).

The results obtained from the indentation tests, cannot specifically be classified as one of the classical material characterisation methods (uni-axial tension or compression, bi-axial tension), but a combination of both. Stretch can be described as the deformation (tension or compression) within the principal directions (McGinty, 2012). It is therefore directly associated with the principal engineering strains as:

$$\lambda_i = 1 + \epsilon_i \quad i = 1,2,3 \tag{5.6}$$

where ϵ_i is the i^{th} principal strain within the Cartesian coordinate system of figure 5.1.

The principal strains can be measured within the FE analysis and be classified as either the minimum, intermediate or maximum principal strain. Only the minimum and maximum principal strains were captured for each nodal point within the FE analysis during the indentation tests. The aim in obtaining this data was to determine an approximate strain and stretch range for which the indentation test characterised the silicone sample. This will be represented by determining which node experienced the smallest minimum principal strain and which node experienced the highest maximum principal strain within the final increment of FE analysis. These two nodes are then tracked to represent the relationship between the minimum principal/maximum principal strain and the indentation depth respectively.

5.2 Sensitivity Analysis Between Finite Element Models For Optimisation

Within this thesis two FE models are used in the inverse FE optimisation procedure. The "Experimental" FE model represents DIC data and was therefore decided to be modelled with a finer mesh. The RMS error between the two FE models' nodal displacements is used as the objective function for optimisation. Since the aim is to obtain a similar material model for the "Numerical" model, the error between the two FE models' results needs to be established using the same material model from table 4.1 for both models. During this study, each indentation test's "Experimental"- and "Numerical" model were given the same material model from table 4.1. The "Numerical" model's nodal displacements, minimum - and maximum principal strains were fitted to that of the "Experimental" model's respectively. The aim of this study is to establish the error between the two models before optimisation and to validate the data capturing and interpolation portion of the numerical pipeline. Three different error measures were used for validation, R^2, RMS and Standard Error of Estimation (SEOE). The R^2 is

to determine how well the two models fit, where the RMS error is determined to obtain a reference towards the objective function during optimisation and the SEOE, represented in Eq. 5.7, was an extra measure to determine the average error between the two models.

$$SEOE = \frac{1}{M}\sum_{m=1}^{M}\sqrt{\frac{\sum_{j=1}^{n}\left(d_{NUM_j}(m) - d_{EXP_j}(m)\right)^2}{n-2}} \tag{5.7}$$

5.2.1 One Perpendicular Cylindrical Indenter

Typically during inverse FE analysis, the difference between the nodal displacements is minimised to match the two sets of results. With this method it is assumed that if the two sets of results are matched and optimised using the nodal displacements, all the other data from the nodal points will match to the same degree.

From table 5.1 and figure 5.2, the displacements produced acceptable results. Each displacement direction produced a near perfect fit with an R^2 value of more than 99% with the Z-direction performing the best. Using one perpendicular cylindrical indenter, will produce a minimum objective function of 0.0232. The optimisation algorithm needs to find an equivalent RMS error for the objective function, or smaller. If a smaller value can be obtained then it might be possible that a better material model is then obtained, but it should be noted that more than one set of parameters exist for a hyper-elastic material described by a Mooney-Rivlin material model. The SEOE error for each direction is smaller than 3%, meaning the "Numerical" model is able to predict the "Experimental" model's behaviour, if the correct material model is used for the "Numerical" model. The results validate that the interpolation procedure is accurate enough to be used during the optimisation procedure.

Table 5.1: Results of the errors for the sensitivity analysis between the two FE models for the one perpendicular cylindrical indenter

	R^2	RMS	SEOE
X-displacement	0.9987	0.0110	0.0144
Y-displacement	0.9989	0.0095	0.0286
Z-displacement	0.9999	0.0024	0.0072
Min. principal strain	0.9956	0.0032	0.0029
Max. principal strain	0.9872	0.0038	0.0108

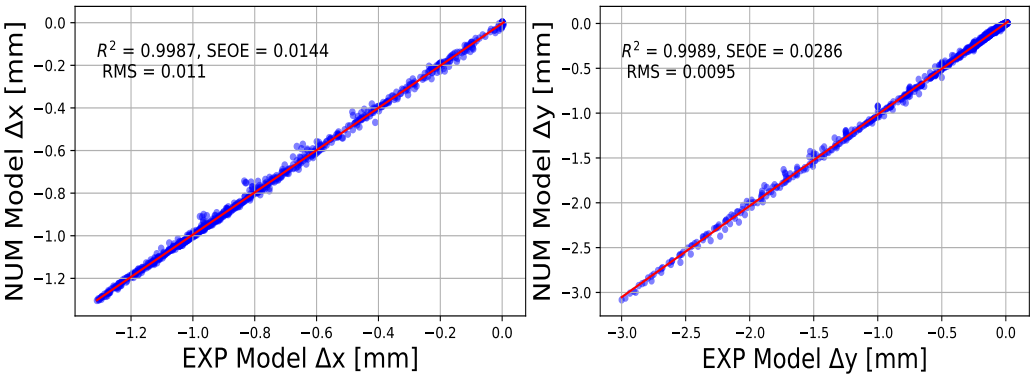

(a) X-displacement (b) Y-displacement

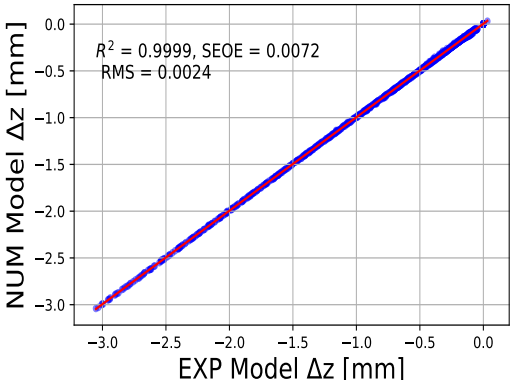

(c) Z-displacement

Figure 5.2: Displacement errors for the "Experimental" model vs. the "Numerical" model for the one perpendicular cylindrical indenter

Looking at figure 5.3 and again at table 5.1, the "Numerical" model does not predict the minimum and maximum principal strains as well as the displacements. The R^2 fit for each principal strain is still an acceptable value of more than 98%. Oddly enough the RMS and SEOE errors are better than those of the X - and Y - directions respectively. It is also noted that it is only in the last three increments that the strain values are less accurate, but the displacements have more points to calculate the errors. The lack in accuracy in the last few increments can be explained by referring to the contact tolerance within the FE models. Due to the coarser mesh within the "Numerical" model, the contact tolerance between the "skin" elements and the sample elements becomes slightly less accurate since there are fewer nodes available for contact detection, hence the error obtained. Nearly perfect fits might be obtained up until an indentation depth of 2 mm, therefore with a less complex deformation field. The results are of acceptable accuracy and the "Numerical" model does not need adjusting.

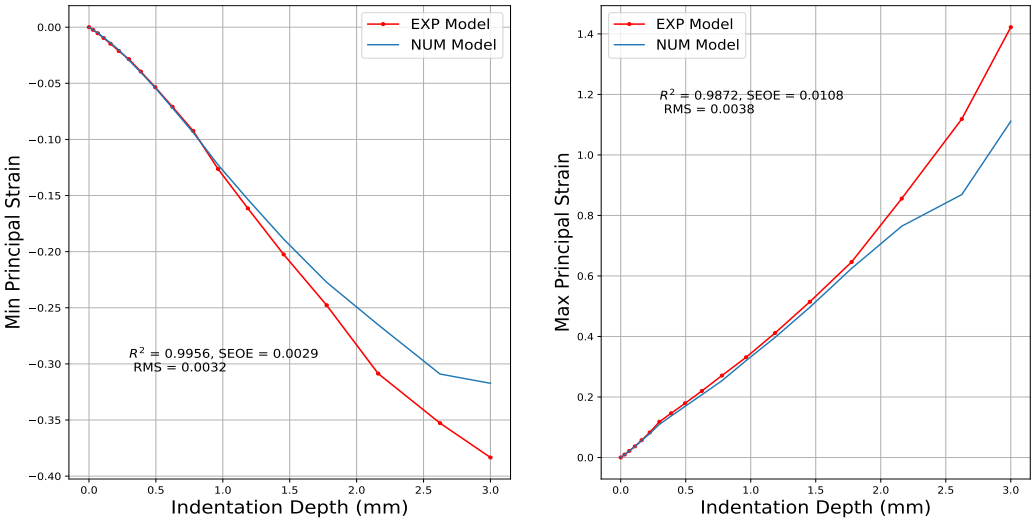

(a) Min. principal strain vs. indentation depth

(b) Max. principal strain vs. indentation depth

Figure 5.3: Min.- and Max. principal strain vs. indentation depth for the "Experimental" model vs. the "Numerical" model for the one perpendicular cylindrical indenter

5.2.2 Two Perpendicular Cylindrical Indenters

From table 5.2 and figure 5.4 the Z - direction obtained a perfect fit with regards to the R^2 value. The "Numerical" model is able to predict the "Experimental" model nearly perfectly within the Z - direction with RMS and SEOE errors of less than 1%. The X - and Y - directions are slightly less accurate, but still obtained nearly perfect fits of more than 99%. A minimum objective function of 0.2217 can be obtained by using two perpendicular cylindrical indenters, which is more than using only one indenter. This is due to the more complex displacement field obtained by the two indenters. The SEOE error is less than 4% for each direction, which is an acceptable error. The "Numerical" model will therefore be able to describe the "Experimental" model with the correct material model.

Table 5.2: Results of the errors for the sensitivity analysis between the two FE models for the two perpendicular cylindrical indenters

	R^2	RMS	SEOE
X-displacement	0.9982	0.0212	0.0377
Y-displacement	0.9975	0.0128	0.0384
Z-displacement	1.0	0.0022	0.0073
Min. principal strain	0.9854	0.0051	0.009
Max. principal strain	0.9222	0.0039	0.0134

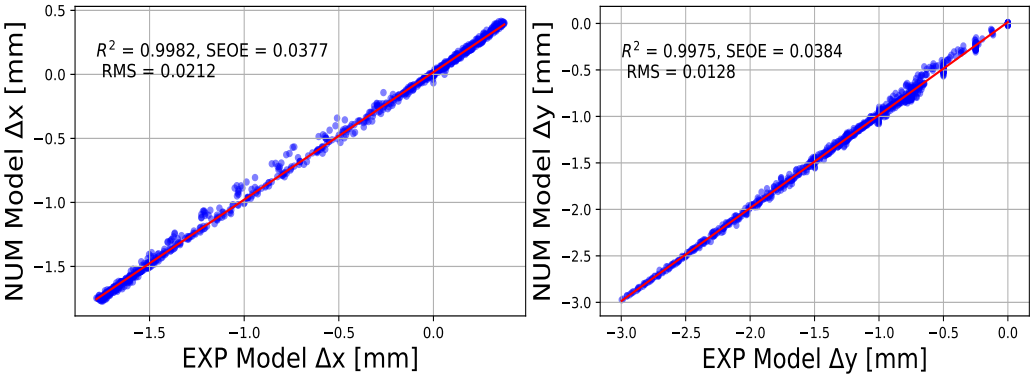

(a) X-displacement

(b) Y-displacement

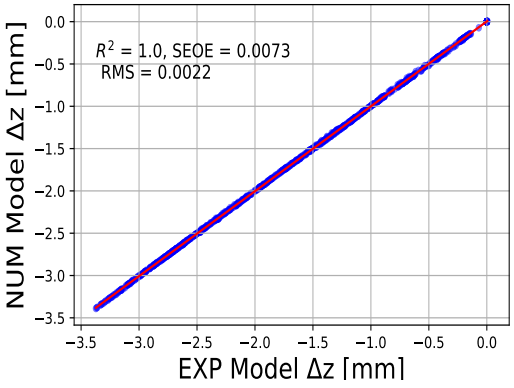

(c) Z-displacement

Figure 5.4: Displacement errors for the "Experimental" model vs. the "Numerical" model for the two perpendicular cylindrical indenters

Within figure 5.5 and table 5.2 it can be seen that the both principal strains obtained a less accurate fit compared to the displacements. The R^2 fit for both the minimum - and maximum principal strains obtained acceptable results of more than 98.5% and 2.2

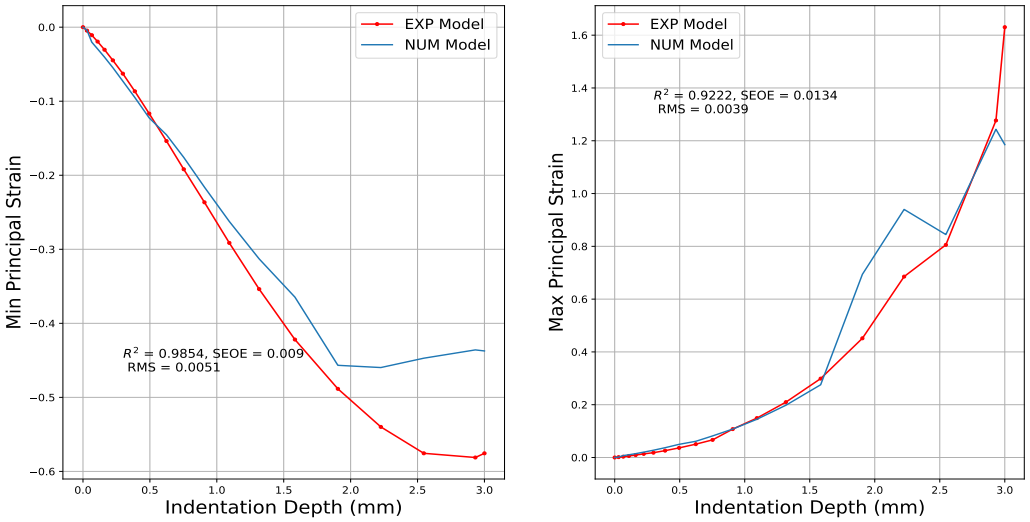

(a) Min. principal strain vs. indentation depth

(b) Max. principal strain vs. indentation depth

Figure 5.5: Min.- and Max. principal strain vs. indentation depth for the "Experimental" model vs. the "Numerical" model for the two perpendicular cylindrical indenters

5.2.3 Parallel Cylindrical Indenter

The parallel cylindrical indenter causes the most complex deformation field from all the indentation tests in this thesis. It is therefore expected to find SEOE errors up to 7.8% for the Y - direction. From figure 5.6 it can be seen that some nodes do not fit as well in the Y - direction as those in the X - and Z - direction, hence the larger SEOE and RMS errors. The R^2 fit is of an acceptable value of approximately 98% within the Y - direction and nearly perfect fits within the X - and Z - directions. A minimum objective function of 0.0431 was obtained. The "Numerical" model will be able to describe the "Experimental" model given the correct material model, but with a higher error in the Y - direction as can be seen in table 5.3.

Table 5.3: Results of the errors for the sensitivity analysis between the two FE models for the parallel cylindrical indenter, indentation test

	R^2	RMS	SEOE
X-displacement	0.9987	0.0124	0.047
Y-displacement	0.9867	0.0261	0.0783
Z-displacement	0.9999	0.0046	0.0085
Min. principal strain	0.5689	0.0149	0.0177
Max. principal strain	0.8911	0.0181	0.0978

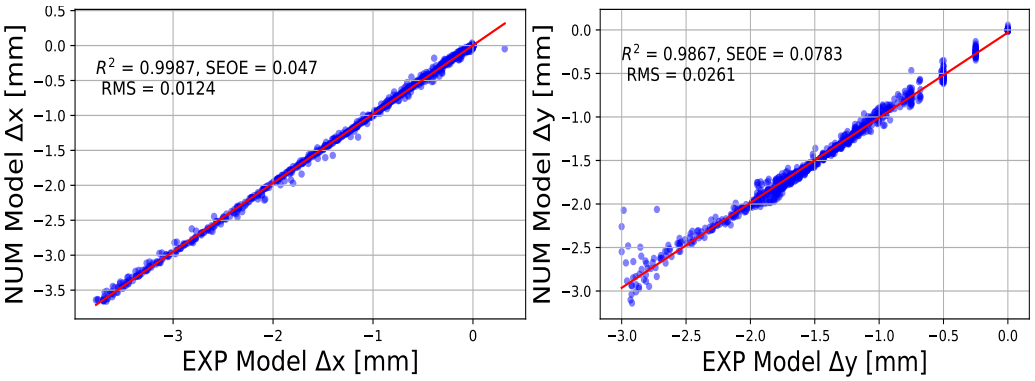

(a) X-displacement

(b) Y-displacement

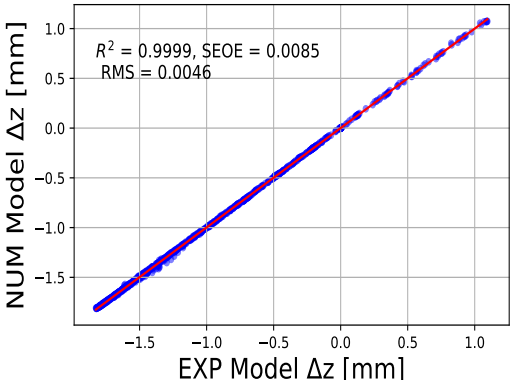

(c) Z-displacement

Figure 5.6: Displacement errors for the "Experimental" model vs. the "Numerical" model for the parallel cylindrical indenter

From table 5.3 and figure 5.7 it can be seen that the "Numerical" model does not fit the "Experimental" model very well. In terms of the minimum principal strain, an average fit of approximately 56% was obtained, but oddly enough both RMS and SEOE errors obtained values less than 2%. Again the R^2 value is a more accurate representation to describe the fit between the two models for the strain values. The maximum principal strain obtained a good fit up until the last two increments. The large difference in the last increments caused a 9.78% SEOE error, while the R^2 fit obtained a respectable 89.11%, which cannot be redeemed acceptable. The results were attempted to be improved by increasing the contact tolerance within the "Numerical" model for the glueing contact between the "skin" elements and the sample elements. Unfortunately the increase in the contact tolerance increases the distortion within the stiffness matrix of the material model. The results obtained in figure 5.7 were the best attempt in adjusting the "Numerical" model before the contact tolerance caused a failed analysis. The optimisation procedure only uses the displacements to obtain an objective function, therefore the strain results do not affect the optimisation numerical pipeline. The "Numerical" model will be used as is, with a starting error

within the strain results. The study within appendix D, showed that with a slight adjustment within the material variables, an improvement within the principal strains is possible.

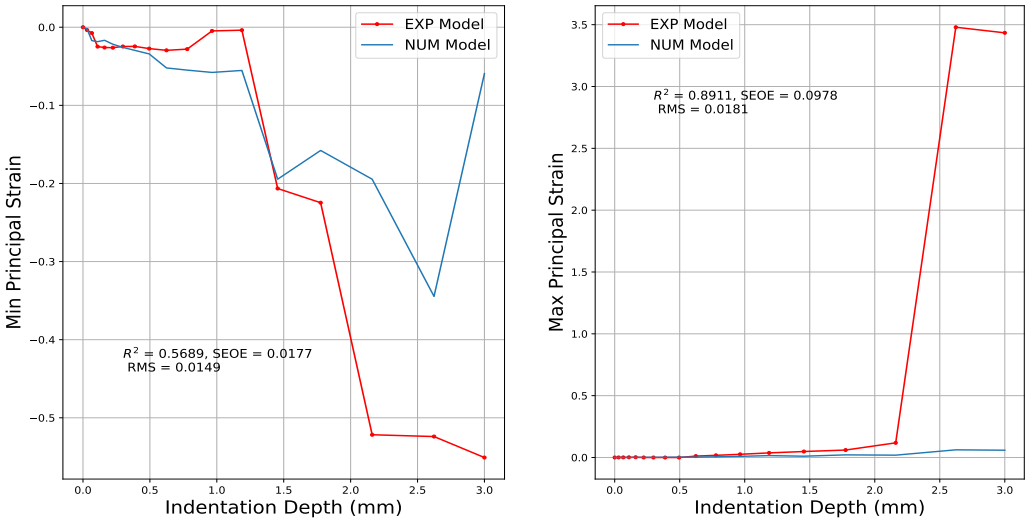

(a) Min. principal strain vs. indentation depth

(b) Max. principal strain vs. indentation depth

Figure 5.7: Min.- and Max. principal strain vs. indentation depth for the "Experimental" model vs. the "Numerical" model for the parallel cylindrical indenter

5.2.4 Diagonal Cylindrical Indenter

The diagonal indenter's unconventional orientation produces a slightly different deformation pattern. With this skew deformation the results produced acceptable and nearly perfect fits with R^2 values of more than 99% in all the displacement directions. Within all three displacement directions, RMS and SEOE errors were obtained less than 3%. A minimum objective function of 0.0199 was obtained, which is the best between the cylindrical indenters. Figure 5.8 and table 5.4 represent these nearly perfect results.

Table 5.4: Results of the errors for the sensitivity analysis between the two FE models for the diagonal cylindrical indenter

	R^2	RMS	SEOE
X-displacement	0.9992	0.0075	0.0182
Y-displacement	0.9987	0.009	0.027
Z-displacement	0.9999	0.0034	0.0086
Min. principal strain	0.9574	0.0038	0.0045
Max. principal strain	0.9988	0.0013	0.002

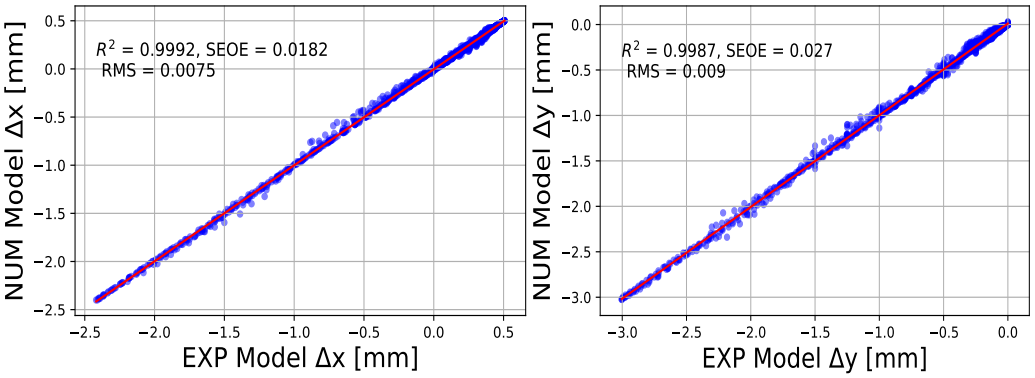

(a) X-displacement

(b) Y-displacement

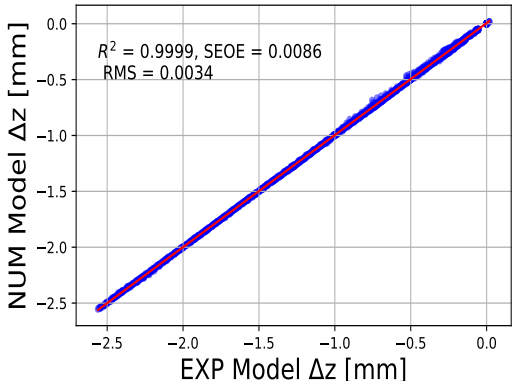

(c) Z-displacement

Figure 5.8: Displacement errors for the "Experimental" model vs. the "Numerical" model for the diagonal cylindrical indenter

From figure 5.9 and table 5.4 it can be seen that the diagonal indenter obtained a nearly perfect R^2 fit for the maximum principal strain of 99.9%. The minimum principal strain did not obtain a nearly perfect fit, but it did obtain an acceptable fit of 95.74%. The RMS and SEOE errors are all below 1%. It can

be concluded that the "Numerical" model will be able to describe the "Experimental" model with fairly accurate results, not just within the displacements, but within the strains as well, given the correct material model.

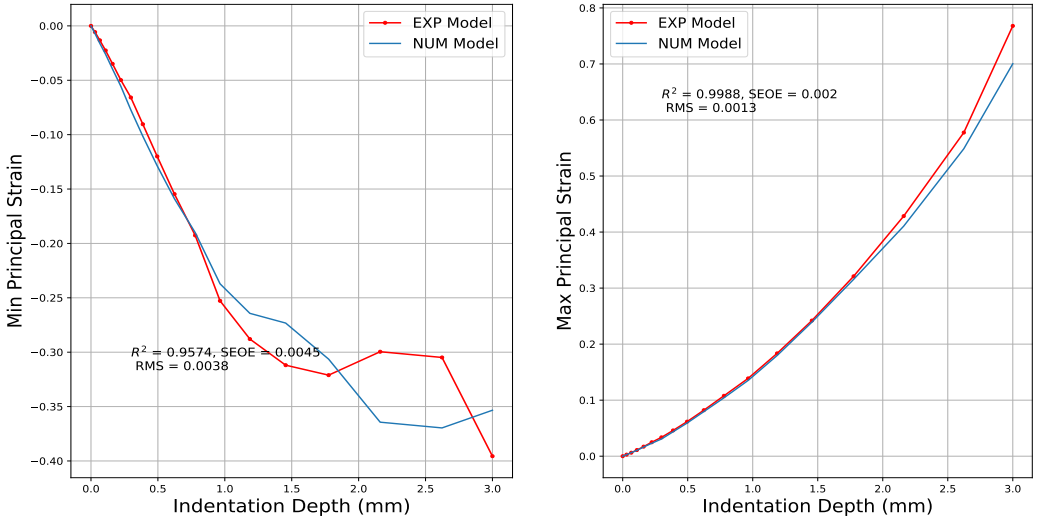

(a) Min. principal strain vs. indentation depth

(b) Max. principal strain vs. indentation depth

Figure 5.9: Min.- and Max. principal strain vs. indentation depth for the "Experimental" model vs. the "Numerical" model for the diagonal cylindrical indenter

5.2.5 One Spherical Indenter

A spherical indenter does not produce a very complex deformation field within the whole sample, but locally it causes a complex field. Within all three directions, a nearly perfect R^2 fit was obtained of more than 99% for the displacements. In table 5.5 the RMS and SEOE errors all obtained values less than 3%. An overall minimum objective function of 0.0339 was obtained. Within figure 5.10 it can be seen that most of the points are located at a Y - displacement below 1.5 mm. This is because of the smaller surface area of the spherical indenter. The "Numerical" model will be able to predict the behaviour of the "Experimental" model accurately, given the correct material model.

Table 5.5: Results of the errors for the sensitivity analysis between the two FE models for the one spherical indenter

	R^2	RMS	SEOE
X-displacement	0.9956	0.0193	0.0173
Y-displacement	0.9986	0.0098	0.0229
Z-displacement	0.9998	0.0048	0.0064
Min. principal strain	0.4214	0.0151	0.0178
Max. principal strain	0.7157	0.0206	0.1378

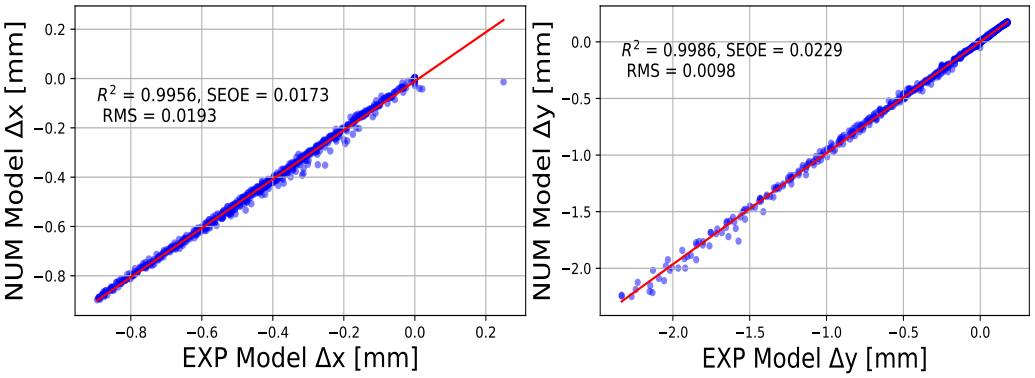

(a) X-displacement

(b) Y-displacement

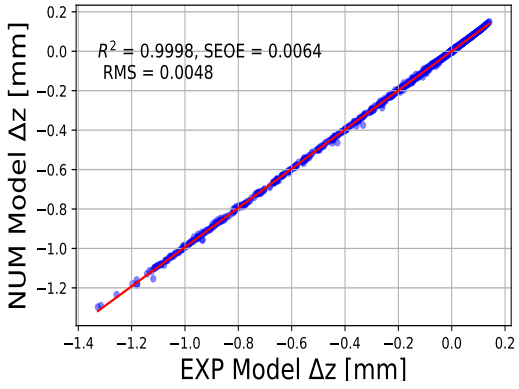

(c) Z-displacement

Figure 5.10: Displacement errors for the "Experimental" model vs. the "FE" model for the one spherical indenter

From figure 5.11 and table 5.5 it can be seen that the model does not produce acceptable results for the minimum - and maximum principal strains. The RMS and SEOE errors obtained are all smaller than 2% , but the R^2 fit for the minimum principal strain is only 42.14%. The maximum principal strain obtained an average fit of 71.57%, but possesses an SEOE error of 13.78%. With regard to the

strain results, the one spherical indenter does not produce acceptable results. The contact tolerance can be adjusted to improve the results, although adjusting it too much leads to a failed FE analysis due to the stiffness matrix failing. The results obtained within figure 5.11 were the best attempt. The optimisation procedure will not be affected since only the displacements are used for the numerical pipeline. It was therefore decided to use the model even though the strains will not produce acceptable results. The study within appendix D did, however, show that an improvement within the principal strain results can be obtained with a new material model.

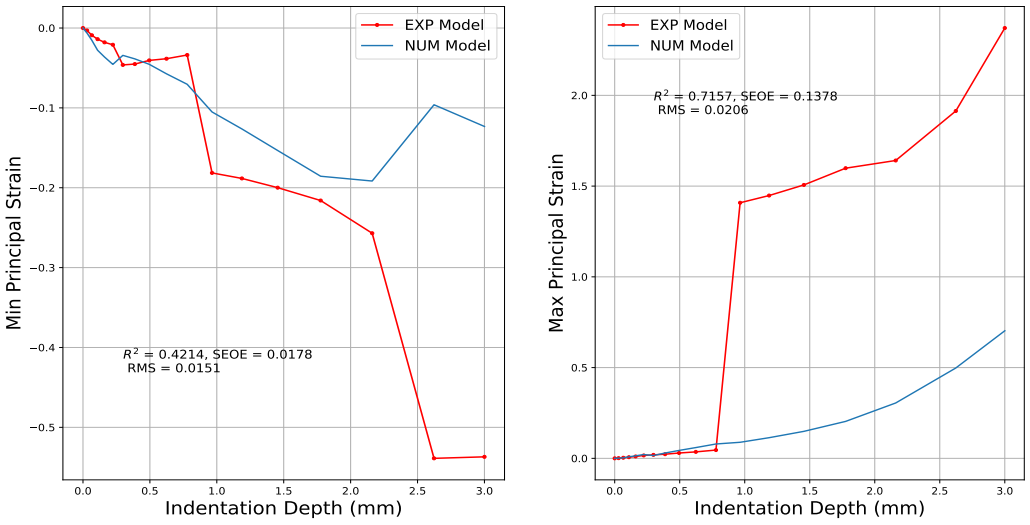

(a) Min. principal strain vs. indentation depth

(b) Max. principal strain vs. indentation depth

Figure 5.11: Min.- and Max. principal strain vs. indentation depth for the "Experimental" model vs. the "Numerical" model for the one spherical indenter

5.2.6 Two Spherical Indenters

The two spherical indenters obtained a nearly perfect R^2 fit of more than 99% within each displacement direction. In table 5.6 it can be seen that the Y - displacement obtained the largest SEOE error of 2.89% and the Z - displacement the smallest with 0.95%. The RMS errors are all below 1.5% with a minimum objective function of 0.0352. It can be concluded that the "Numerical" model will be able to match the "Experimental" model if the correct material model is given. Figure 5.12 shows the nearly perfect fit for all three displacements.

Table 5.6: Results of the errors for the sensitivity analysis between the two FE models for the two spherical indenter

	R^2	RMS	SEOE
X-displacement	0.9987	0.0144	0.018
Y-displacement	0.9973	0.0132	0.0289
Z-displacement	0.9996	0.0076	0.0095
Min. principal strain	0.727	0.0093	0.0094
Max. principal strain	0.7082	0.0101	0.0188

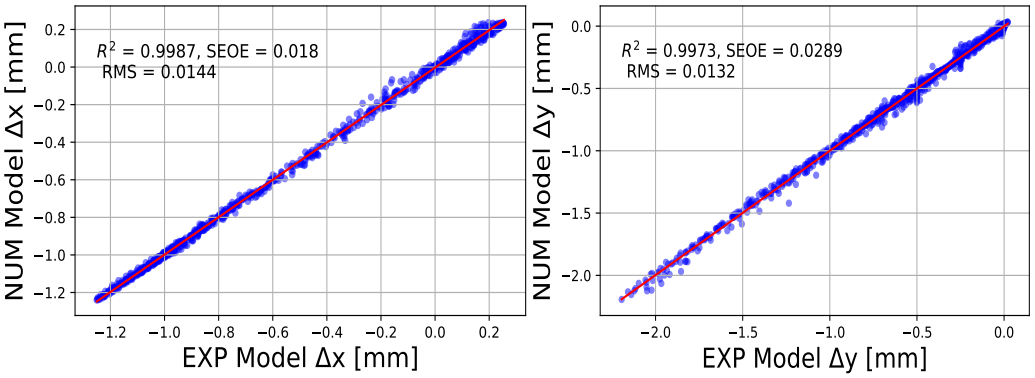

(a) X-displacement

(b) Y-displacement

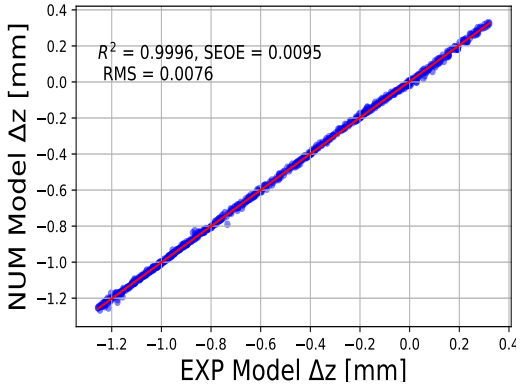

(c) Z-displacement

Figure 5.12: Displacement errors for the "Experimental" model vs. the "Numerical" model for the two spherical indenters

From table 5.6 and figure 5.13 the minimum - and maximum principal strains obtained average R^2 fits of 72.7% and 70.8% respectively. This is not an acceptable fit, but is an improvement from the one spherical indenter indentation test. It can therefore be noted that more than one spherical indenter can improve the strain results. The RMS and SEOE errors are below 2% which is an acceptable

match. It is still clear that the R^2 value is a better indication for how accurately the two models match with regard to the principal strains. The error between the two models only increases with the last three increments, which can be an indication that the contact tolerance was not sufficient between the "skin" elements and the sample elements within the coarser mesh of the "Numerical" model. Unfortunately a higher contact tolerance will lead to more distortion within the stiffness matrix and the mesh generator within the remeshing procedure. However, from figure 5.13 it can be seen that up to approximately 2 mm, the "Numerical" model describes the "Experimental" model with a higher accuracy. The strain results will not have an affect on the optimisation procedure, therefore the model will be used as is. The study within appendix D did, however prove that and improvement within the strain analysis can be obtained with a new material model.

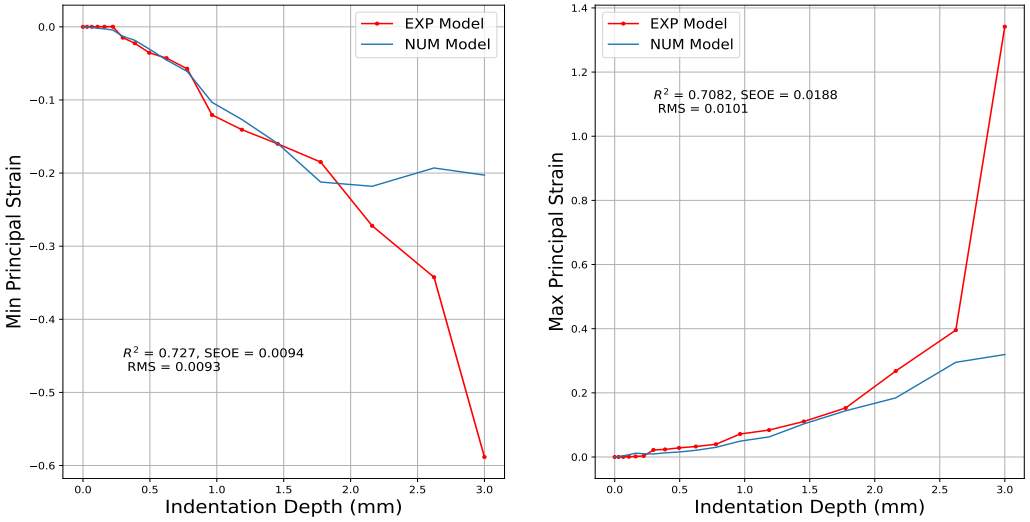

(a) Min. principal strain vs. indentation depth

(b) Max. principal strain vs. indentation depth

Figure 5.13: Min.- and Max. principal strain vs. indentation depth for the "Experimental" model vs. the "Numerical" model for the two spherical indenters

5.3 Summary

This chapter discussed how the Mooney-Rivlin three parameter material model can be used to extrapolate strain data within the compression and tensile region to obtain a relationship between the stretch and engineering stress. A sensitivity study was done between the two FE models within each indentation test. This study aimed to determine the error between the FE models using the same material model. The results validated that the data capturing and interpolation part of the numerical pipeline is working. The results also validated that the two FE models within each indentation test will obtain nearly the same displacements,

thus ensuring that both models are the same. All six indentation tests were able to produce acceptable and nearly perfect fits between the "Numerical" model and the "Experimental" model within each displacement direction. In each indentation test the Z - displacement obtained the best R^2 fit and smallest RMS and SEOE error. The strain results were not as successful in each indentation case. The parallel cylindrical indenter and both spherical indentation test did not obtain acceptable principal strain fits. It was concluded that this is due to the glueing contact tolerance between the "skin" elements and the sample elements within the coarse meshed "Numerical" models. The glueing contact tolerance effect the results within the "Experimental" model as well, but from a relative perspective, the problem persists in the "Numerical" model, since it is compared to the "Experimental" model. All three models were adjusted as best as possible, but too much adjustment caused failed FE analysis due to the increased distortion in the stiffness matrix. Within the numerical pipeline, only the displacements are used for the optimisation procedure, therefore the strains does not effect the credibility of the numerical pipeline and the "Numerical" models for these three indentation tests can be used as is. In Appendix D a sensitivity study was done on the material model and the effect the three material variables have on the principal strain results as well as the stretch vs. engineering strain relationship. This study showed that the material model's variables greatly affect the principal strain results. Therefore a possibility for improvement in the fit between the "Experimental" model and "Numerical" model's principal strain results, for the parallel cylindrical indenter and spherical indenters, is possible.

From the validation tests a few conclusions can be made in order to set a baseline for the final results. The numerical pipeline is performing and obtaining the results as expected, therefore the pipeline does not need adjustments. Within each of the indentation tests, the displacement results from the "Numerical" model fit the results from the "Experimental" model accurately. The displacements therefore need to obtain an R^2 fit of minimum 0.9500, to be classified as an acceptable fit. The parallel cylindrical indenter resulted in the most complex deformation field. Within the validation tests, a baseline for the R^2 fit within the principal strains was set at 0.9000. This validated which FE model resulted in acceptable results. This baseline will be used for the final tests as well. The parallel cylindrical indenter obtained the largest principal strain range of approximately -0.54 - 3.45, which is a stretch of 0.46 - 4.45, within the "Experimental" model.

Chapter 6

Indentation Tests

This chapter discusses the test procedure used during each indentation test, followed by the best results obtained for each indentation test with the SLP and SQP optimisation algorithms respectively. Finally, each subsection will present the best material model obtained using the SLP and SQP algorithm respectively.

All the indentation tests were simulated with 20 mm x 20 mm x 5 mm square test samples. The cylindrical indenters possessed a radius of 3 mm and a length of 30 mm, except for the diagonal indenter which has a length of 35 mm. All the spherical indenters possessed a radius of 3 mm. Within the FE models the indenter was displaced 3 mm within the negative Y - direction over a time period of 1 s. All boundary conditions and contact analyses were applied as explained in chapter 3. The numerical pipeline, explained in chapter 4, was used to obtain a material model for the "Numerical" model, optimised to fit the results obtained from the "Experimental" model. The results for each indentation test below are only for the best material model obtained from the 10 optimised sets within each indentation test.

6.1 One Perpendicular Cylindrical Indenter

From the results in table 6.1, it is clear that the SLP algorithm successfully obtained a material model which matched the displacements with a near perfect fit within all three directions. It can be observed that the Y - displacement obtained a better fit than the original model within chapter 5, table 5.1. An overall objective function of 0.0228 was obtained for this solution, which is a smaller objective function obtained by the original material model.

Table 6.1: Errors obtained for the best design point, for a 3 mm indentation with a one perpendicular cylindrical indenter, using the SLP optimisation algorithm

	R^2	RMS	SEOE
X-displacement	0.9986	0.0122	0.0161
Y-displacement	0.9993	0.0065	0.0194
Z-displacement	0.9999	0.0025	0.0076
Min. principal strain	0.9924	0.0035	0.0030
Max. principal strain	0.9964	0.0027	0.0090
Engineering stress	0.9880	0.0006	0.0449

The results in table 6.2, represent the displacement results for the material model with the smallest objective function obtained from the SQP optimisation algorithm. Here the SQP algorithm obtained a material model which obtained a better fit for the Y - displacement and nearly the same values for the X - and Z - displacements to that of the original model. An objective function of 0.0226 was obtained. The SQP algorithm obtained a smaller objective function than the SLP algorithm.

Table 6.2: Errors obtained for the results with the smallest objective function, for a 3 mm indentation with one perpendicular cylindrical indenter, using the SQP optimisation algorithm

	R^2	RMS	SEOE
X-displacement	0.9986	0.0111	0.0145
Y-displacement	0.9993	0.0065	0.0196
Z-displacement	0.9999	0.0023	0.0072
Min. principal strain	0.9878	0.0040	0.0032
Max. principal strain	0.9974	0.0026	0.0088
Engineering stress	0.9996	0.0002	0.0168

Another material model was obtained by the SQP algorithm, which obtained results with an equivalent fit to the displacement results obtained for the material model with the smallest objective function. The results for this material model can be found in table 6.3, where it can be observed that the X - displacement obtained a better fit than the material model with a smaller objective function. Overall this material model would have expected to possess the smallest objective function, but the overall objective function obtained for this material model was 0.0229, making it the material model with the largest objective function. Appendix E, visualises the displacement results for tables 6.1 - 6.3 in figures E.1 - E.3.

Table 6.3: Errors obtained for the results with the best curve fitting results, for a 3 mm indentation with one perpendicular cylindrical indenter, using the SQP optimisation algorithm

	R^2	RMS	SEOE
X-displacement	0.9980	0.0130	0.0171
Y-displacement	0.9994	0.0065	0.0195
Z-displacement	0.9999	0.0023	0.0071
Min. principal strain	0.9941	0.0032	0.0027
Max. principal strain	0.9972	0.0028	0.0093
Engineering stress	0.9993	0.0001	0.0062

Figure 6.1 represents the engineering stress vs. stretch, obtained from Eq. 5.4, for the material models obtained by the SLP and SQP algorithms respectively, shown in table 6.4. As expected the material model with the smallest objective function from the SQP algorithm, fitted the "Experimental" model's curve better than the SLP algorithm's material model. Unexpectedly, the material model from table 6.3, obtained the best fit for the "Experimental" model engineering stress vs. stretch curve, while it possesses the largest objective function. Both material models obtained by the SQP algorithm fitted the "Experimental" model's curve for the entire stretch range, but the SLP algorithm's material model only fitted for an approximate range of 0.6 - 2.0 stretch.

Table 6.4: Optimised Mooney-Rivlin parameter, obtained from the SLP - and SQP optimisation algorithms respectively, for the one perpendicular cylindrical indenter

Optimisation algorithm	C_{10} [MPa]	C_{01} [MPa]	C_{20} [MPa]	Objective function
SLP	0.208454	0.078040	0.046001	0.0228
SQP - Best objective function	0.223661	0.088311	0.056582	0.0226
SQP - Best fitted results	0.232402	0.091010	0.060749	0.0229

In figure 6.2 it can be seen that all three material models from table 6.4 under determined both the minimum - and maximum principal strains. The error within the last three increments was established in chapter 5 as a result from the contact tolerance within the "Numerical" model. Disregarding the contact error, it can be observed that the extra material model obtained by the SQP algorithm, obtained the best fit to the "Experimental" model for both principal strains. Another unexpected observation is that the material model from the SLP algorithm, obtained a better fit within the minimum principal strain to the material model

obtained by the SQP algorithm with the smallest objective function. It can be observed from table 6.4 that all three material models have quite different parameters. This is expected since the Mooney-Rivlin material model is a curve fitting equation and more than one set of parameters are bound to obtain similar results, while all of them fit the displacement field very well.

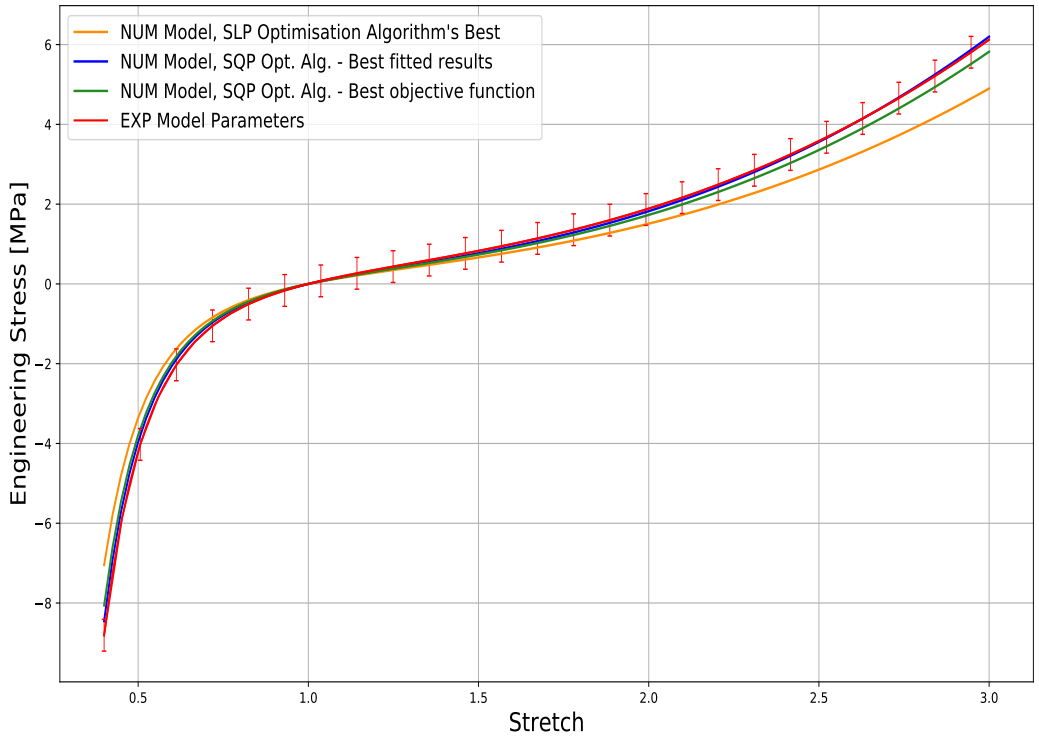

Figure 6.1: Engineering stress vs. stretch for the best results obtained from the SQP - and SLP optimisation algorithms, for the one perpendicular cylindrical indenter

Figure 6.3 represents the sorted progression for the objective functions obtained during the 10 optimisation procedures. The 10th optimisation run represents the best results obtained from the SLP - and SQP algorithms for the smallest objective functions, respectively. The third optimisation run represents the extra material model obtained by the SQP algorithm. It can be observed that the material model with the best objective function, does not guarantee the best material model to fit the engineering stress vs. stretch or the principal strain curves.

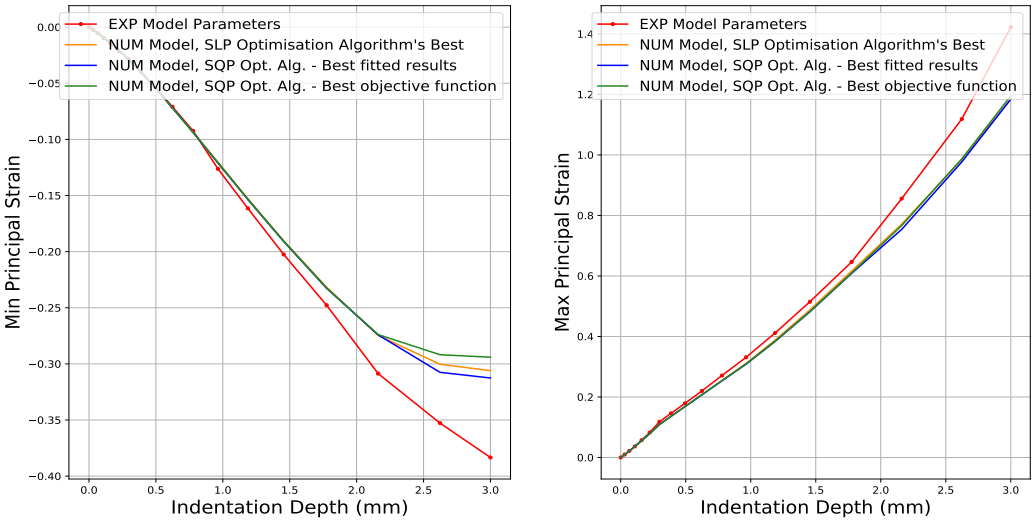

(a) Min. principal strain vs. indentation depth

(b) Max. principal strain vs. indentation depth

Figure 6.2: Min.- and Max. principal strain vs. indentation depth for the best results from the SLP - and SQP optimisation algorithms, for the one perpendicular cylindrical indenter

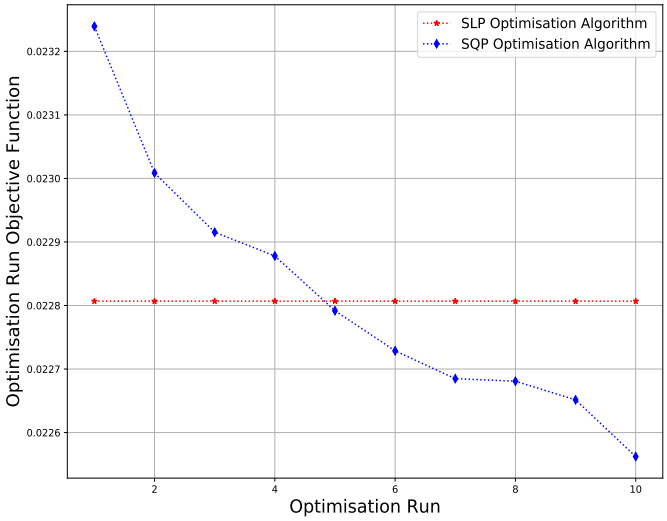

Figure 6.3: Objective functions for each of the 10 design points, obtained by both the SLP - and SQP algorithms, for the one perpendicular cylindrical indenter

6.2 Two Perpendicular Cylindrical Indenters

In table 6.5, the SLP algorithm obtained a material model which obtained nearly perfect displacement results within the X - and Y - directions and a perfect fit

within the Z - direction. An overall objection function of 0.2292 was obtained. Between the 10 design points, nine obtained the same material model and objective function after optimisation. Only one design point obtained a slightly different material model which produced an objective function larger than the other nine.

Table 6.5: Errors for the best design point results, for a 3 mm indentation with two perpendicular cylindrical indenters, using the SLP optimisation algorithm

	R^2	RMS	SEOE
X-displacement	0.9976	0.0246	0.0439
Y-displacement	0.9966	0.0165	0.0494
Z-displacement	1.0	0.0017	0.0057
Min. principal strain	0.9860	0.0051	0.0090
Max. principal strain	0.8765	0.0049	0.0176
Engineering stress	0.9880	0.0006	0.0449

In table 6.6 it is observed that the SQP algorithm obtained a material model which obtained nearly perfect fits within all three displacements. An overall objective function of 0.2153 was obtained, which is an improvement from the one obtained by the SLP algorithm. Compared to the original material model in chapter 5, this material model obtained a smaller objective function, but compared to the results from table 5.2, the smaller objective function did not guarantee better error results.

Table 6.6: Errors obtained for the results with the smallest objective function, for a 3 mm indentation with two perpendicular cylindrical indenters, using the SQP optimisation algorithm

	R^2	RMS	SEOE
X-displacement	0.9975	0.0458	0.0817
Y-displacement	0.9957	0.0179	0.0538
Z-displacement	0.9996	0.0193	0.0653
Min. principal strain	0.9839	0.0056	0.0087
Max. principal strain	0.9047	0.0051	0.0152
Engineering stress	0.9994	0.0004	0.0278

The SQP algorithm obtained another material model which obtained a better fit within the Y - and Z - displacements, as well as improved error results, shown in table 6.7. An overall objective function of 0.2185 was obtained by this material model, which is not an improvement from the previous SQP material

model, hence the unexpected observation with regards to the improved results within table 6.7. The displacement errors within tables 6.5 - 6.7 are depicted in figures E.4 - E.6 in appendix E.

Table 6.8 summarises the material models obtained from the SLP - and SQP algorithms. It is observed that the SLP algorithm obtained the same material model to the one cylindrical indenter test.

Table 6.7: Errors obtained for the results with the best curve fitting results, for a 3 mm indentation with two perpendicular cylindrical indenters, using the SQP optimisation algorithm

	R^2	RMS	SEOE
X-displacement	0.9973	0.0238	0.0425
Y-displacement	0.9965	0.0019	0.0456
Z-displacement	1.0	0.0152	0.0064
Min. principal strain	0.9845	0.0051	0.0087
Max. principal strain	0.9041	0.0045	0.0152
Engineering stress	1.0	0.0001	0.0045

Table 6.8: Optimised Mooney-Rivlin parameters, obtained from the SLP - and SQP optimisation algorithms respectively, for the two perpendicular cylindrical indenters

Optimisation algorithm	C_{10} [MPa]	C_{01} [MPa]	C_{20} [MPa]	Objective function
SLP	0.208454	0.078040	0.046001	0.2292
SQP - Best objective function	0.221657	0.090082	0.050867	0.2153
SQP - Best fitted results	0.261949	0.105881	0.058390	0.2185

In figure 6.4 the engineering stress vs. stretch curve indicates that the material model with the smallest objective function from the SQP algorithm, obtained a better fit to the material model obtained by the SLP algorithm. This is expected since the material model from the SQP algorithm obtained a smaller objective function. The extra material model, obtained by the SQP algorithm, obtained a perfect fit to the "Experimental" model's curve for the entire stretch region. It was expected to find an improved fit compared to the SLP algorithm's material model, but it was unexpected that the material model with the smallest objective function, from the SQP algorithm did not obtain a perfect fit. The material model from the SLP algorithm and the material model with the smallest objective function, fitted the "Experimental" model for an approximate 0.6 - 1.8 stretch range.

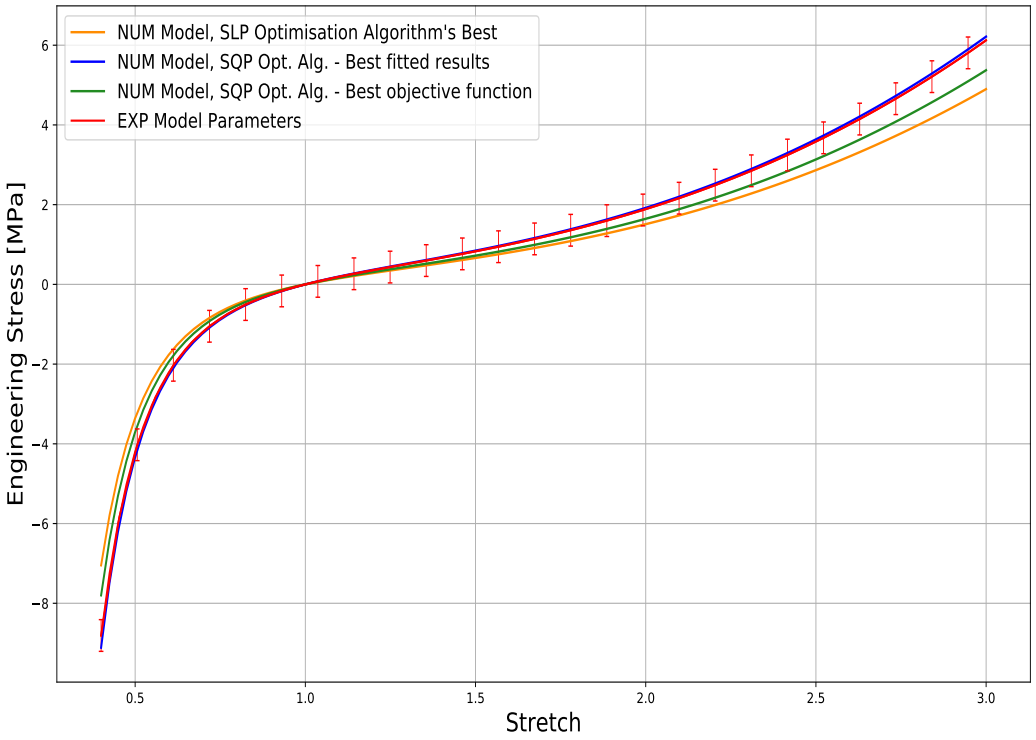

Figure 6.4: Engineering stress vs. stretch for the best results obtained from the SLP - and SQP optimisation algorithms, for the two perpendicular cylindrical indenters

From figure 6.5 it is observed that the extra material model from the SQP algorithm resulted in a better fit within the minimum principal strain and obtained the best error results, compared to the material model with the smallest objective function. The material model from the SLP algorithm obtained the largest objective function, but obtained a better fit within the minimum principal strain than the material model with the smallest objective function from the SQP algorithm. With regards to the maximum principal strain, the material model with the smallest objective function obtained by the SQP algorithm, obtained the best fit to the "Experimental" model's curve, which is expected. All three material models under determined both the principal strains.

Figure 6.6 represents the sorted objective function for each of the 10 optimised design points, obtained from both the SLP - and SQP algorithms. The eighth optimisation run represents the objective function obtained for the extra material model from the SQP algorithm. It can be observed that the material model with the smallest objective function does not guarantee the best curve fitting results within the engineering stress vs. stretch curve.

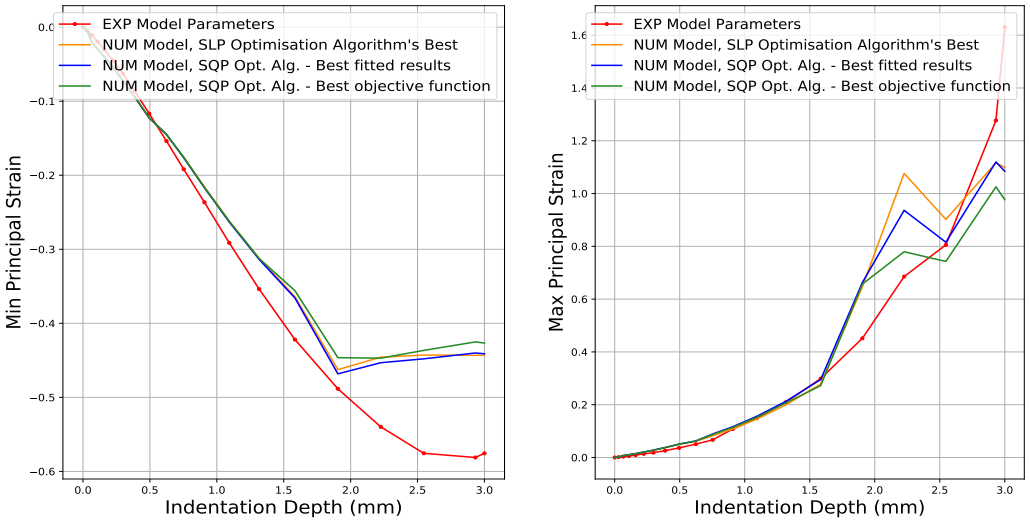

(a) Min. principal strain vs. indentation depth

(b) Max. principal strain vs. indentation depth

Figure 6.5: Min.- and Max. principal strain vs. indentation depth for the best results from the SLP - and SQP optimisation algorithms, for the two perpendicular cylindrical indenters

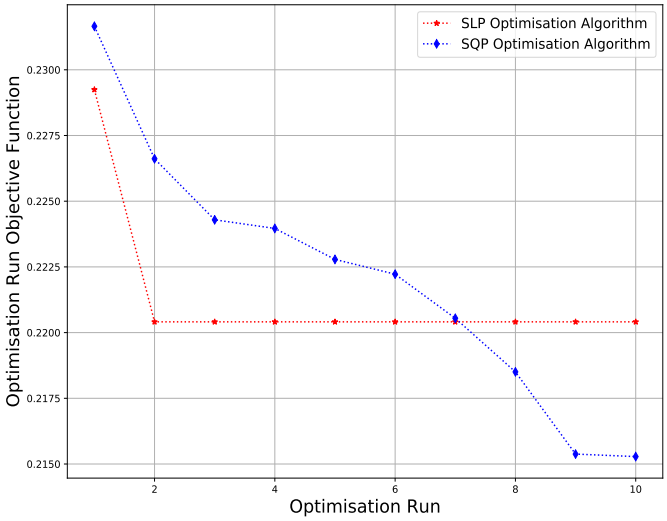

Figure 6.6: Objective functions for each of the 10 design points, obtained by both the SLP - and SQP algorithms, for the two perpendicular cylindrical indenters

6.3 Parallel Cylindrical Indenter

The results obtained for the SLP algorithm are displayed in table 6.9. The material model obtained by the SLP algorithm, obtained a better fit for the X - dis-

placement to the original model's within table 5.3. Acceptable displacement results were obtained, but the Y - displacement obtained quite a smaller R^2 fit of 93%, compared to the nearly perfect fits of more than 99% for the X - and Z - displacements. This means the Y - displacement failed to obtain an acceptably accurate fit. An overall objective function of 0.0837 was obtained for this material model.

Table 6.9: Errors obtained for the best design point results, for a 3 mm indentation with a parallel cylindrical indenter, using the SLP optimisation algorithm

	R^2	RMS	SEOE
X-displacement	0.9989	0.0096	0.0362
Y-displacement	0.9348	0.0597	0.1793
Z-displacement	0.9999	0.0047	0.0086
Min. principal strain	0.8940	0.0128	0.0171
Max. principal strain	0.6716	0.0178	0.0945
Engineering stress	0.9880	0.0006	0.0449

From table 6.10, it can be seen that the SQP algorithm obtained a material model which obtained nearly perfect displacement fits of more than 99% each. This material model obtained an overall objective function of 0.0791. This objective function is smaller to the original model's objective function in chapter 5. The two material models obtained by the SLP - and SQP algorithms respectively, are displayed in table 6.11. The displacement results are represented by figures E.7 - E.8 in appendix E.

Table 6.10: Errors obtained for the results with the smallest objective function, for a 3 mm indentation with a parallel cylindrical indenter, using the SQP optimisation algorithm

	R^2	RMS	SEOE
X-displacement	0.9992	0.0083	0.0313
Y-displacement	0.9949	0.0168	0.0505
Z-displacement	0.9999	0.0038	0.0070
Min. principal strain	0.8303	0.0161	0.0215
Max. principal strain	0.8462	0.0180	0.0974
Engineering stress	0.9993	0.0001	0.0058

Table 6.11: Optimised Mooney-Rivlin parameter, obtained from the SLP - and SQP optimisation algorithms respectively, for the parallel cylindrical indenter

Optimisation algorithm	C_{10} [MPa]	C_{01} [MPa]	C_{20} [MPa]	Objective function
SLP	0.208454	0.078040	0.046001	0.0837
SQP - Best objective function	0.296871	0.094198	0.052430	0.0791

Unlike the previous two indentation tests, the parallel cylindrical indenter did not obtain an extra material model with a better fit within the engineering stress vs. stretch results, observed in figure 6.7. The material model obtained by the SQP algorithm, obtained a nearly perfect R^2 fit of 99.93% for the engineering stress vs. stretch curve. This was expected since the material model from the SQP algorithm, obtained the smallest objective function.

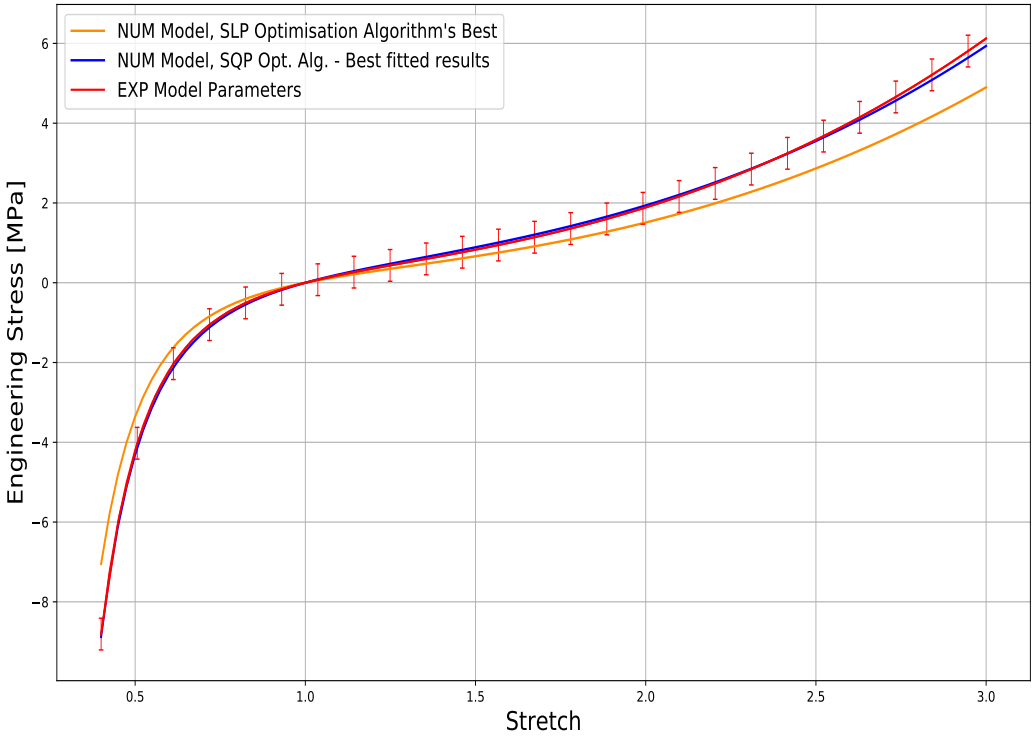

Figure 6.7: Engineering stress vs. stretch for the best results obtained from the SLP - and SQP optimisation algorithms, for the parallel cylindrical indenter

The results obtained for the principal strains can be visualised in figure 6.8. It can be observed that both the material models from the SLP - and SQP algorithms did not succeed in obtaining acceptable fitted results, which was established in chapter 5, as a result of poor contact detection within the "Numerical"

model. Both material models under determined the principal strains. Apart from the poor fit, it was observed that the SLP algorithm obtained a better fit and errors for the minimum principal strain. This was unexpected since the material model obtained by the SQP algorithm obtained a smaller objective function. However, it was expected to find a better fit for the material model obtained by the SQP algorithm within the maximum principal strain.

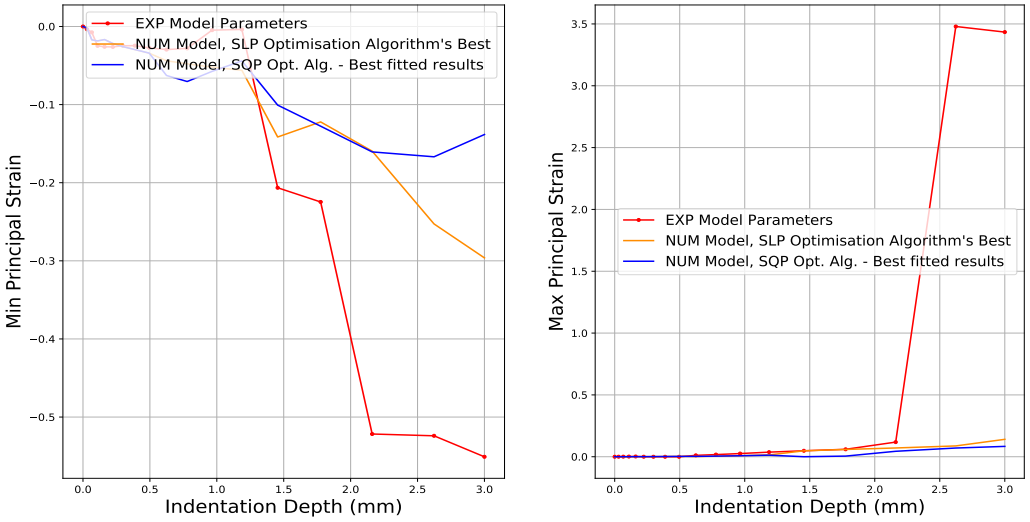

(a) Min. principal strain vs. indentation depth

(b) Max. principal strain vs. indentation depth

Figure 6.8: Min.- and Max. principal strain vs. indentation depth for the best results from the SLP - and SQP optimisation algorithms, for the parallel cylindrical indenter

Figure 6.9 showcases the sorted, best objective function obtained for each of the 10 optimisation runs. The SLP algorithm has obtained the same objective function for the 10 different optimised design points, hence the same material model. The SQP seems to obtain a wider range of different material models and objective functions.

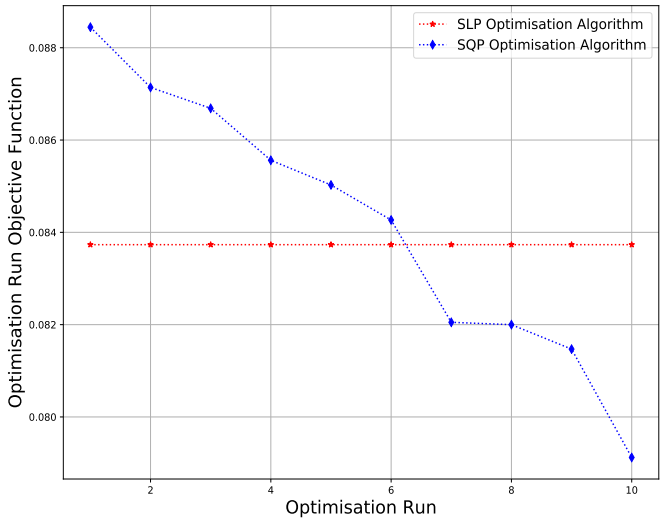

Figure 6.9: Objective functions for each of the 10 design points, obtained by both the SLP - and SQP algorithms, for the parallel cylindrical indenter

6.4 Diagonal Cylindrical Indenter

The SLP algorithm obtained a material model with an overall objective function of 0.0228. Within table 6.12, it is observed that nearly perfect displacements results of more than 99% each were obtained.

Table 6.12: Errors obtained for the best design point, for a 3 mm indentation with a diagonal cylindrical indenter, using the SLP optimisation algorithm

	R^2	RMS	SEOE
X-displacement	0.9991	0.0081	0.0197
Y-displacement	0.9987	0.0092	0.0277
Z-displacement	0.9999	0.0036	0.0093
Min. principal strain	0.9698	0.0033	0.0035
Max. principal strain	0.9983	0.0013	0.0019
Engineering stress	0.9880	0.0006	0.0449

The SQP algorithm obtained a material model with and overall objective function of 0.0218. Within table 6.13 it is observed that this material model obtained nearly perfect fits of more than 99% for each displacement. These results are better than the results obtained by the SLP algorithm, which is expected due to the smaller objective function. This material model obtained better results than the original model within table 5.4.

Table 6.13: Errors obtained for the results with the smallest objective function, for a 3 mm indentation with a diagonal cylindrical indenter, using the SQP optimisation algorithm

	R^2	RMS	SEOE
X-displacement	0.9994	0.0063	0.0152
Y-displacement	0.9987	0.0095	0.0285
Z-displacement	0.9999	0.0033	0.0085
Min. principal strain	0.9654	0.0035	0.0039
Max. principal strain	0.9877	0.0019	0.0038
Engineering stress	0.9998	0.0003	0.0167

From table 6.14 it can be observed that another material model was obtained by the SQP algorithm which obtained better fits within the displacement results, but an overall objective function of 0.0220 was obtained. Table 6.15 summarises the material models obtained by the optimisation algorithms. It can be observed that the material model obtained for the SLP algorithm, has the same set of parameters obtained for the previous cylindrical indenter tests. Figures E.9 - E.11, in appendix E, represent the displacement errors obtained within tables 6.12 - 6.14.

Table 6.14: Errors obtained for the results with the best curve fitting results, for a 3 mm indentation with a diagonal cylindrical indenter, using the SQP optimisation algorithm

	R^2	RMS	SEOE
X-displacement	0.9996	0.0056	0.0135
Y-displacement	0.9988	0.0089	0.0269
Z-displacement	0.9999	0.0036	0.0091
Min. principal strain	0.9628	0.0036	0.0041
Max. principal strain	0.9981	0.0012	0.0017
Engineering stress	0.9998	0.0001	0.0033

Table 6.15: Optimised Mooney-Rivlin parameter, obtained from the SLP - and SQP optimisation algorithms respectively, for the diagonal cylindrical indenter

Optimisation algorithm	C_{10} [MPa]	C_0 [MPa]	C_{20} [MPa]	Objective function
SLP	0.208454	0.078040	0.046001	0.0228
SQP - Best objective function	0.252613	0.091769	0.050992	0.0218
SQP - Best fitted results	0.280362	0.092507	0.054244	0.0220

In figure 6.10, unexpected results can be observed. The extra material model obtained by the SQP algorithm, obtained a nearly perfect fit within the standard error of the "Experimental" model's engineering stress vs. stretch curve, over the entire stretch range. The material model with the smallest objective function from the SQP algorithm, fitted the "Experimental" model within the standard error for an approximate range of 0.4 - 2.7 stretch. The SLP algorithm fitted the "Experimental" model within the standard error for an approximate range of 0.7 - 2.2 stretch. The results from the SLP algorithm's material model were expected, since it possessed the largest objective function.

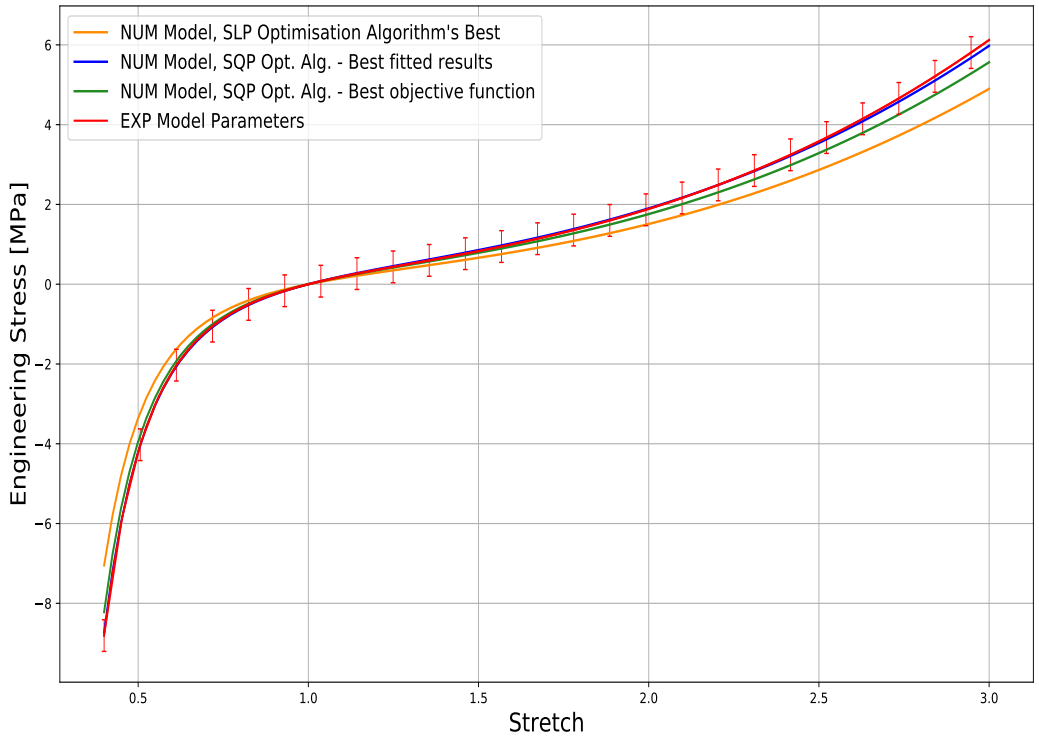

Figure 6.10: Engineering stress vs. stretch for the best results obtained from the SQP - and SLP optimisation algorithms, for the diagonal cylindrical indenter

In figure 6.11, all three material models in table 6.15 under determined the final strain results for both the principal strains. This error is due to the contact detection within the coarse mesh of the "Numerical" model. With the contact error present, the results obtained were of an acceptable fit. For the minimum principal strain, all three material models obtained an R^2 fit of more than 96%, with the SLP algorithm performing the best with an R^2 value of 96.98%. For the maximum principal strain, the SLP algorithm obtained the best R^2 fit of 99.83%, followed by the extra material model obtained from the SQP algorithm with an R^2 value of 99.81%. These results were unexpected since the material model with the largest objective function obtained the best fit between all three material models. A quick observation can be made between the shape of the curve obtained within the minimum principal strain, for the material model with the smallest objective function obtained by the SQP algorithm. The shape of this curve is the same as the curve obtained by the "Numerical" model for the original material model in figure 5.9. Indirectly this material model found the perfect fit, compared to the optimum potential the "Numerical" analysis possesses.

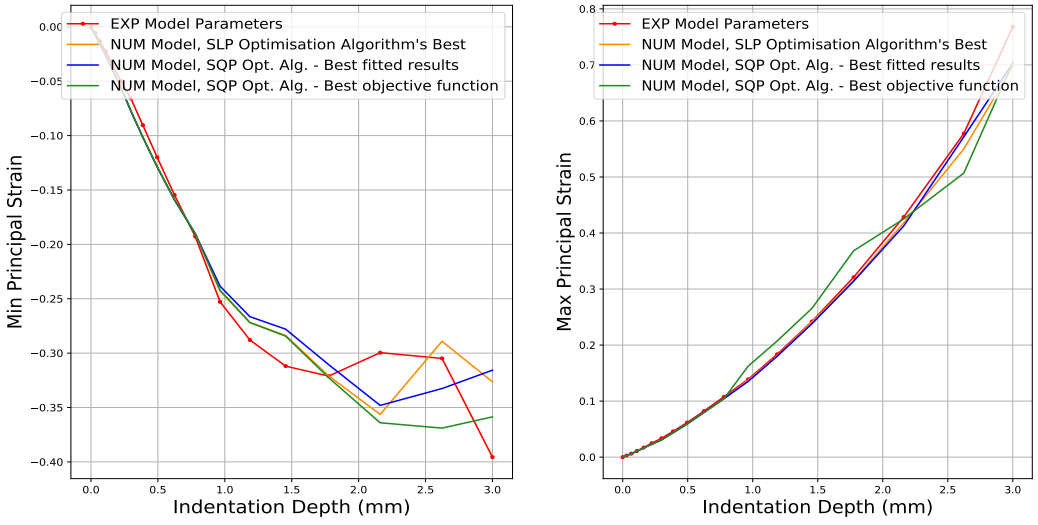

(a) Min. principal strain vs. indentation depth

(b) Max. principal strain vs. indentation depth

Figure 6.11: Min.- and Max. principal strain vs. indentation depth for the best results from the SLP - and SQP optimisation algorithms, for the diagonal cylindrical indenter

In figure 6.12 the sorted objective function for each of the 10 optimisation runs, for both algorithms, are depicted. It can be observed that the SLP algorithm obtained the same objective function and thus the same material model, regardless of the starting point. The SQP algorithm within this indentation test, obtained a better objective function to the SLP algorithm for each optimisation

run. The eighth optimisation run, represents the extra material model obtained by the SQP algorithm within table 6.15.

Between the cylindrical indenters, an indentation test with a diagonal cylindrical indenter, obtains the best material model for the smallest objective function.

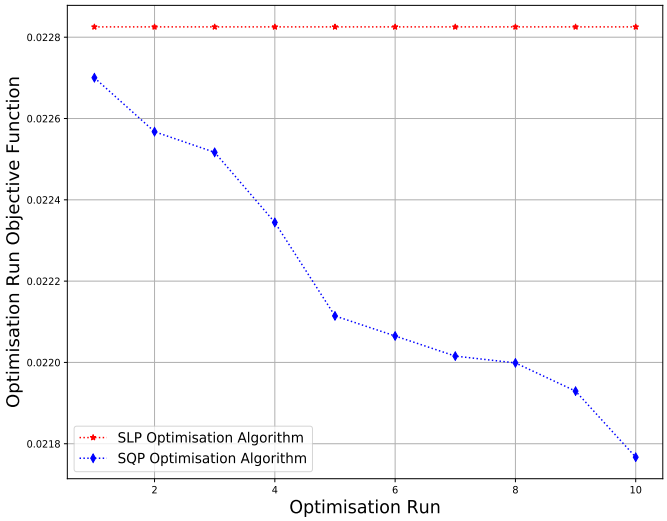

Figure 6.12: Objective functions for each of the 10 design points, obtained by both the SLP - and SQP algorithms, for the diagonal cylindrical indenter

6.5 One Spherical Indenter

Within table 6.16 the error results for the material model obtained by the SLP algorithm can be observed. All three displacements obtained acceptable results with a nearly perfect fit within each direction of more than 99%. An overall objective function of 0.0569 was obtained for this material model.

Table 6.16: Errors obtained for the best design point, for a 3 mm indentation with one spherical indenter, using the SLP optimisation algorithm

	R^2	RMS	SEOE
X-displacement	0.9948	0.0198	0.0177
Y-displacement	0.9970	0.0130	0.0303
Z-displacement	0.9990	0.0089	0.0118
Min. principal strain	0.8855	0.0117	0.0163
Max. principal strain	0.7228	0.0211	0.1409
Engineering stress	0.9880	0.0006	0.0449

In table 6.17 it can be observed that the material model obtained by the SQP algorithm obtained nearly perfect fits for all three displacement directions of more than 99% each. An overall objective function of 0.0528 was obtained for this material model, which is smaller to the one obtained by the SLP algorithm. This resulted in the expected observation, that the material model from the SQP algorithm obtained better displacement results. The SQP's material model obtained a smaller objective function compared to the original material model from chapter 5, but the material model did not obtain better displacement results within table 6.17 compared to table 5.5.

Table 6.17: Errors obtained for the results with the smallest objective function, for a 3 mm indentation with one spherical indenter, using the SQP optimisation algorithm

	R^2	RMS	SEOE
X-displacement	0.9957	0.0181	0.0163
Y-displacement	0.9979	0.0126	0.0295
Z-displacement	0.9994	0.0080	0.0106
Min. principal strain	0.8904	0.0119	0.0161
Max. principal strain	0.6903	0.0210	0.1400
Engineering stress	0.9995	0.0001	0.0056

The SQP algorithm obtained another material model which obtained better results within the Y - and Z - displacements, as can be observed in table 6.18. This is unexpected since the overall objective function obtained for this material model is 0.0533, which is larger than the first material model obtained from the SQP algorithm. This objective function, obtained by the extra material model from the SQP algorithm, is smaller than the original material model's within chapter 5, but it is only the Y - displacement's results within table 6.18, which improved from the results in table 5.5. The three material models with their objective functions are summarised within table 6.19.

Table 6.18: Errors obtained for the results with the best curve fitting results, for a 3 mm indentation with one spherical indenter, using the SQP optimisation algorithm

	R^2	RMS	SEOE
X-displacement	0.9946	0.0194	0.0174
Y-displacement	0.9988	0.0095	0.0222
Z-displacement	0.9997	0.0053	0.0070
Min. principal strain	0.8537	0.0122	0.0161
Max. principal strain	0.7426	0.0214	0.1426
Engineering stress	0.9998	0.0001	0.0046

Table 6.19: Optimised Mooney-Rivlin parameter, obtained from the SLP - and SQP optimisation algorithms respectively, for the one spherical indenter

Optimisation algorithm	C_{10} [MPa]	C_{01} [MPa]	C_{20} [MPa]	Objective function
SLP	0.208454	0.078040	0.046001	0.0569
SQP - Best objective function	0.308723	0.080755	0.051686	0.0528
SQP - Best fitted results	0.285277	0.084034	0.053420	0.0533

The engineering stress vs. stretch curves for the three material models in table 6.19 are shown in figure 6.13. The material model from the SLP algorithm obtained the largest objective function and it is thus expected to find this model with the least accurate fitted curve within figure 6.13. This material model successfully fitted the "Experimental" model's curve within the standard error, with an approximate 0.7 - 2.0 stretch range. An interesting observation can be made between the two material models obtained from the SQP algorithm. Firstly, from table 6.17 and table 6.18, the extra material model obtained a better fit to the material model with the smallest objective function, but with only 0.03%. This explains secondly, the perfect fit between these two material models and the near perfect fit between each material model from the SQP algorithm and the "Experimental" model, respectively. As can be observed in figure 6.13, both the SQP material models fitted the "Experimental" model within the standard error for the entire stretch range. Lastly, the difference in the material model parameters does not seem to have a big effect. The study in appendix D concluded that each material parameter causes quite a change within the engineering stress, but the results presented within figure 6.13, prove that multiple sets of parameters exist to fit the "Experimental" model.

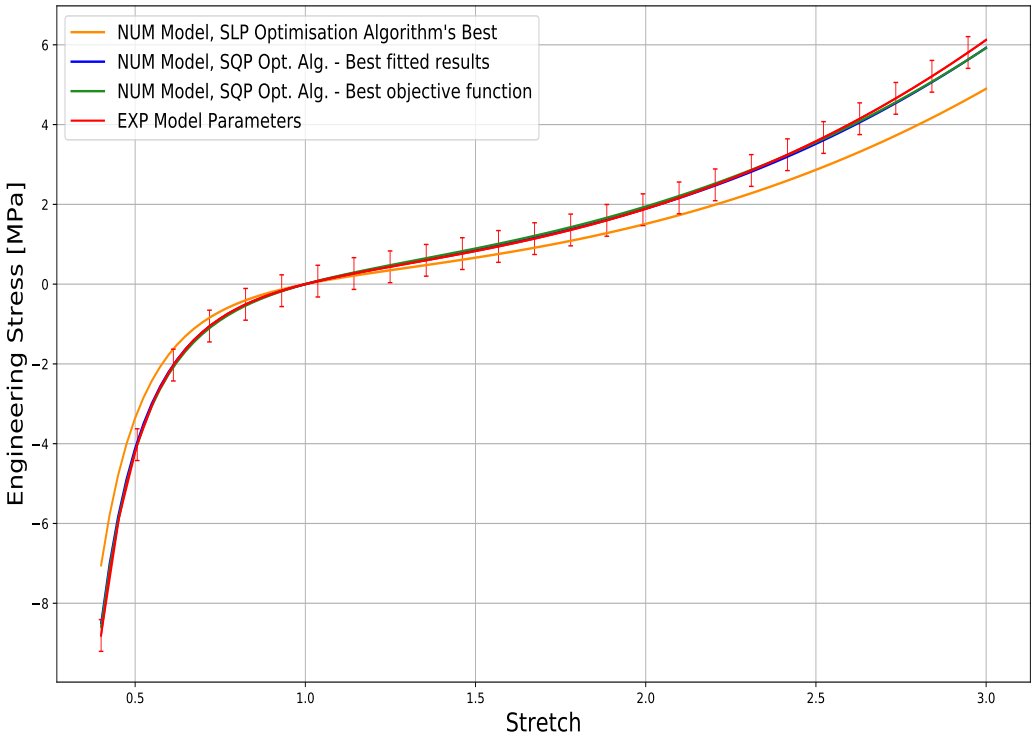

Figure 6.13: Engineering stress vs. stretch for the best results obtained from the SQP - and SLP optimisation algorithms, for the one spherical indenter

Within figure 6.14 all three material models in table 6.19, underestimated both the principal strains. In chapter 5 this was established to be expected. Within the minimum principal strain, the material model with the smallest objective function from the SQP algorithm, obtained the best R^2 fit of 89.04%, as expected. Next is the material model from the SLP algorithm with an R^2 fit of 88.55%, which is not expected since this model obtained the largest objective function. The maximum principal strain results obtained the best fit from the extra material model in the SQP algorithm, followed by the material model from the SLP algorithm. This also caused unexpected observations since both of these material models obtained the largest objective functions from the three material models obtained. A last observation which can be made, is that all three material models obtained a better fit for the minimum principal strain compared to the original material model shown in table 5.5, which is expected from the SQP's material models, but not the SLP's material model. With regards to the maximum principal strain, the material model which obtained the smallest objective function within the SQP algorithm, did not obtain a better fit for the "Experimental" model, compared to the original material model with a larger objective function. All three models might have obtained respectable R^2 values for the minimum principal strain, but all three models failed in obtaining accurate results.

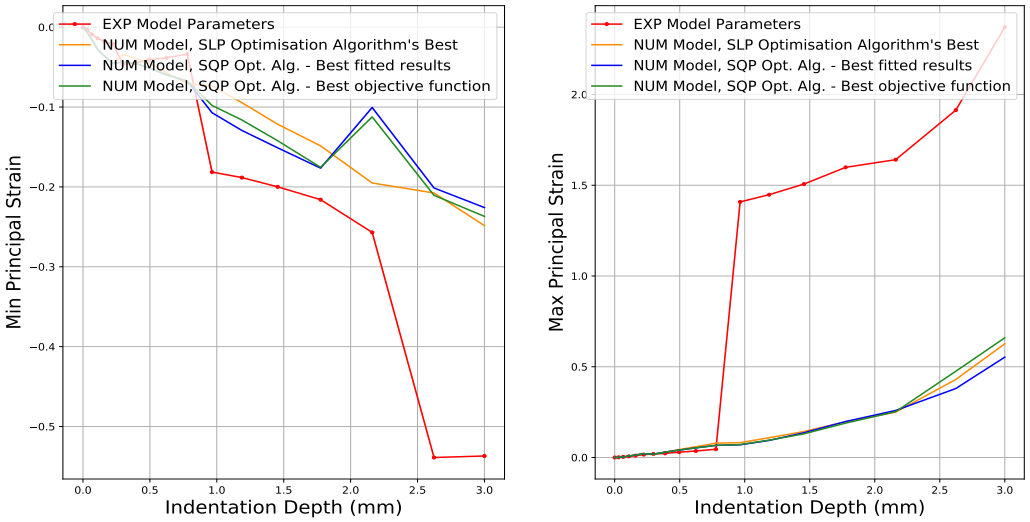

(a) Min. principal strain vs. indentation depth

(b) Max. principal strain vs. indentation depth

Figure 6.14: Min.- and Max. principal strain vs. indentation depth for the best results from the SLP - and SQP optimisation algorithms, for the one spherical indenter

Figure 6.15 depicts the sorted objective functions for each of the 10 optimisation runs for both the SLP - and SQP algorithms. It is observed that the SLP algorithm obtained the same objective function for all 10 optimisation runs, hence the same material model. The material model obtained by the SLP algorithm, is the same material model obtained for all the indentation tests so far. Each of the

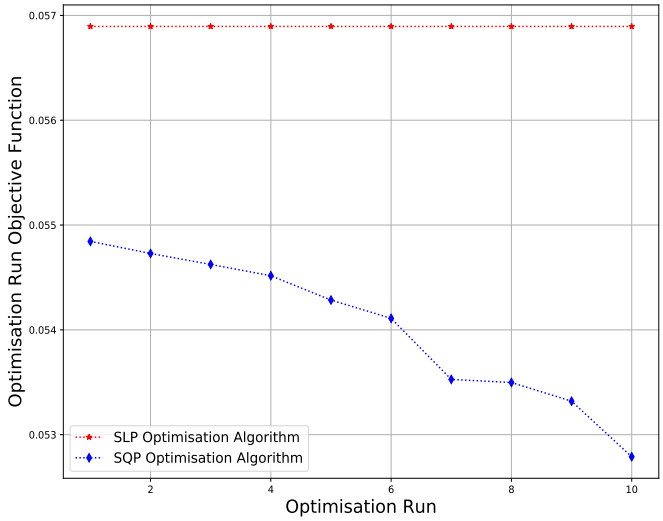

Figure 6.15: Objective functions for each of the 10 design points, obtained by both the SLP - and SQP algorithms, for the one spherical indenter

material models obtained within the SQP algorithm, obtained a larger objective function to the SLP algorithm. The ninth optimisation run represents the extra material model obtained for the SQP algorithm within table 6.19.

6.6 Two Spherical Indenters

Within table 6.20 the material model obtained by the SLP algorithm, obtained a nearly perfect fit of more than 99% for each displacement. An overall objective function of 0.0680 was obtained. This material model obtained a smaller objective function from the original material model within chapter 5, but the displacement results in table 6.20 have not improved from the original model's results in table 5.6.

Table 6.20: Errors obtained for the best design point, for a 3 mm indentation with two spherical indenters, using the SLP optimisation algorithm

	R^2	RMS	SEOE
X-displacement	0.9987	0.0145	0.0182
Y-displacement	0.9971	0.0144	0.0316
Z-displacement	0.9994	0.0093	0.0118
Min. principal strain	0.8995	0.0089	0.0107
Max. principal strain	0.5565	0.0108	0.0197
Engineering stress	0.9880	0.0006	0.0449

The SQP algorithm obtained a material model with an overall objective function of 0.0673, which is an improvement from the objective function obtained by the original material model in chapter 5 and from the material model obtained by the SLP algorithm. The displacement results for this material model in table 6.21, obtained nearly perfect R^2 fits for each direction of more than 99%. The X - displacement obtained better results to the original model in table 5.5 and the material model obtained by the SLP algorithm. The Z displacement obtained a better fit to the material model from the SLP algorithm. The improved results for this material model, were expected due to the smaller objective function.

Table 6.21: Errors obtained for the results with the smallest objective function, for a 3 mm indentation with two spherical indenters, using the SQP optimisation algorithm

	R^2	RMS	SEOE
X-displacement	0.9991	0.0122	0.0153
Y-displacement	0.9970	0.0139	0.0306
Z-displacement	0.9997	0.0081	0.0102
Min. principal strain	0.8869	0.0087	0.0103
Max. principal strain	0.7051	0.0101	0.0188
Engineering stress	0.9993	0.0001	0.0074

The material models obtained by both the SLP - and SQP algorithms respectively, can be found in table 6.23. It can be observed that another material model was obtained by the SQP algorithm, which produced nearly perfect displacement fits of more than 99%, shown in table 6.22. This extra material model obtained an overall objective function of 0.0677, which is smaller than the objective function obtained by the SLP algorithm.

Table 6.22: Errors obtained for the results with the best curve fitting results, for a 3 mm indentation with two spherical indenters, using the SQP optimisation algorithm

	R^2	RMS	SEOE
X-displacement	0.9989	0.0152	0.0191
Y-displacement	0.9969	0.0147	0.0324
Z-displacement	0.9997	0.0066	0.0083
Min. principal strain	0.7959	0.0102	0.0118
Max. principal strain	0.6386	0.0107	0.0204
Engineering stress	0.9997	0.0001	0.0035

Table 6.23: Optimised Mooney-Rivlin parameter, obtained from the SLP - and SQP optimisation algorithms respectively, for the two spherical indenters

Optimisation algorithm	C_{10} [MPa]	C_{01} [MPa]	C_{20} [MPa]	Objective function
SLP	0.208454	0.078040	0.046001	0.0680
SQP - Best objective function	0.271716	0.101385	0.051918	0.0673
SQP - Best fitted results	0.267954	0.082347	0.058411	0.0677

The engineering stress vs. stretch curves can be found in figure 6.16 for the material models in table 6.23. The material model obtained by the SLP algorithm, fitted the "Experimental" model within the standard error for approximately a 0.7 - 2.0 stretch range. This material model obtained the largest objective function and it was therefore expected not to obtain a perfect fit. Interesting results were obtained for the SQP algorithm's material models. The extra material model obtained by the SQP algorithm, obtained the best fit within the engineering stress vs. stretch curve to the material model with the smallest objective function, which was unexpected. Both material models from the SQP algorithm fitted the "Experimental" model for the entire stretch range within the standard error.

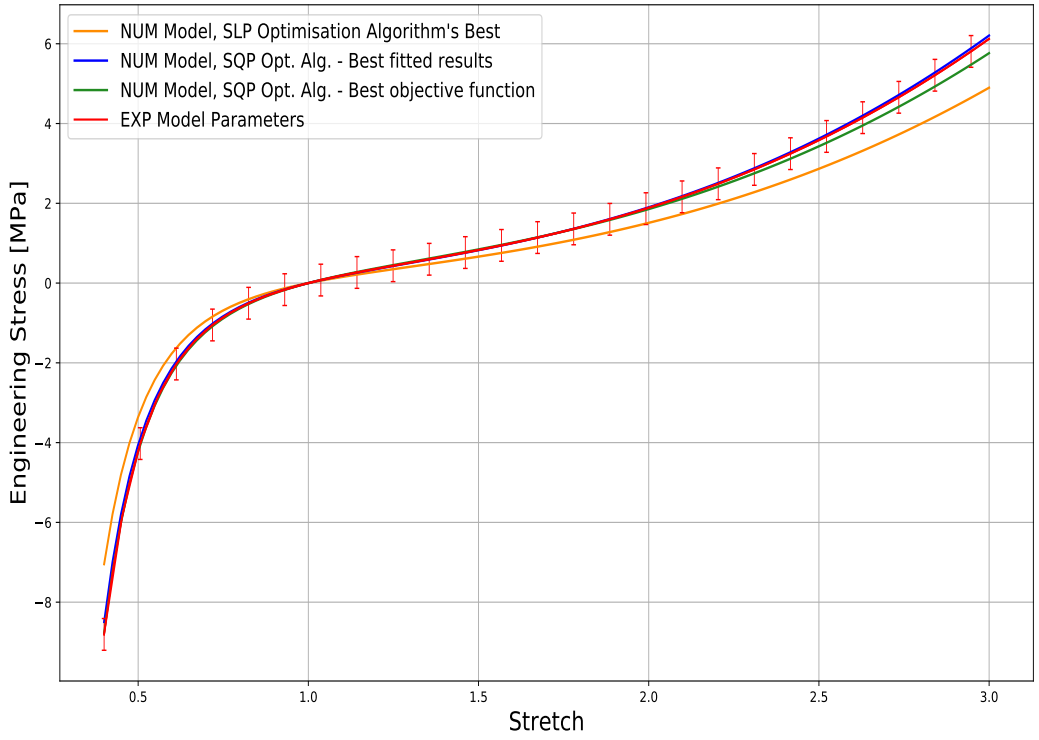

Figure 6.16: Engineering stress vs. stretch for the best results obtained from the SQP - and SLP optimisation algorithms, for the two spherical indenters

Within figure 6.17, the material models obtained by both the SLP - and SQP algorithms, underestimated both the principal strains. Other than the error obtained by the contact tolerance within the "Numerical" model, the material model obtained by the SLP algorithm, obtained the best R^2 fit of 89.95%, but it possessed the largest objective function. It is expected that the material model with the best objective function obtained by the SQP algorithm obtained the best fitted results within the maximum principal strain results. Overall, the extra material model

obtained by the SQP algorithm, only obtained the best fit within the engineering stress vs. stretch curve and obtained further results in line with what was expected from the objective function.

Within figure 6.18, the sorted objective function for each of the 10 optimisation runs can be observed. It is clear that the SLP algorithm obtained the

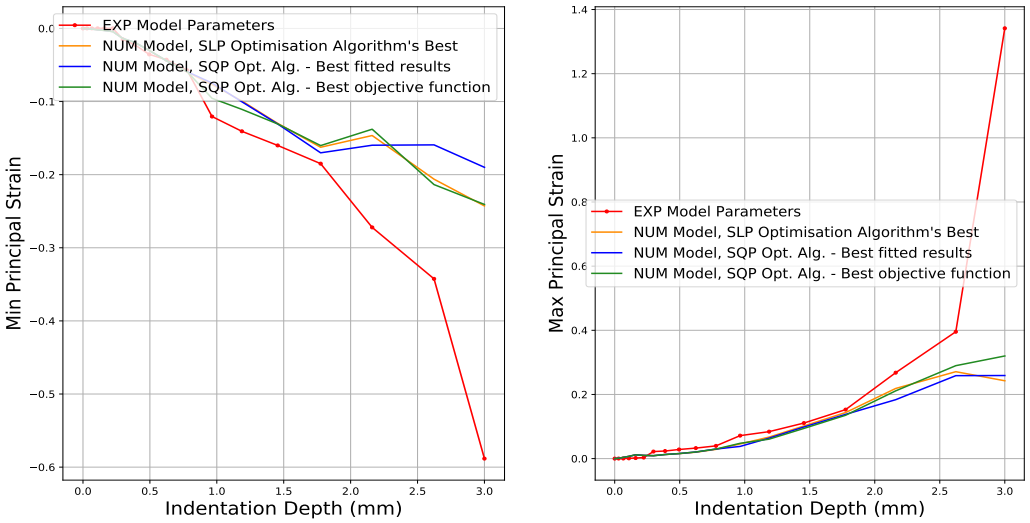

(a) Min. principal strain vs. indentation depth

(b) Max. principal strain vs. indentation depth

Figure 6.17: Min.- and Max. principal strain vs. indentation depth for the best results from the SLP - and SQP optimisation algorithms, for the two spherical indenters

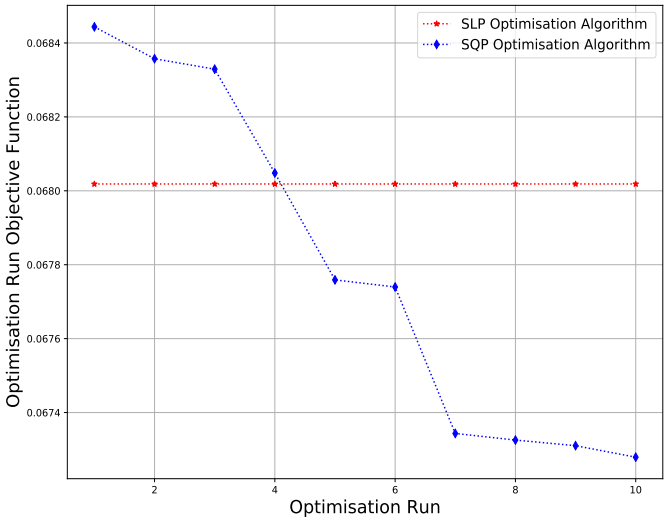

Figure 6.18: Objective functions for each of the 10 design points, obtained by both the SLP - and SQP algorithms, for the two spherical indenters

same objection function for all of the optimisation runs, hence the same material model. The SQP algorithm obtained a new material model with every optimisation run, hence the different objective functions. The sixth optimisation run represents the objective function obtained for the extra material model obtained by the SQP algorithm.

6.7 Summary

To summarise the six indentation test results above, it can be concluded that five of the six indentation tests successfully characterised the silicone rubber through inverse finite elements analysis. Acceptable results were obtained within the three displacements directions for these five indentation tests. The parallel cylindrical indenter failed to produce acceptable results within the Y - displacement, hence failing to fit the "Experimental" model accurately. The SLP optimisation algorithm obtained the same material model in every single optimisation run and test. This material model is equivalent to the lower bounds for each of the material variables. The SQP algorithm obtained two material models in each indentation test, except for the parallel cylindrical indenter. The one material model obtained the smallest objective function, while the other material model obtained the best fit for the engineering stress vs. stretch curve. Unexpected results were obtained for the engineering stress vs. stretch curves and the principal strain curves. A summarised conclusion can be made that the material model with the smallest objective function does not necessarily obtain the best engineering stress results or principal strain results. Finally, the diagonal cylindrical indenter obtained the best results, which will be discussed in more detail within chapter 7.

Chapter 7

Discussion and Conclusion

Six different indentation tests were conducted using two FE models and an inverse finite element approach to characterise a soft silicone rubber using micro-indentation. The Mooney-Rivlin three parameter model was used to describe each of the FE model's material behaviour. Inverse FE analysis was used to obtain a set of material parameters for each indentation test's "Numerical" model, to fit to the "Experimental" model's results. Two optimisation procedures were used, namely the SLP and SQP constraint gradient based optimisation algorithms. The Mooney-Rivlin three parameter constitutive equation for a uni-axial compression case, was used to predict the engineering stress vs. stretch curve for the material models obtained from the optimisation algorithms. From the test results, the minimum and maximum principal strains were obtained against the indentation depth, to determine the multi-axial strain response for each indentation test. Taking all the tests results into account, it was determined that using a diagonal cylindrical indenter will characterise a soft material the best.

7.1 Discussion

Chapter 6 presented the results obtained for each indentation test, along with the interesting and unexpected results. A general discussion can be made from the observations obtained from the results.

Firstly, according to the numerical pipeline and the optimisation procedures, the overall objective function was calculated using only the displacement results. Five of the six indentation tests successfully obtained acceptable displacement correlations within each direction. The combined displacement RMS value was used for the objective function; it is therefore reasonable to believe that the indentation test which obtained the best objective function, is the best test to use for characterisation. From the results obtained by the different indentation tests, it was seen that a less complex displacement field obtained a smaller objective function, since the field is easier to fit than a more complex field. Therefore the complexity of the displacement field need to be considered. However, the whole

inverse FE approach was built around the objective function and any other contributing factor which was not accounted for, cannot have a larger contributing factor towards the final decision.

One of the main goals for this thesis was to obtain an improved method for characterising soft materials to improve the engineering stress vs. stretch curve within both the compression and tension region. Each of the indentation tests obtained a material model through the SQP algorithm which obtained a nearly perfect fit for the engineering stress vs. stretch curve for the entire stretch range. Unfortunately these material models did not obtain the smallest objective functions. This is a new observation which can lead to new research within the future. It was due to this observation that the material models and the results were further investigated. However, the parameters obtained by these material models, prove that they are not unique for the Mooney-Rivlin model and that many combinations of the parameters will result in the same accurate fit for the displacement field. Therefore the parameters of the material model does not influence the deciding factor.

The stretch is directly correlated to the principal strains; it was therefore decided to investigate the minimum and maximum principal strains obtained for the indentation depth. The same conclusion can be drawn that the material model which obtained the smallest objective function, cannot guarantee the best strain results. To be fair, the FE models introduced an error within the data obtained for the principal strain values and the results are not an accurate representation, but it does form a good idea of what can be expected. Disregarding the error, the same FE model was used to obtain the results and the material model obtained by the SQP algorithm with the largest objective function, still obtained better results. The diagonal indenter model obtained the best fit for the original material model, within the principal strain results. Where the spherical indentation tests obtained principal strains with large errors, the diagonal indenter did not have this big of a problem and can therefore be concluded to be a more stable test. By comparing the material model obtained by the SQP algorithm for the smallest objective function, the minimum principal strain curve did not fit the "Experimental" model's curve perfectly, but it had the same shape as the original "Numerical" model's result within figure 5.9. This means this test possesses the potential to obtain its best possible result. It was therefore decided that the diagonal cylindrical indenter was chosen as the best indentation test. Between the three material models, the material model with the larger objective function obtained by the SQP algorithm, is the best material model obtained.

The one perpendicular cylindrical indenter obtained better theoretical correlation values but the strain change at an indentation depth of 3 mm, was still larger between the two FE models. This indentation test will definitely be the second choice. The spherical indenters did not obtain desirable results to be considered even further. The parallel and two perpendicular cylindrical indentation tests were considered difficult to implement within practice and with real time experimental tests, due to the precision required within the placement of

the indenters to conduct the indentation test.

Some final remarks can be made towards the optimisation algorithms. It was not an objective to find the best optimisation method, but it was clear that the SQP algorithm performed the best. A results that can count in favour of the SLP algorithm, is the fact that between the 120 different optimisation runs across the very different indentation tests, the same material model was obtained each time. If the material model obtained by the algorithm predicted better results, it would have been the perfect test procedure since one optimum guaranteed material model would have been obtained and therefore the silicone rubber would have been perfectly characterised. Another interesting observation, the objective functions obtained in the optimisation procedure, was most of the time smaller than the objective functions obtained by the original models with the desired material model. This can point to the fact that the optimiser uses the material model to also compensate for the difference in mesh convergence between the two models. This is an interesting observation which can be investigated in future work.

7.2 Conclusion

In conclusion, micro-indentation is a promising method to characterise soft material and it is proven that with the correct indenter, a soft material can be characterised accurately. Using a cylindrical indenter, applying a uni-axial load in a diagonal fashion across the test sample, will obtain the best Mooney-Rivlin material model using a SQP optimisation algorithm within an inverse FE approach. The final conclusion from the observations within the results suggested, that a material model either matched the displacement field nearly perfect, or the engineering stress vs. stretch curve nearly perfect, but both cannot be matched perfectly simultaneously.

7.3 Future Work

This thesis successfully proved that indentation can be used to characterise soft material within a theoretical environment, but there is always room for improvements. It was assumed that optimising for the displacement results would obtain an equivalent accurateness within the engineering stress and strain results. The reason behind this assumption is related to the fact that stress and strain are derived properties from the displacement field and the displacements are directly measured in DIC and calculated by FE models. The results within this thesis, showed that this was evidently not true. It is advised within future work to investigate to optimise for the strain response instead of for the displacement results, or even better, incorporating both results in a single objective function to account for both responses.

The remeshing feature within Marc has a lot of potential, but need some improvements in implementing the procedure with its full potential. It is advised to test for different settings. Unfortunately the node tracking drawback limited the results obtained within this thesis, as well as affected the accuracy of the results due to the method used for tracking the nodes. Using membrane elements, which are glued to the sample surface, worked in tracking the displacement results, but was not the best method to obtain stress or strain results. Contact within the FE model, contributes and effects the stress and strain results greatly. The slightest changes in the settings cause the stress results to change from 2 MPa to 10 MPa, which is not a desirable effect. It is proposed to find a method in obtaining the stress and strain results directly from the sample nodes. Another quick solution is to model the membrane elements with a smaller element size. From the experience obtained within this thesis, perfectly square elements work the best. The size of the membrane elements used within this thesis, were the smallest element size to obtain perfect squares in the mesh relative to the sample size.

Only one hyper-elastic material model was considered and more might be beneficial in validating the indentation methods. More complex indenters can be tested as well such as a cross, to account for more complex material properties. This method was able to characterise soft silicone and can possibly characterise soft biological tissue. If this method should be applied to soft biological tissue, a more complex displacement field might be needed to account for the complex anisotropic material properties. The repeatability of this study can be tested by applying this approach to more than one type of silicone and can be taken as far as biological tissue.

The next step for this research it to validate the results obtained within this thesis with real time tests.

Appendices

Appendix A

Mesh Refinement Study: Remesh vs. No Remesh

Remeshing offers benefits in reducing the exponential increase in run time during an FE analysis and to improve the drawbacks from encountering distortion, by replacing the mesh within the FE analysis with an improved mesh. Along with the benefits, some drawbacks like the lack of node tracking for some elements are not available. A particle tracking method can be used within the remesh feature for tet4 elements, but it is not supported for tet10 elements. This study first investigated with tet4 elements if remeshing is worth using within this thesis.

This thesis investigated six different indentation tests. In order to determine how well remeshing performs compared to no remeshing, a complex deformation field is required. This section investigated the difference in results obtained for the FE model with the largest complexity in deformation in the XY - plane. The parallel indentation test was used for this study. Figure A.1a is the indentation test FE model used for this study. In figure A.1b the green dot is the node location used for data capturing during this study. The indenter displaced 2 mm in the negative Y - direction.

With the tet4 elements, the particle tracking feature within the remesh feature can be used. The node is chosen within the first increment of the FE analysis and the particle tracking feature predicts its movement along the FE analysis. Within the last increment the same node id can be used to capture the data at every increment. Only the data in the last increment was used for comparison.

Table A.1 gives the wall time and Y - displacement results obtained for both remesh and no remesh models, at finer mesh sizes. With regard to the Y - displacement captured at the last increment, shown in figure A.2, the remesh model produced acceptable results at a coarse mesh, where the no remesh model only produced acceptable results at a finer mesh. From figure A.3 and a closer look at table A.1 in the wall time section, it can be seen that initially the remesh model takes longer to converge at a coarse mesh, but with a finer mesh it is faster.

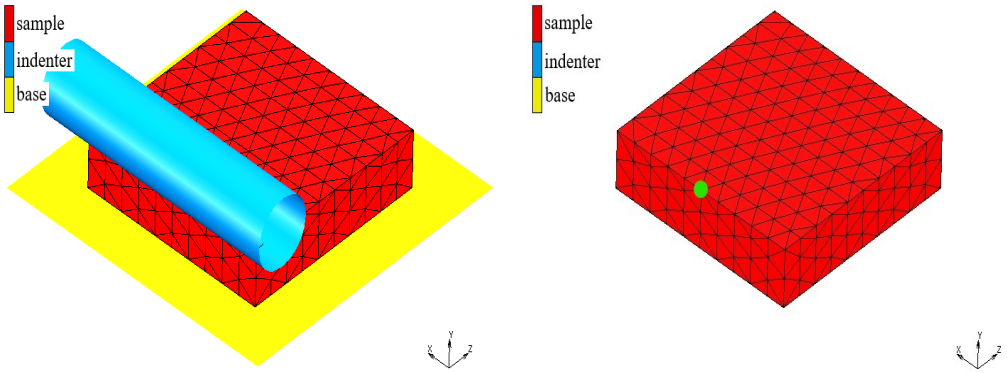

(a) FE model (b) Node location

Figure A.1: FE model of the indentation test used during the remesh vs. no remesh study, with indicated node location for data capturing

Table A.1: Tet4 Remesh vs. No Remesh Results

Y-Displacement [mm]			Wall Time [s]	
Element Edge Length	Remesh	No Remesh	Remesh	No Remesh
0.35	1.8471	1.9155	5338.67	5720.01
0.53	1.8220	1.9538	916.37	936.15
0.7	1.8037	1.9496	295.90	350.94
1.1	1.7452	1.9684	93.98	70.94
1.5	1.7878	1.9567	67.19	18.43
3.0	1.7866	1.4673	53.94	4.11

It can therefore be concluded that the remeshing feature will produce more accurate results at a coarser mesh with a better wall time, where the no remesh model will need a finer mesh and more time to produce equally acceptable results. Even though the remesh feature did not improve the wall time by a significant amount, the fact that it took longer in the initial coarser mesh and quicker in the finer mesh shows that it is able to resolve the distortion better than the no remesh model. A closer observation at the specific numbers within table A.1, the remesh model saves more or less six minutes within the wall time, meaning it will improve the computational cost within the optimisation procedure where every iteration needs to perform multiple FE analysis. From this study it is also decided that a mesh size of 0.9 mm for the "Experimental" model can be used and a mesh size of 1.0 mm for the "Numerical" model.

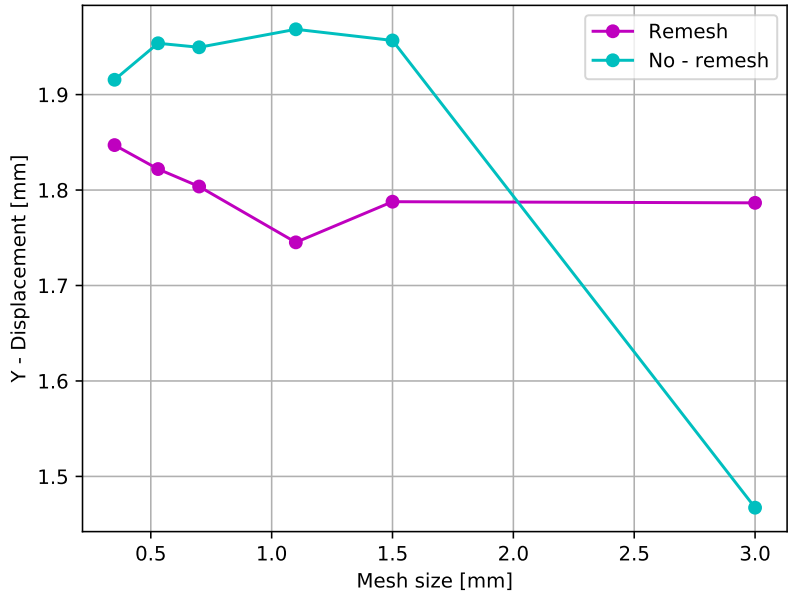

Figure A.2: Node's Y - displacement vs. mesh size for remesh vs. no remesh study

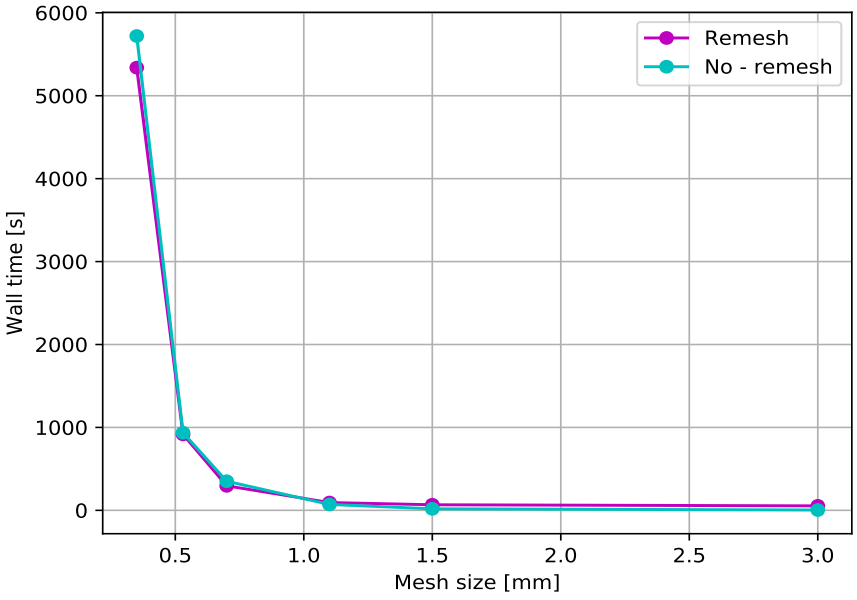

Figure A.3: Wall time vs. mesh size for remesh vs. no remesh study

Appendix B

Mesh Refinement Study: Tet4 vs. Tet10 Elements

In Appendix A is was determined that the remeshing feature within Marc will be used for the FE models. One of the drawbacks is to track the nodes within the tet10 elements. It is already established that the nodes within the tet4 elements can be tracked with the particle tracking feature in Marc. The tet10 elements are not supported within this feature, therefore this study will establish if tet10 elements are necessary and if tet4 elements will be sufficient.

Figure B.1 is the FE model used for both the tet4 and tet10 FE analysis. The parallel indentation test was used, since it possesses the most complex defor-

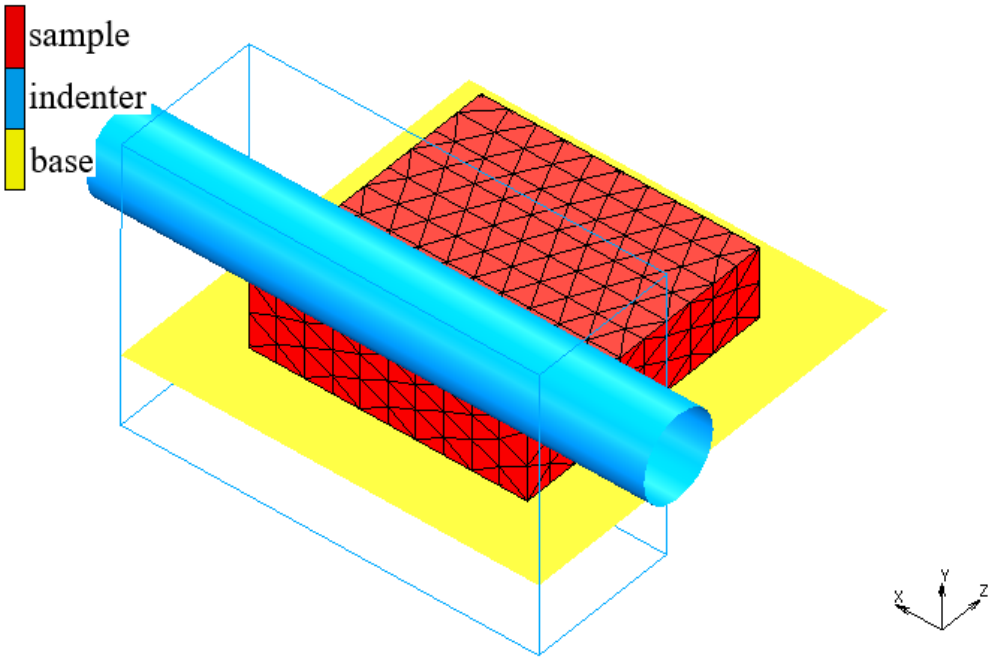

Figure B.1: FE model for study between tet4 and tet10 elements

mation field. The blue square outline around the indenter indicates the area that needs to undergo remeshing within the silicone sample (the meshed red square). Both the tet4 and tet10 FE models were remeshed to a minimum mesh size of 0.9 mm. Four indentation depths were tested to compare how well both element types perform under an increasingly complex deformation.

Both models were tested with indentation depths of 1 mm, 2 mm, 3 mm and 4 mm. From the graphs in figure B.2 the tet10 elements performed very consistently overall, but the wall time was almost double from the tet4 elements. Even though the tet4 elements had a better computation time, the tet10 elements needed only four remeshes and zero cutbacks up until indentation depth of 3 mm, where the tet4 elements were stuck with 17 remeshes. At an indentation depth of 4 mm the tet10 FE model converged after eight remeshes and two cutbacks, where the tet4 FE model was not able to converge after the 17 remeshes and 24 cutbacks. This means that the tet10 elements are more stable than the tet4 elements and are more prone to finding a solution at a more complex deformation field.

Since the nodes cannot be tracked within the tet10 elements, only the last

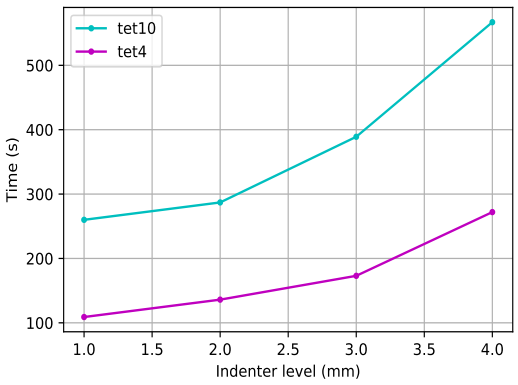

(a) Wall time vs. indenter depth

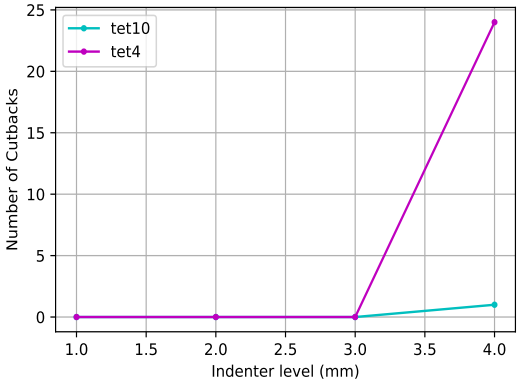

(b) Number of cutbacks vs. indenter depth

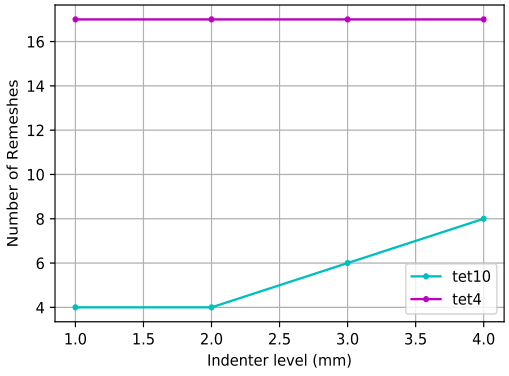

(c) Number of remeshes vs. indenter depth

Figure B.2: Results for Wall time-, Number of cutbacks- and Number of remeshes vs. indenter depth for the tet4 vs. tet10 elements study

increment's results were used for the full field displacements in figures B.3 and figures B.4. The displacement results can only be obtained for each node per increment, from its starting point and how much it displaced from there on. Therefore with the remeshing feature the node might have been created in increment five and remeshing can occur before increment six, therefore the displacement is only valid from where the node started and displaced in increment five. The total displacement can be obtained for the nodes present at the last increment, but not during every increment. The nodal displacement data used for this study was thus obtained and chosen by using the data from the last increment. The nodes of interest are in the XY-plane at $Z = 0$. By using Eq. B.1, the approximate location of the node's original Z-coordinate can be obtained. Since this is an approximate solution, the Z-coordinate will not be exactly equal to zero. It was therefore decided to use every node which had an original Z-coordinate value less than 0.005. This method was used for both the tet4 and tet10 FE model results, even though the tet4 elements can be properly tracked. It ensured a proper baseline for the results. This method is not the best or most accurate way to obtain the nodal displacements and should therefore not be used for formal data capturing, but it is an effective and reasonable method for the aim in this study.

$$C_{Z_0} = \left(C_{Z_m} + D_{Z_m}\right) - Dt_{Z_m} \approx 0 \tag{B.1}$$

where C_{Z_0} is the node's original Z-coordinate, C_{Z_m} the node's coordinate at the last increment, D_{Z_m} the node's Z-displacement from coordinate C_{Z_m}. Dt_{Z_m} is the node's approximate total displacement from its original Z-coordinate, when it was created during the FE analysis.

Within figure B.3 the tet4 model's nodal displacements were interpolated towards the tet10 model's nodal displacements. In figure B.4 the tet10 model's nodal displacements were interpolated towards the tet4 model's nodal displacements. Both interpolation results were done for an indentation depth of 3 mm. The only reason why the results in figure B.3 obtained better error values than those of figure B.4, is because the tet10 elements have more nodal points to improve the quality of the RBF interpolation function. But this also means that at a coarser mesh, the tet10 elements will be able to interpolate the results with a better quality due to the number of nodal points available.

From the results obtained, it is clear that the tet10 elements are more stable with complex deformation fields and the ability to fit data is also of a better quality.

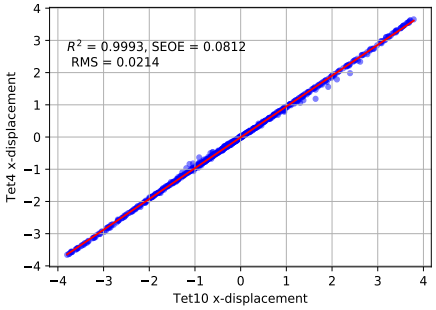

(a) X-displacement

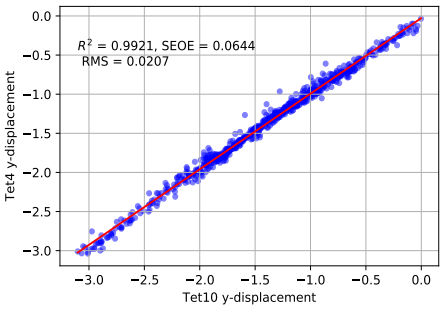

(b) Y-displacement

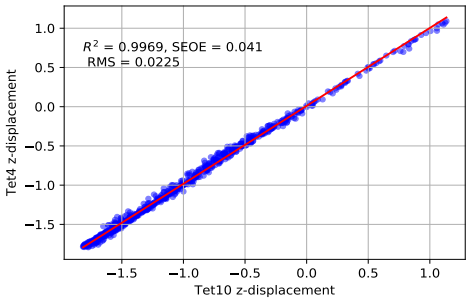

(c) Z-displacement

Figure B.3: Displacement errors for the tet4 nodal displacements interpolated to the tet10 nodal displacements, with an indenter depth of 3 mm

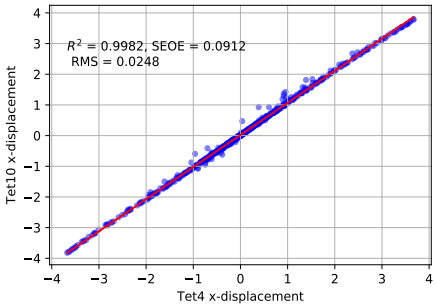

(a) X-displacement

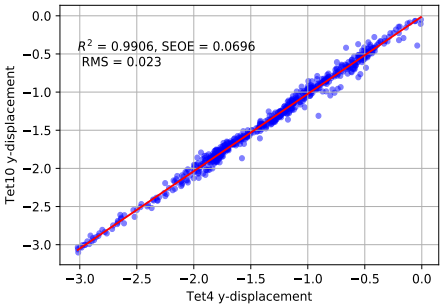

(b) Y-displacement

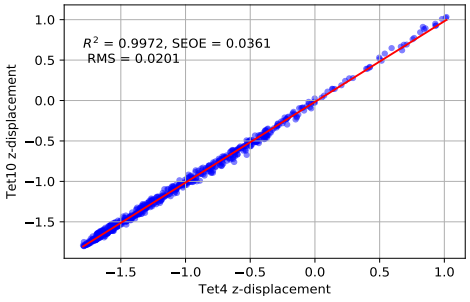

(c) Z-displacement

Figure B.4: Displacement errors for the tet10 nodal displacements interpolated to the tet4 nodal displacements, with an indenter depth of 3 mm

Appendix C

Mesh Refinement Study: Membrane Elements

It has been established that the remeshing feature with tet10 type elements will be used for all the FE models within Marc. The particle tracking feature does not support tet10 elements and a new method is needed to track the nodes for data capturing. Membrane elements of thickness 0.001 mm will be glued on the desired surface within the XY-plane at $Z = 0$, of the silicone sample. The nodes within this thin membrane layer should possess approximately the same nodal values as the nodes on the surface of the silicone sample. What still needs to be established, is the mesh size of these membrane elements. This study examines which of the three mesh sizes (1 mm, 0.5 mm or 0.25 mm) for the membrane elements, obtains the best nodal results compared to the nodal results on the silicone sample's surface.

Within this thesis the "Experimental" models will be remeshed to a minimum element edge length of 0.9 mm and the "Numerical" models to a minimum element edge length of 1 mm. This study will remesh the FE models to a minimum edge length of 1 mm to ensure that the coarser "Numerical" models will obtain acceptable results. The one perpendicular cylindrical indenter test will be used for this study. Figure C.1a is the tet10 FE model which will be used to validate which of the membrane mesh sizes in figures C.1b-C.1d will obtain the best results for data capturing. The remesh feature is not applied to the membrane elements and therefore the nodes within these elements will be used for data capturing within the models in figures C.1b-C.1d. The data for the tet10 model in figure C.1a was obtained using the same method as in Appendix B. Therefore the displacement field in the last increment is the only data used for comparison within this study. The RBF interpolation will be used to predict the displacements from the models in figures C.1b-C.1d at the nodal coordinates from the model in figure C.1a.

Between the results obtained from figures C.2-C.4, all three mesh sizes produced acceptable results. The 0.25 mm mesh size performed the best and the 1 mm the worst as expected. It was decided to use the 0.5 mm mesh size for

the membrane elements in the "Numerical" models. The "Experimental" models are remeshed to a minimum mesh size of 0.9 mm, which is a finer mesh than used in this study.It was therefore decided to use the 0.25 mm mesh size for the membrane elements for the "Experimental" models.

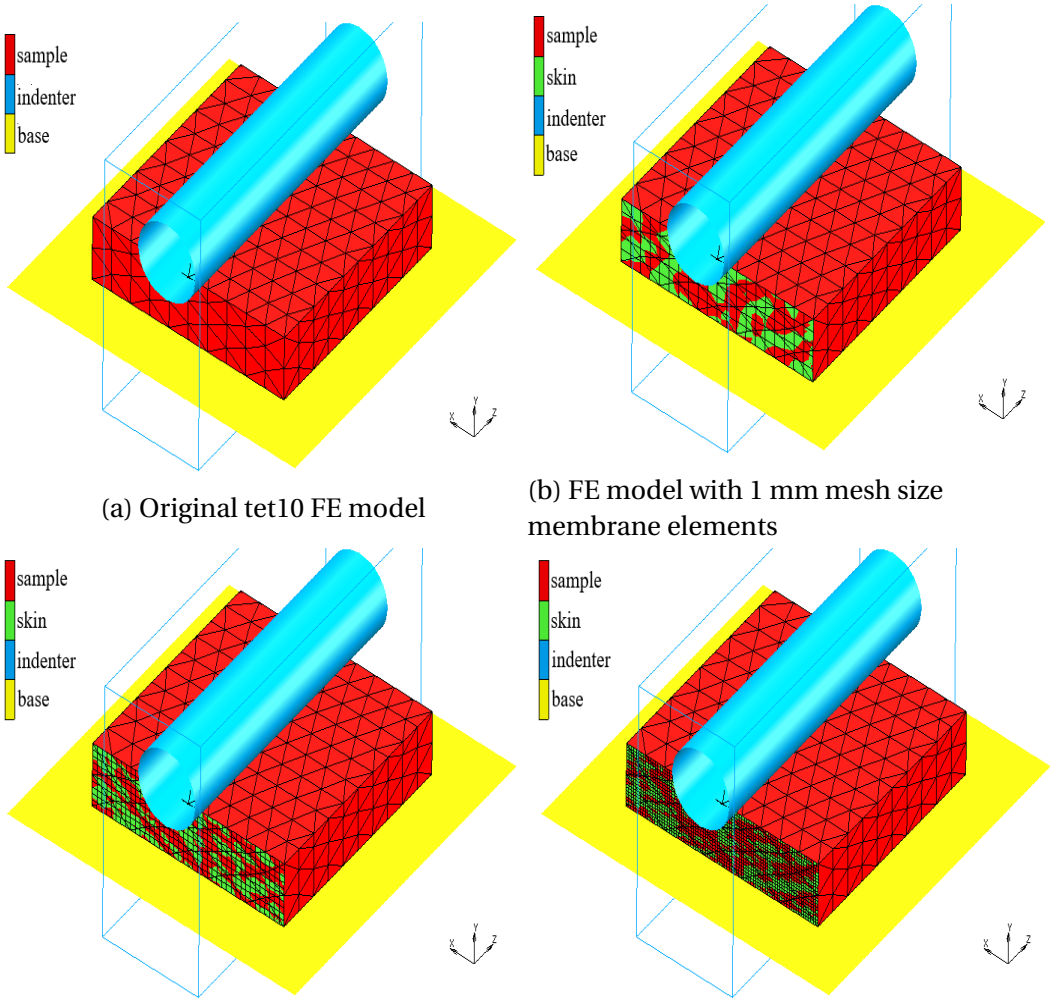

(a) Original tet10 FE model

(b) FE model with 1 mm mesh size membrane elements

(c) FE model with 0.5 mm mesh size membrane elements

(d) FE model with 0.25 mm mesh size membrane elements

Figure C.1: FE models for the membrane elements mesh refinement study

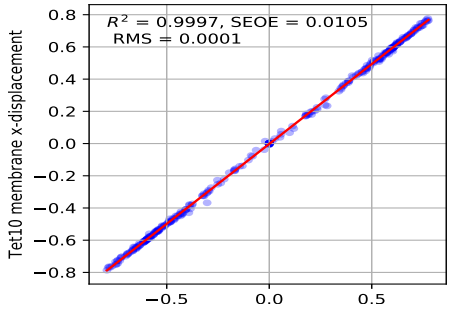

(a) X-displacement

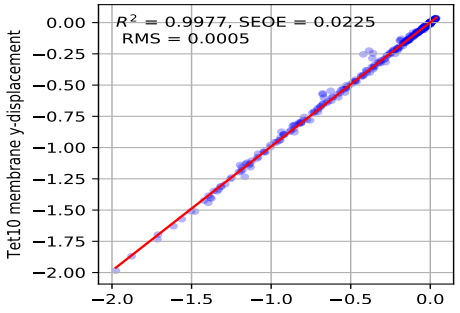

(b) Y-displacement

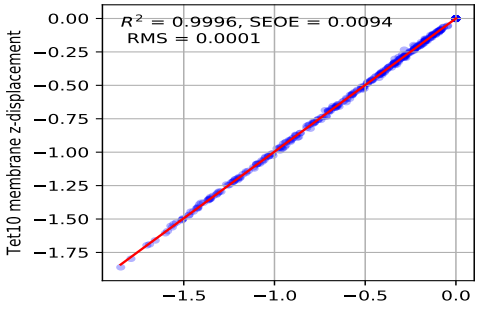

(c) Z-displacement

Figure C.2: Displacement error results with a 1 mm mesh size for the membrane elements

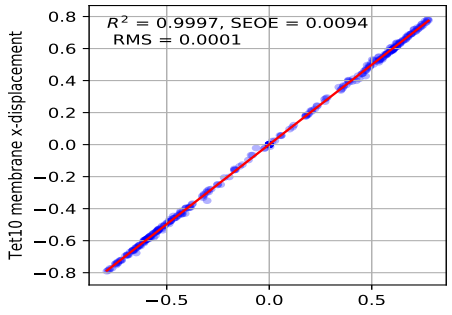

(a) X-displacement

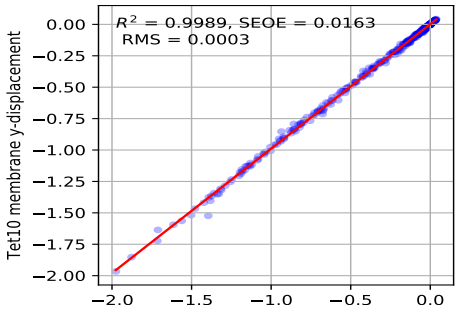

(b) Y-displacement

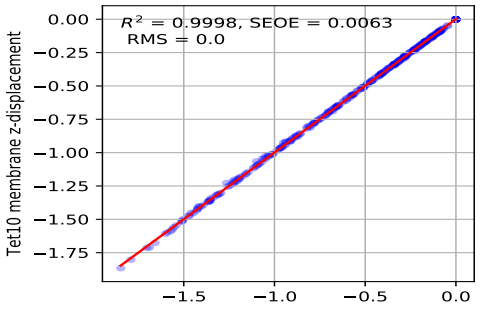

(c) Z-displacement

Figure C.3: Displacement error results with a 0.5 mm mesh size for the membrane elements

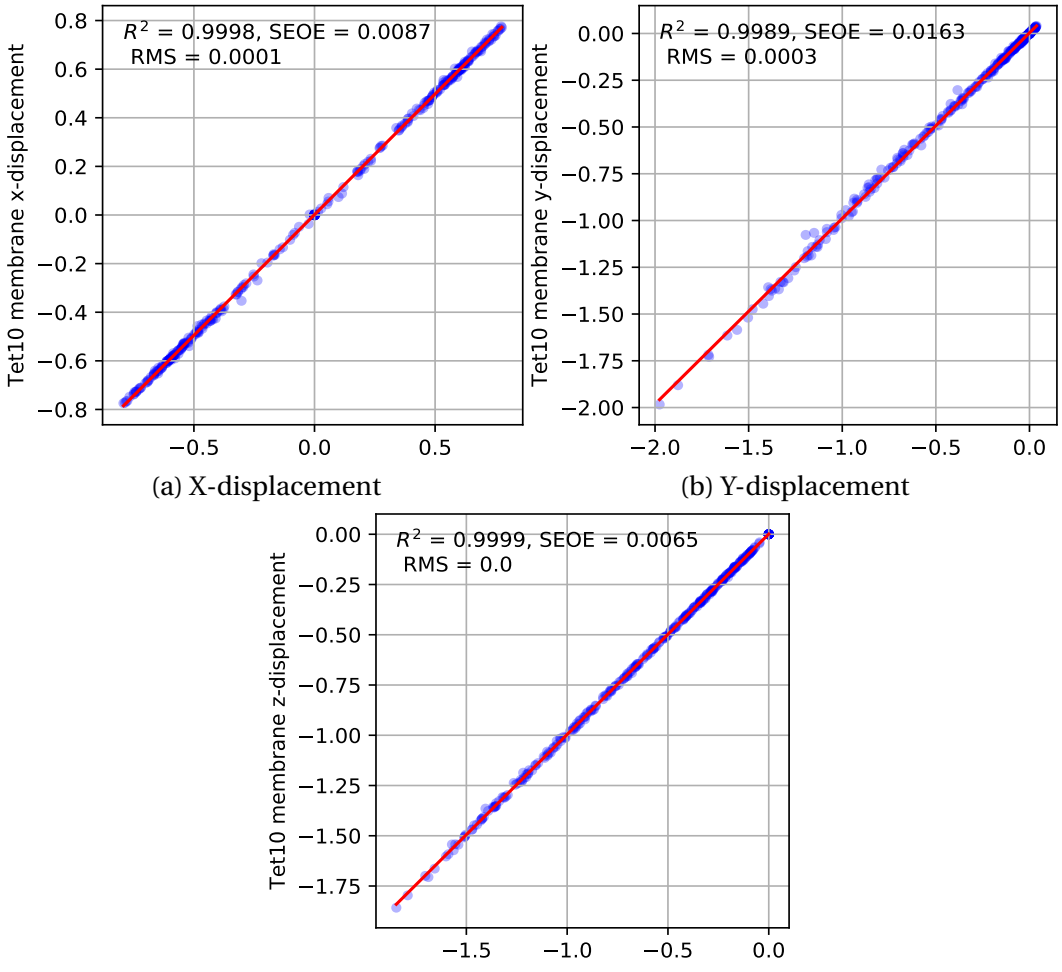

(a) X-displacement

(b) Y-displacement

(c) Z-displacement

Figure C.4: Displacement error results with a 0.25 mm mesh size for the membrane elements

Appendix D

Strain Sensitivity Study

In order to fully understand the results within the final tests in chapter 6, a sensitivity analysis was done for each indentation test to determine the effect each design variable has on the engineering stress and the minimum - and maximum principal strains respectively. The lower and upper bounds for each design variable in table 4.2 were tested individually.

D.1 Engineering Stress vs. Stretch

The engineering stress using, the Mooney-Rivlin three parameter model, can be calculated using Eq. 5.4. Figures D.1 - D.2 represent the effect each material constant within table 4.2, has on the engineering stress for the compression and tension regions respectively. This was done using the material model from table 4.1 and changing each variable, one at a time to the variables within table 4.2. From figure D.1, it can be seen that within the compression region, each variable obtains the same amount of change at a final stretch of 0.4. This maximum change is approximately 1 MPa. It is the C_{10} variable which produces a larger change from a flared out curve downwards. The C_{20} variable produces little change, by starting out tightly around the "Experimental" model's curve, before flaring outwards. From figure D.2, it is the C_{20} variable which produces the most change within the tension region of approximately 1.75 MPa. The C_{01} variable produces the smallest change of less than 0.01 MPa, which means this variable will have very little effect on the test results within the tension region. The C_{10} variable produces a change of approximately 0.5 MPa. It can be observed again that the C_{10} variable starts having an effect at a lower stretch value, but increases with an even effect towards a stretch of 3.0. The C_{20} variable only starts having a detectable effect from 1.5 stretch and increases at an exponential rate towards 3.0 stretch. These variables will all have the same effect in every indentation test for the engineering stress vs. stretch curve, since Eq. 5.4 is used to determine the engineering stress within the inverse FE method.

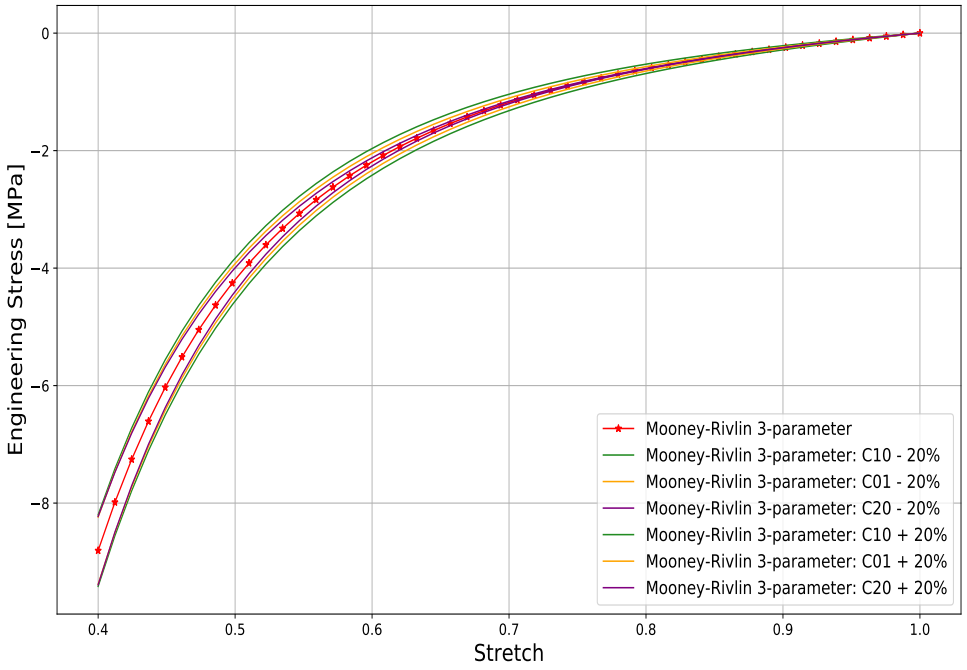

Figure D.1: Mooney-Rivlin material variable sensitivity study of the engineering stress vs. stretch within the compression region

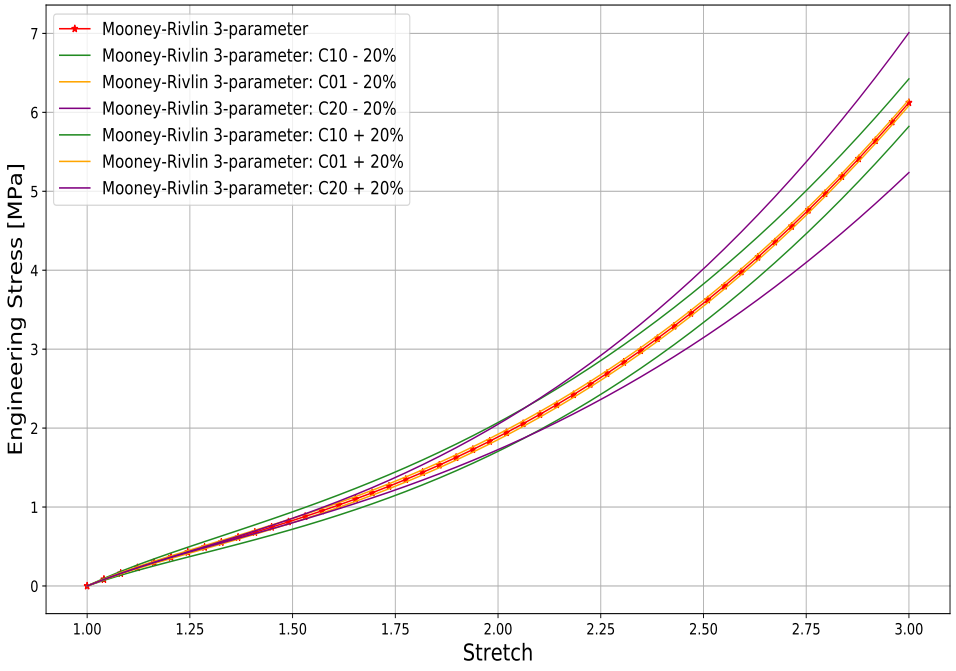

Figure D.2: Mooney-Rivlin material variable sensitivity study of the engineering stress vs. stretch within the tension region

Chapter 5 showed that, due to some glueing contact error within the coarse mesh of the "Numerical" model between the "skin" elements and the sample elements, the principal strains between the two FE models do not match exactly. It was therefore decided to compare the difference in the material variables, for the principal strains, separately for each "Experimental" - and "Numerical" model within each indentation test.

D.2 One Perpendicular Cylindrical Indenter

Figure D.3 depicts the difference each material variable from the Mooney-Rivlin model has on the "Experimental" model for a one cylindrical indenter. It can be observed that each variable does not have a linear relationship with the indentation depth. Within the minimum principal strain, the C_{20} variable has the largest effect of an approximate strain change of 0.075, between the two bounds, at an indentation depth of 3 mm. This variable will cause an overestimation within the minimum principle strain. Both the C_{10} and C_{01} variables will underdetermine the minimum principal strain by a maximum approximate value of 0.025, but with a negligible change between the two bounds. Within the maximum principal strain, the C_{01} and C_{20} variables, contribute a change towards the form of the curve as it approaches an indentation depth of 3.0 mm. All three variables cause a minimal change within the final strain value at a depth of 3 mm. Both the C_{10} and C_{01} variables cause an underdetermination with a maximum value of 0.01

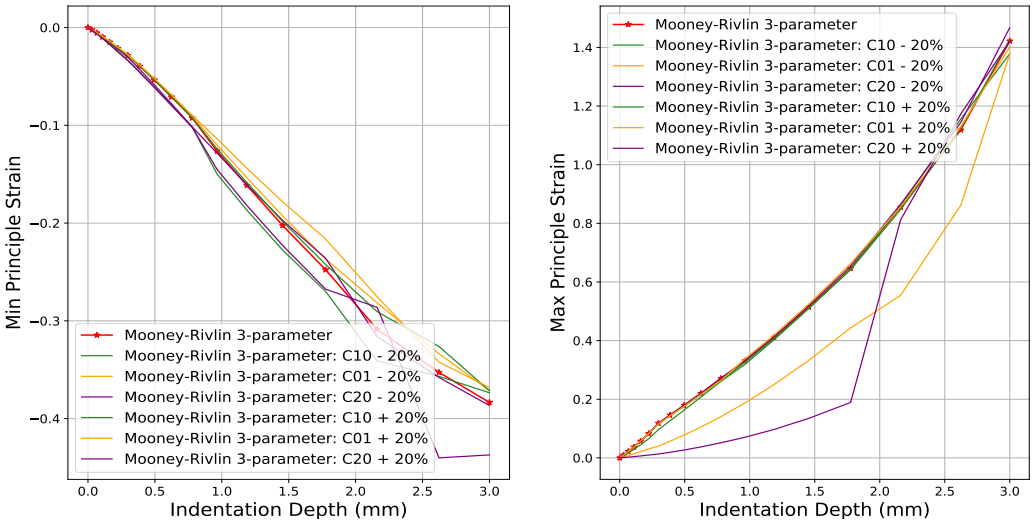

(a) Min. principal strain vs. indentation depth

(b) Max. principal strain vs. indentation depth

Figure D.3: Mooney-Rivlin material model constants' sensitivity study of the Min.- and Max. principal strain vs. indentation depth for the "Experimental" model, for the one perpendicular cylindrical indenter

within the strain. The C_{20} variable causes an overestimation of an approximate maximum change of 0.015 within the strain.

Within figure D.4, each variable causes a significant change within both the principal strain values, for the "Numerical" model. With regard to the minimum principal strain, the C_{10} variable causes the largest change at an indentation depth of 3 mm, with a maximum approximate value of 0.16 between the bounds. The C_{20} variable has the second largest change of a maximum approximate value of 0.055, leaving the C_{01} variable with a mere 0.01 maximum change. With regard to the maximum principal strain, the C_{01} and C_{20} variables have significant effect in the form of the curve towards an indentation depth of 3 mm. The C_{20} variable causes the largest change in form and change at a depth of 3 mm, of a maximum approximate strain change of 4.4. The C_{01} variable causes a maximum approximate strain change of 1.9, throughout the entire indentation depth. Variable C_{10} causes a maximum approximate strain change of 2.0, from an indentation depth range of 2 mm - 3 mm.

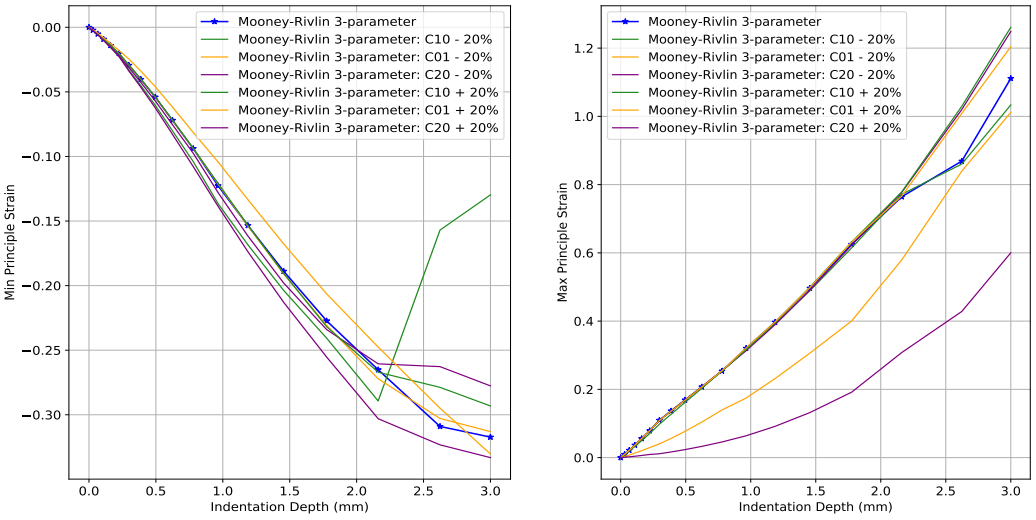

(a) Min. principal strain vs. indentation depth

(b) Max. principal strain vs. indentation depth

Figure D.4: Mooney-Rivlin material model constants' sensitivity study of the Min.- and Max. principal strain vs. indentation depth for the "Numerical" model for the one perpendicular cylindrical indenter

D.3 Two Perpendicular Cylindrical Indenters

Within figure D.5, it can be observed that the different material variables cause minimal strain changes for the "Experimental" model. Within the minimum principal strain region, the variables have a negligibly small change within the final strain value at an indentation depth of 3 mm. There is a slight underestima-

tion of the strain value at an indentation depth of 2 mm, where the C_{01} and C_{20} variables cause the largest strain change of approximately 0.04. With regard to the maximum principal strain, all three variables cause a more downward bulge within the form of the curve, as it approaches its final strain value at an indentation depth of 3 mm. Between the two bounds for the C_{01} variable, an underestimation of a maximum approximate strain change of 0.15 occurs.

Figure D.6 shows the effect the material variables has on the "Numerical" model's principal strain values. Within both principal strains, the variables cause a bit of an unstable strain change as they approach their final values at an indentation depth of 3 mm. This is due to the error within the contact tolerance within the "Numerical" model. Regardless of the contact error, the variables cause a small change within the final minimum principal strain value at a depth of 3 mm. With regard to the maximum principal strain, the variables cause a significant change within the final strain value at an indentation depth of 3 mm. The C_{01} variable causes the largest strain change of approximately 0.62, followed by the C_{10} variable with an approximate strain change of 0.6.

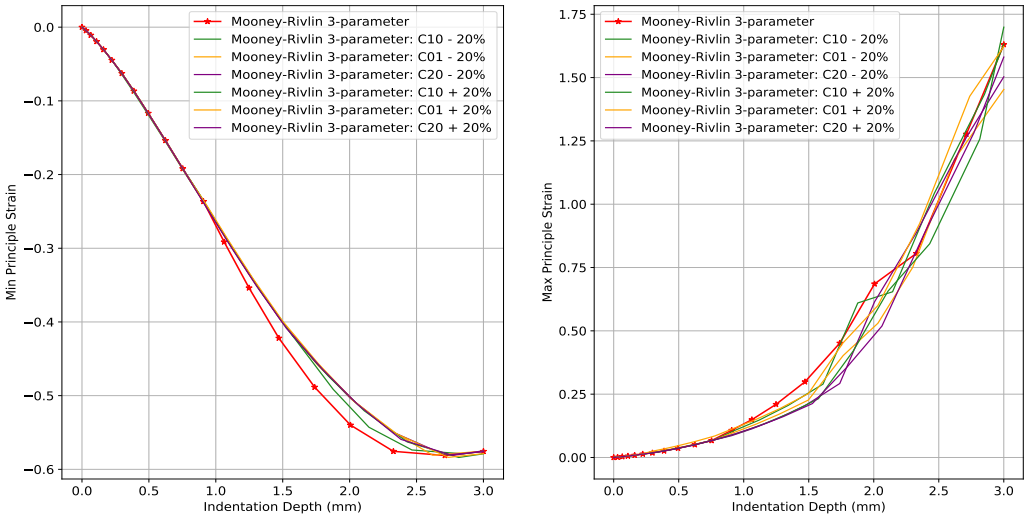

(a) Min. principal strain vs. indentation depth

(b) Max. principal strain vs. indentation depth

Figure D.5: Mooney-Rivlin material model constants' sensitivity study of the Min.- and Max. principal strain vs. indentation depth for the "Experimental" model for the two perpendicular cylindrical indenters

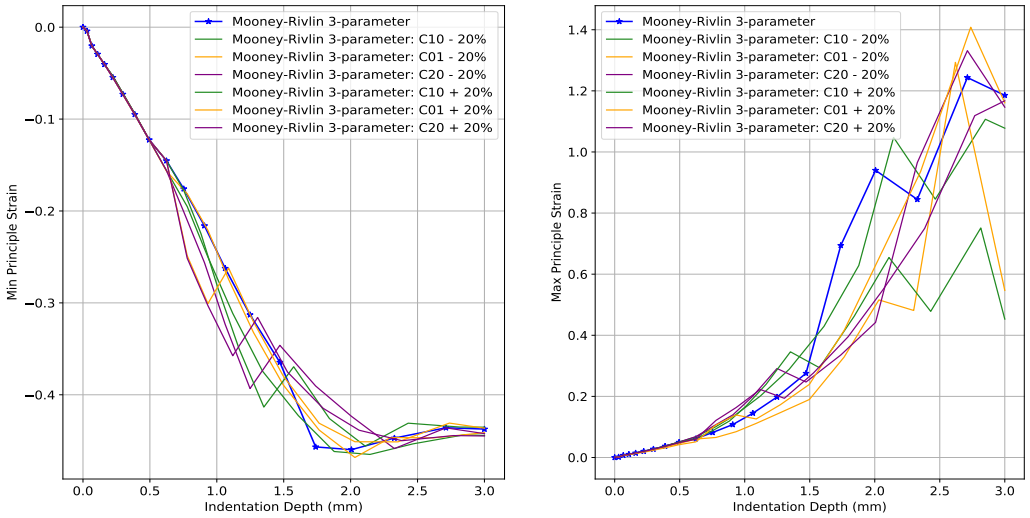

(a) Min. principal strain vs. indentation depth

(b) Max. principal strain vs. indentation depth

Figure D.6: Mooney-Rivlin material model constants' sensitivity study of the Min.- and Max. principal strain vs. indentation depth for the "Numerical" model for the two perpendicular cylindrical indenters

D.4 Parallel Cylindrical Indenter

Figure D.7 represents the effect the different material variables have on the "Experimental" model for the parallel indenter. Within the minimum principal strain curve, the C_{01} variable causes a sharp, linear curvature towards the final strain value, at an indentation depth of 1.5 mm, followed by a horizontal progression at approximately the same minimum strain value up until an indentation depth of 3 mm. This variable causes a final strain change of approximately 0.025. Between the two outer bounds for the C_{20} variable, a constant maximum strain change of approximately 1.1, follows the original curve for the entire depth range, until both bounds converge to the same final strain value, which has a negligible strain change from the original curve's final value. It is the C_{10} variable which causes the largest strain change and form change between the two boundary values. But both curves converge towards each other at an indentation depth of 3 mm, with a final maximum strain change of approximately 0.04.

Figure D.8 represents the effect each material variable has on the principal strains within the "Numerical" model. With regards to the minimum principal strain, the variables cause the same effect it did for the "Experimental" model, but with different strain changes due to the difference in the original material model's curve. The same can be said for the maximum principal strain. The difference in the maximum principal strain, is that the variables cause the curve to obtain a better fit towards the "Experimental" model's curve, which can be

beneficial in obtaining a material model during the inverse FE analysis, which will be a better fit than the original material model.

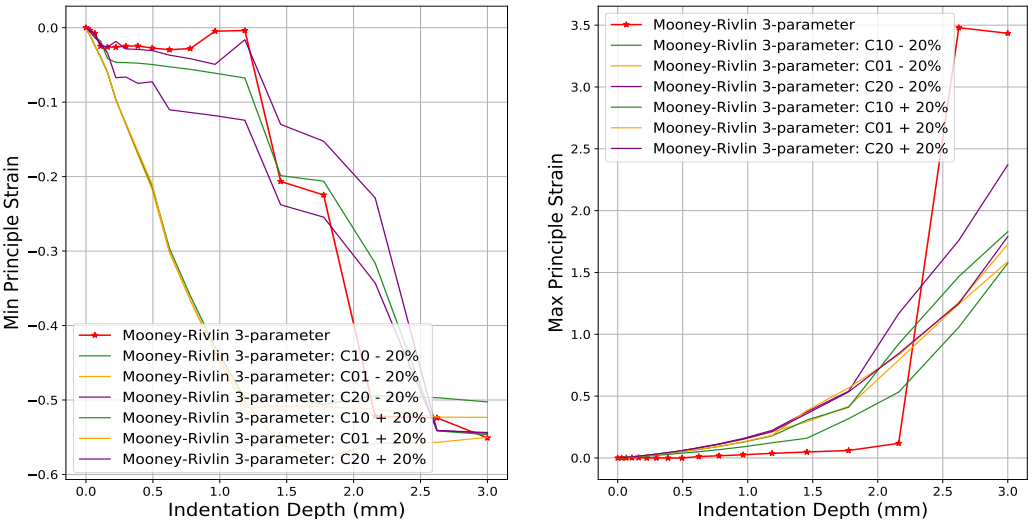

(a) Min. principal strain vs. indentation depth

(b) Max. principal strain vs. indentation depth

Figure D.7: Mooney-Rivlin material model constants' sensitivity study of the Min.- and Max. principal strain vs. indentation depth for the "Experimental" model for the parallel cylindrical indenter

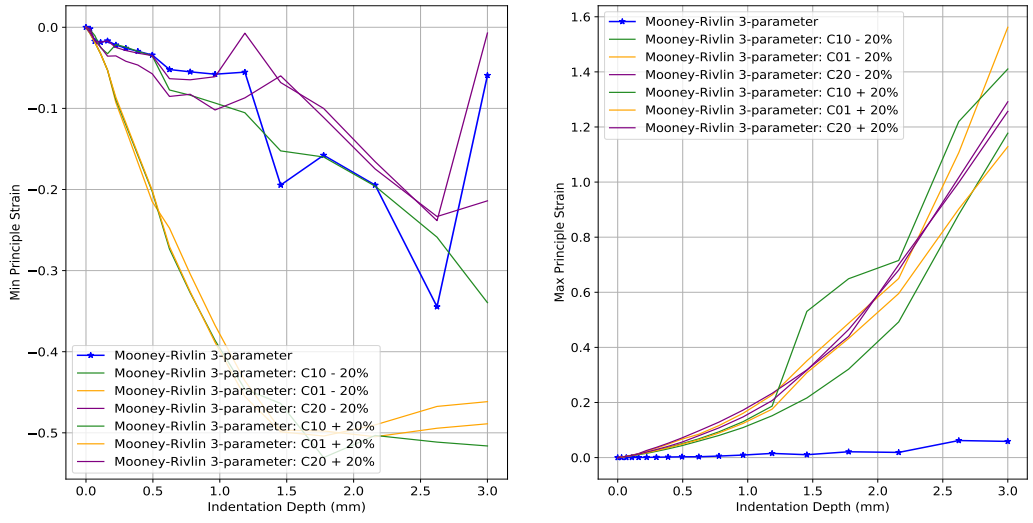

(a) Min. principal strain vs. indentation depth

(b) Max. principal strain vs. indentation depth

Figure D.8: Mooney-Rivlin material model constants' sensitivity study of the Min.- and Max. principal strain vs. indentation depth for the "Numerical" model for the parallel cylindrical indenter

D.5 Diagonal Cylindrical Indenter

Figure D.9 represents the material variable's effect within the "Experimental" model. Within the minimum principal strain, the C_{20} variable causes the largest strain change, by firstly causing the curve to reach its approximate maximum, minimum principal strain value at an indentation depth of 1 mm and then to further progress with an approximate constant strain value towards an indentation depth of 3 mm. At any given point, this variable will cause a maximum strain change of approximately 0.14. The other two variables have approximately the same effect, but with a much lower strain change. It is the C_{10} variable which causes the largest strain change of approximately 0.06, at an indentation depth of 3 mm. For the maximum principal strain, the variables have a very small effect on the form of the curve, or the final strain value, save for the C_{10} variable. This variable can cause up to an approximate maximum strain change of 16, which is a bit suspicious and can be linked to an error within the contact tolerance.

Figure D.10 represents the effect the material variables have on the "Numerical" model's principal strain curves for a diagonal cylindrical indenter. For the minimum principal strain, the variables have the same effect they have for the "Experimental" model. For the maximum principal strain, again the variables have the same effect they have for the "Experimental" model, save for the C_{20} variable and the strain changes. Within the "Numerical" model, the C_{20} variable has an approximate, maximum strain change of 6.2, followed by the C_{01} variable with a maximum, approximate strain change of 4.0. Finally the C_{20} variable

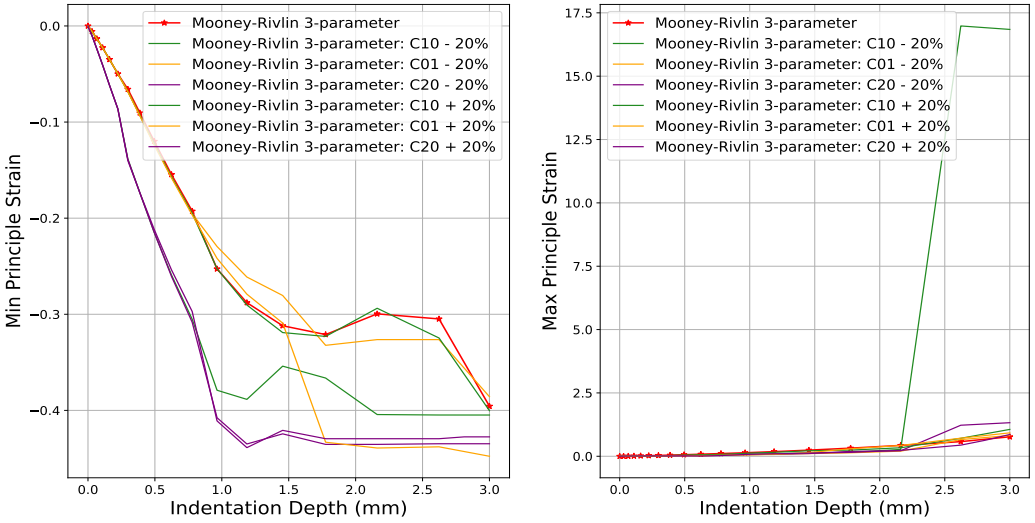

(a) Min. principal strain vs. indentation depth

(b) Max. principal strain vs. indentation depth

Figure D.9: Mooney-Rivlin material model constants' sensitivity study of the Min.- and Max. principal strain vs. indentation depth for the "Experimental" model for the diagonal cylindrical indenter

causes an approximate, maximum strain change of 2.5.

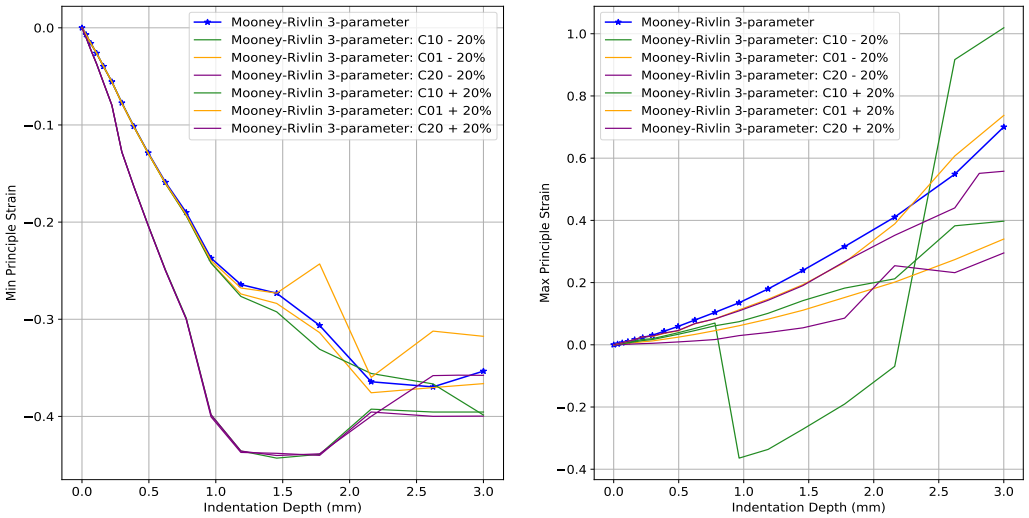

(a) Min. principal strain vs. indentation depth

(b) Max. principal strain vs. indentation depth

Figure D.10: Mooney-Rivlin material model constants' sensitivity study of the Min.- and Max. principal strain vs. indentation depth for the "Numerical" model for the diagonal cylindrical indenter

D.6 One Spherical Indenter

Figure D.11 represents the effect the material variables have on the "Experimental" model for one spherical indenter. Within the minimum principal strain, the C_{10} and C_{20} variables cause a change in the curvature of the final curve, with the bounds from the C_{20} variable converging to the same final strain value at an indentation depth of 3 mm. The bounds of the C_{10} variable cause a maximum, approximate strain change of 1.5, at an indentation depth of 3 mm. The $C01$ variable causes the original curve to smooth out and progress at a linear rate toward its final strain value, causing an approximate maximum strain change of 2.0 at an indentation depth of 3 mm. For the maximum principal strain, all three variables cause an underestimate for the final strain value, with an approximate maximum strain change of 2.0. It is the C_{20} variable which causes a bit of change in the form of the curve as well.

Figure D.12 represents the effect the material variables have on the principal strain curves within the "Numerical" model. For the minimum principal strain, the variables have the same effect they have on the "Experimental" model, save for the C_{10} variable. The C_{10} variable causes an unexpected positive strain change towards the maximum principal strain region, which can only be explained by an error within the FE analysis. For the maximum principal strain, the variables

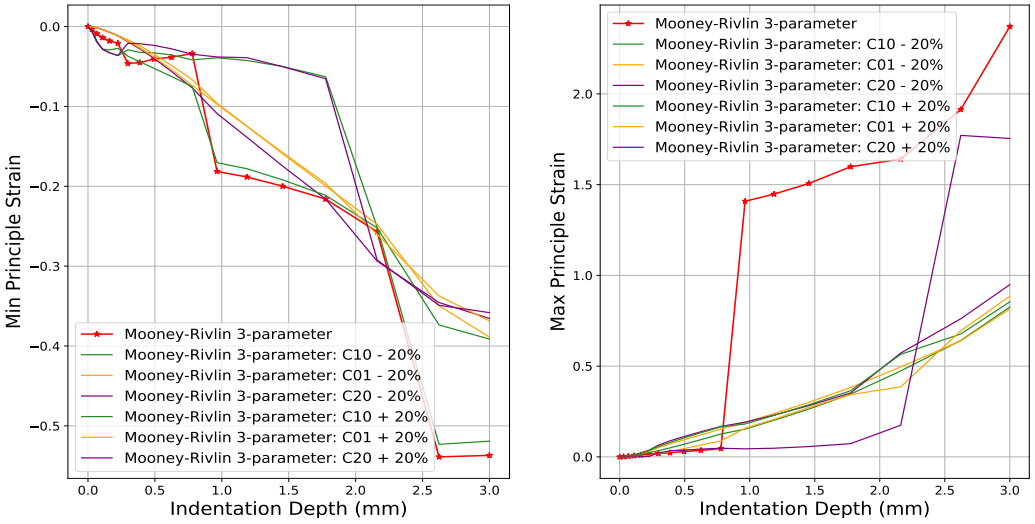

(a) Min. principal strain vs. indentation depth

(b) Max. principal strain vs. indentation depth

Figure D.11: Mooney-Rivlin material model constants' sensitivity study of the Min.- and Max. principal strain vs. indentation depth for the "Experimental" model for the one spherical indenter

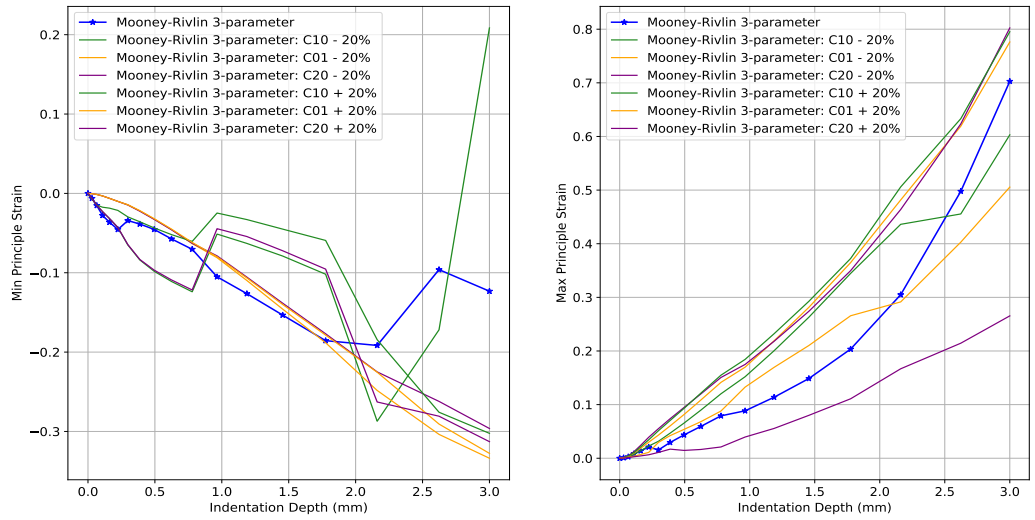

(a) Min. principal strain vs. indentation depth

(b) Max. principal strain vs. indentation depth

Figure D.12: Mooney-Rivlin material model constants' sensitivity study of the Min.- and Max. principal strain vs. indentation depth for the "Numerical" model for the one spherical indenter

cause a large strain change within the final strain value at and indentation depth of 3 mm. The C_{20} variable causes the largest strain change of approximately 5.4, followed by the C_{10} variable with an approximate, maximum strain change of 2.8. Lastly the C_{01} variable causes an approximate, maximum strain change of 2.0.

D.7 Two Spherical Indenters

Figure D.13 represents the effect the material variables have on the principal strain curves for the "Experimental" model. For the minimum principal strain, all three variables cause a constant strain change between the two boundary curves, as they progress towards their respective final strain values, at an indentation depth of 3 mm. The C_{20} variable causes the largest strain change of approximately 1.5, followed by the C_{01} variable with an approximate strain change of 1.2. Finally the C_{10} variable causes an approximate strain change of 0.2. Within the maximum principal strain curve, the variables follow the same curvature than the original model curve, but end with a final strain value. The C_{10} variable causes the largest strain change of approximately 0.85, followed by the C_{01} variable with an approximate strain change of 0.25, followed lastly with the C_{20} variable, with an approximate strain change of 0.19.

Figure D.14, represents the effect the material variables have on the principal strain curves for the "Numerical" model. For the minimum principal strain, the C_{10} variable causes a linear curve to eventually overestimate the final min-

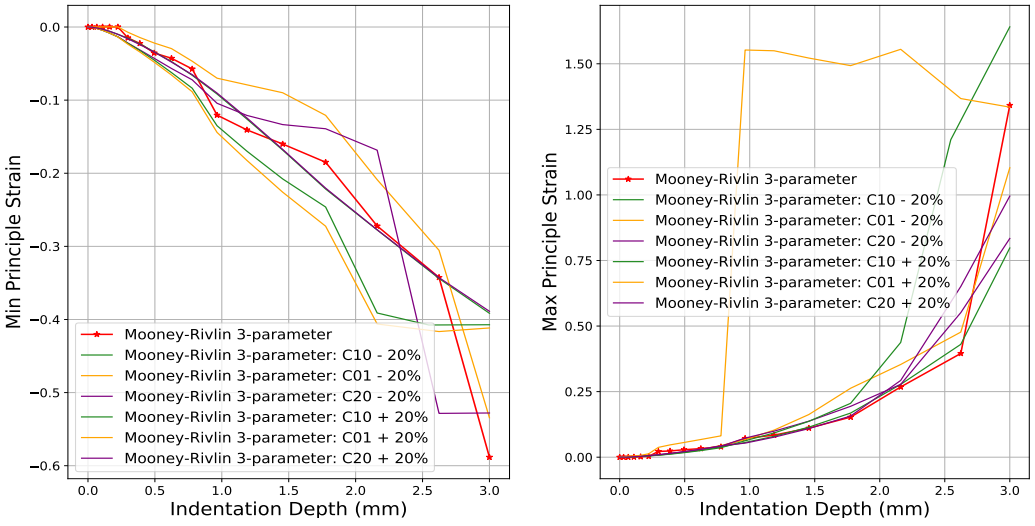

(a) Min. principal strain vs. indentation depth

(b) Max. principal strain vs. indentation depth

Figure D.13: Mooney-Rivlin material model constants' sensitivity study of the Min.- and Max. principal strain vs. indentation depth for the "Experimental" model for the two spherical indenters

imum strain value. This variable causes a final approximate strain change between the two boundary curves of 0.05. Both the C_{01} and C_{20} variables follow a linear progression along with the original curve, before splitting at the second last increment to form a large strain range between the two boundary curves for each variable respectively. The C_{20} variable causes the largest strain change at a 3 mm indentation, of an approximate maximum strain change of 1.8, followed by the C_{01} variable with an approximate, maximum strain change of 1.65. For the maximum principal strain, the C_{10} variable causes a linear curve to again, overestimate the final strain value at an indentation depth of 3 mm. Between the two boundary curves of the variable C_{10}, an approximate strain change of 0.1 can be obtained. Between the two boundary curves of the C_{01} variable, a negligible strain change can be obtained, since both curves progress linearly towards the same final strain value, which causes an overestimate from the original strain value. This strain change is approximately equal to 2.0. The same behaviour for the C_{20} variable is obtained as in the minimum principal strain curve, with a maximum approximate strain change of 7.4 between the two boundary curves.

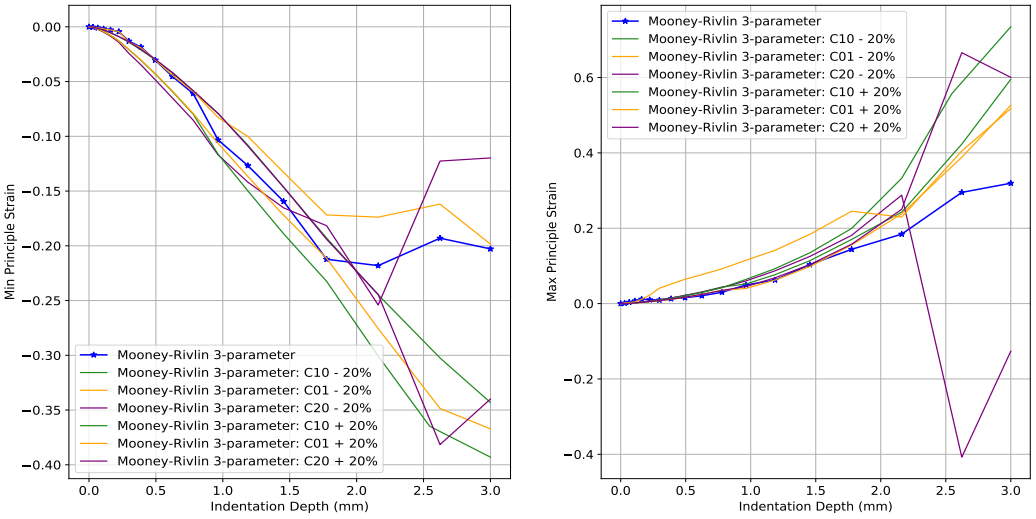

(a) Min. principal strain vs. indentation depth

(b) Max. principal strain vs. indentation depth

Figure D.14: Mooney-Rivlin material model constants' sensitivity study of the Min.- and Max. principal strain vs. indentation depth for the "Numerical" model for the two spherical indenters

D.8 Summary and Final Remarks

For the one perpendicular, cylindrical indenter, the C_{10} and C_{20} variables have the largest effect with regards to the form and final strain value. For the "Numer-

ical" model, it can be observed that both of these variables will be able to improve the error between the "Experimental" model and the "Numerical" model.

By using two cylindrical indenters, it can be observed that within the "Numerical" model, all three variables have a significant effect on the curve, therefore it will be desirable to obtain optimised variables closer to the original parameters.

Using a parallel cylindrical indenter, the C_{01} variable changes the shape of the curve substantially. For the "Numerical" model, it will be desirable to obtain a material model close to the limits, since a combination of them might improve the curvature and final strain value at an indentation depth of 3 mm and a better fit towards the "Experimental" model.

With the diagonal cylindrical indenter, the C_{10} and C_{20} variables cause the largest changes within the curvature and final strain value. Here it will be desirable to obtain a material model within the "Numerical" model, with the variables close to the original model's, since the "Numerical" model showed a close fit towards the "Experimental" model, as shown in chapter 5.

For the one spherical indenter, the large change the C_{20} and C_{10} variable contribute to the curvature and strain values, it will be desirable to obtain a material model close to the bounds. Chapter 5 indicated that a poor fit is present between the "Experimental" model and the "Numerical" model, with the original model. Therefore a better fit might be possible with the improved material variables.

For the two spherical indenters, the C_{10} and C_{01} contribute to an improved curvature within the "Numerical" model. It will be desirable to obtain boundary values for these variables through the analysis.

Overall, it seems that the C_{10} and C_{20} variables have the largest effect within all the indentation tests. Ideally, the idea is to obtain the same material model in order to validate that the particular indentation method will be able to accurately characterise the material model. Unfortunately an error between the two FE models exist, due to contact error within the FE analysis. More than one set of material variables exist for a hyper-elastic material, using a constitutive material model such as the Mooney-Rivlin three parameter model. If a new set of variables can be obtained within the "Numerical" model, which obtains a better fit towards the "Experimental" model, the indentation method can be concluded to be successful since it improved the original results.

Appendix E

Results

E.1 One Perpendicular Cylindrical Indenter

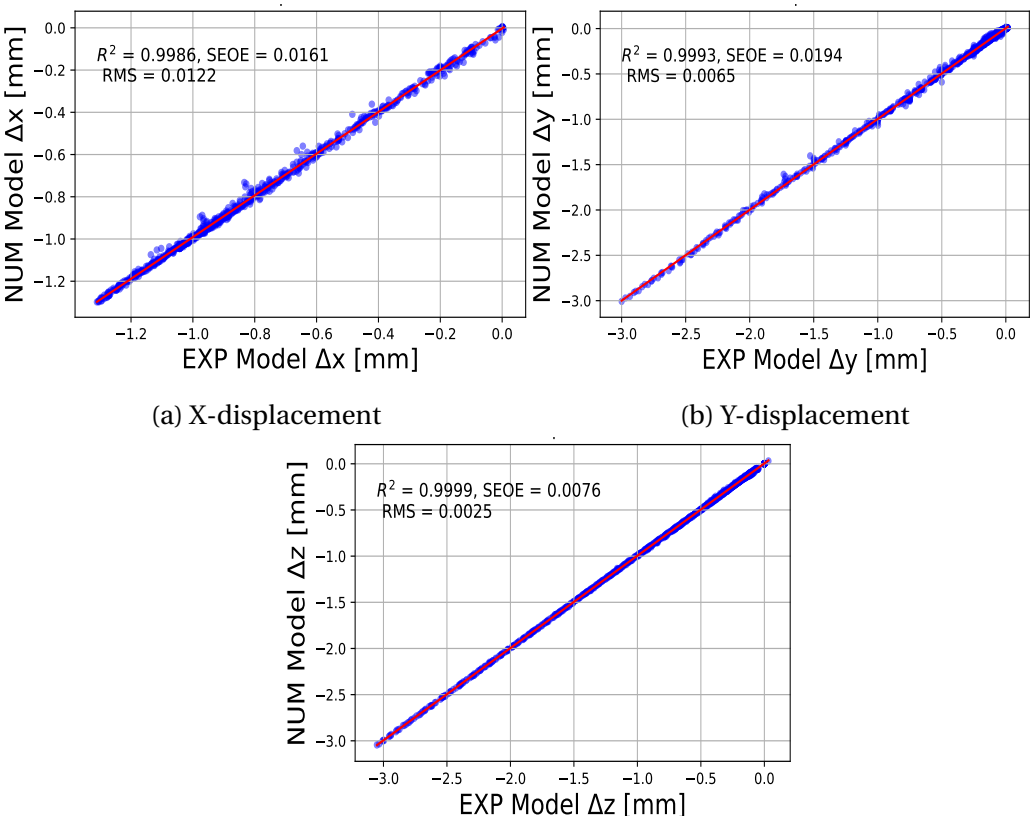

(a) X-displacement

(b) Y-displacement

(c) Z-displacement

Figure E.1: Displacement errors, for the results with the best objective function, for the one perpendicular cylindrical indenter, with the SLP algorithm

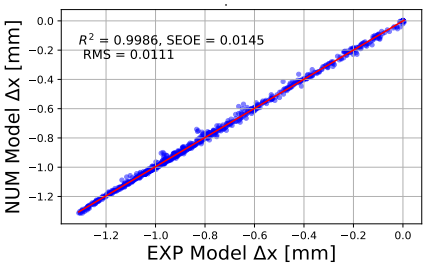

(a) X-displacement

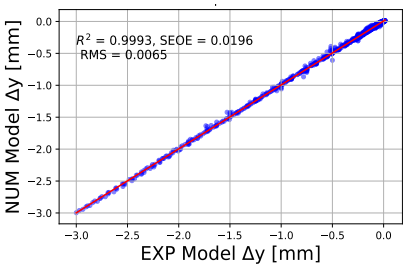

(b) Y-displacement

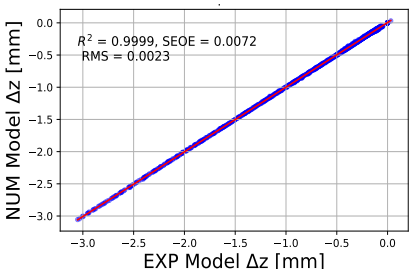

(c) Z-displacement

Figure E.2: Displacement errors, for the results with the best objective function, for the one perpendicular cylindrical indenter, with the SQP algorithm

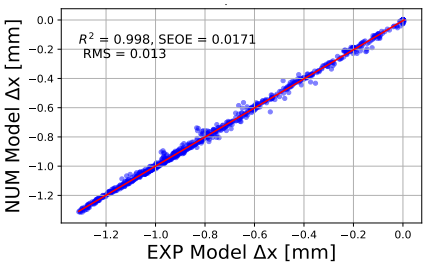

(a) X-displacement

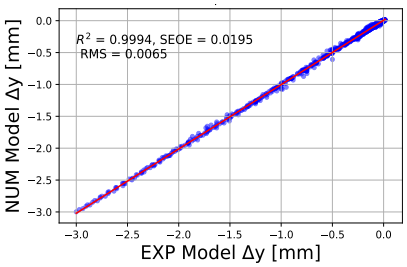

(b) Y-displacement

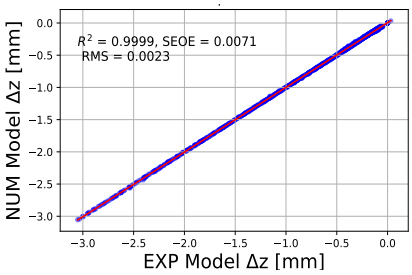

(c) Z-displacement

Figure E.3: Displacement errors, for the results with the best curve fitting results, for the one perpendicular cylindrical indenter, with the SQP algorithm

E.2 Two Perpendicular Cylindrical Indenters

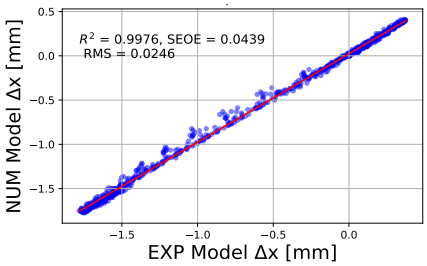

(a) X-displacement

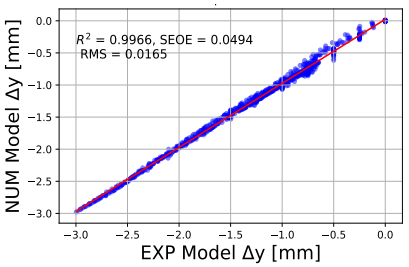

(b) Y-displacement

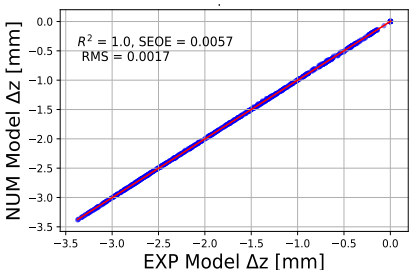

(c) Z-displacement

Figure E.4: Displacement errors, for the results with the best objective function, for the two perpendicular cylindrical indenters, with the SLP algorithm

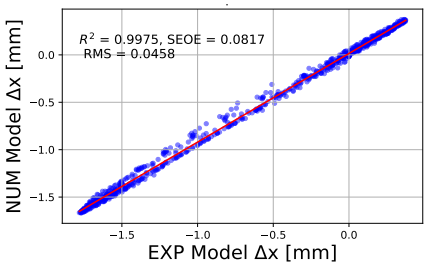

(a) X-displacement

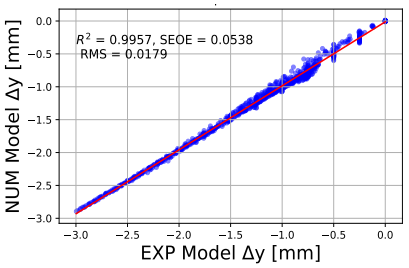

(b) Y-displacement

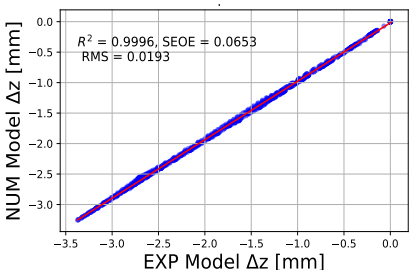

(c) Z-displacement

Figure E.5: Displacement errors, for the results with the best objective function, for the two perpendicular cylindrical indenters, with the SQP algorithm

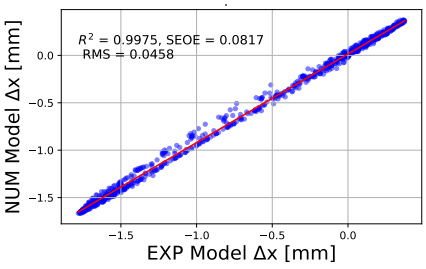

(a) X-displacement

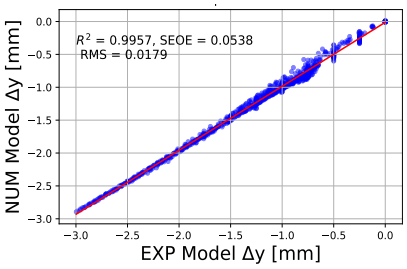

(b) Y-displacement

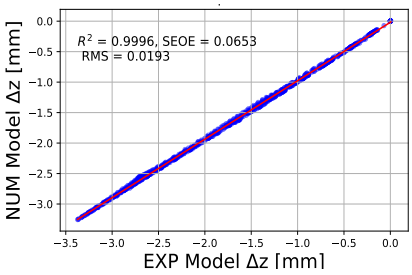

(c) Z-displacement

Figure E.6: Displacement errors, for the results with the best curve fitting results, for the two perpendicular cylindrical indenters, with the SQP algorithm

E.3 Parallel Cylindrical Indenter

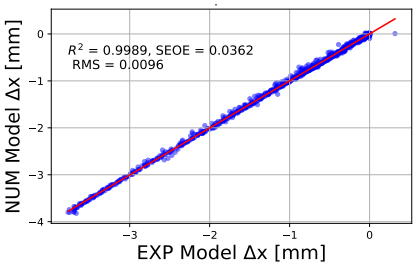

(a) X-displacement

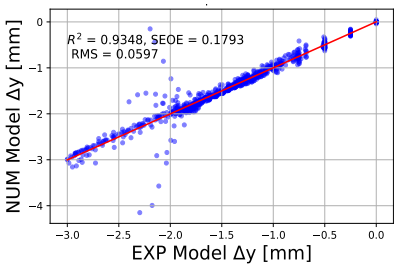

(b) Y-displacement

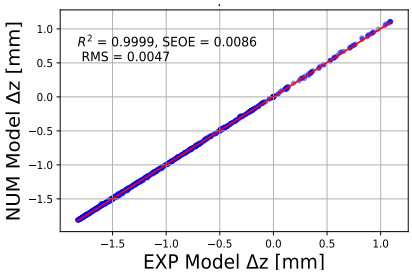

(c) Z-displacement

Figure E.7: Displacement errors, for the results with the best objective function, for the parallel cylindrical indenter, with the SLP algorithm

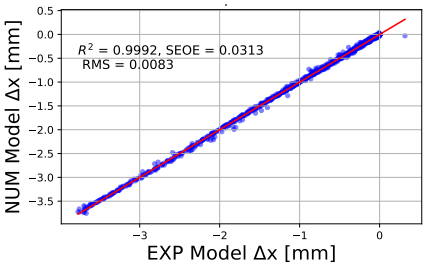

(a) X-displacement

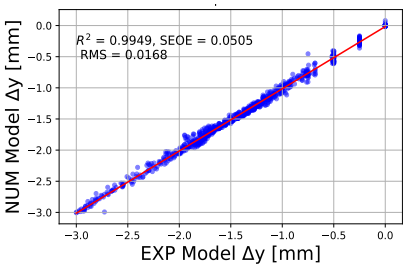

(b) Y-displacement

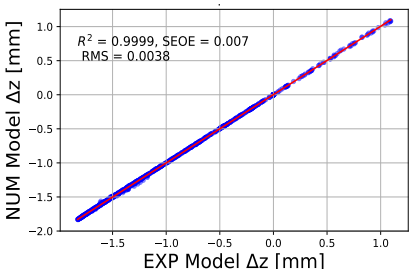

(c) Z-displacement

Figure E.8: Displacement errors, for the results with the best objective function, for the parallel cylindrical indenter, with the SQP algorithm

E.4 Diagonal Cylindrical Indenter

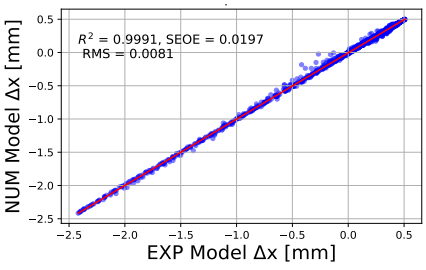

(a) X-displacement

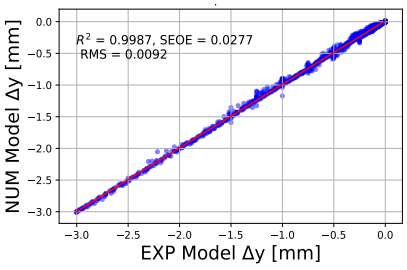

(b) Y-displacement

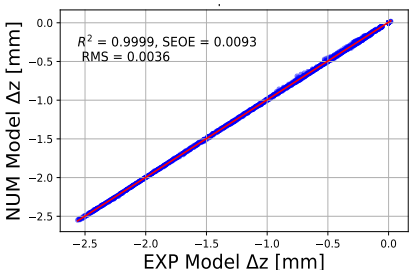

(c) Z-displacement

Figure E.9: Displacement errors, for the results with the best objective function, for the diagonal cylindrical indenter, with the SLP algorithm

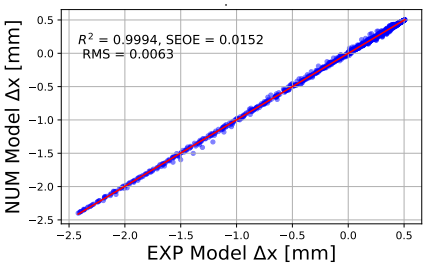

(a) X-displacement

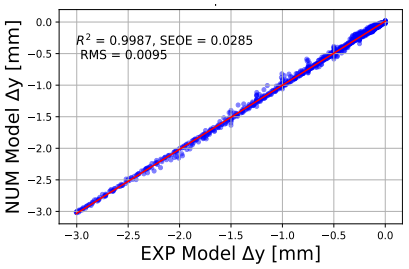

(b) Y-displacement

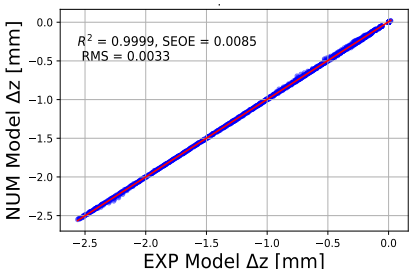

(c) Z-displacement

Figure E.10: Displacement errors, for the results with the best objective function, for the diagonal cylindrical indenter, with the SQP algorithm

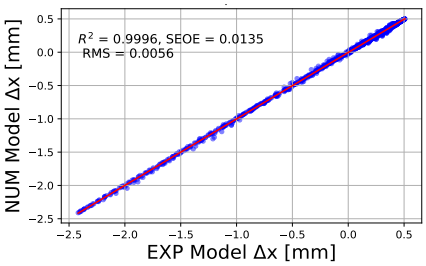

(a) X-displacement

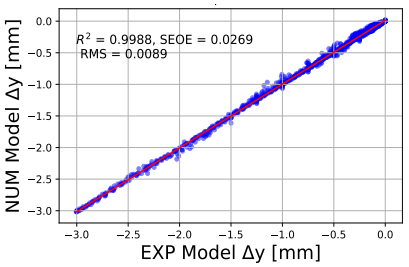

(b) Y-displacement

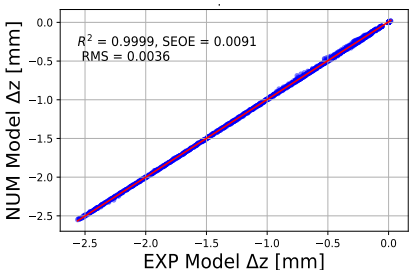

(c) Z-displacement

Figure E.11: Displacement errors, for the results with the best fitted results, for the diagonal cylindrical indenter, with the SQP algorithm

E.5 One Spherical Indenter

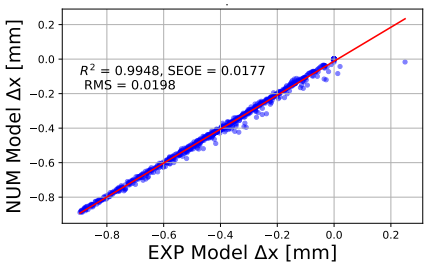

(a) X-displacement

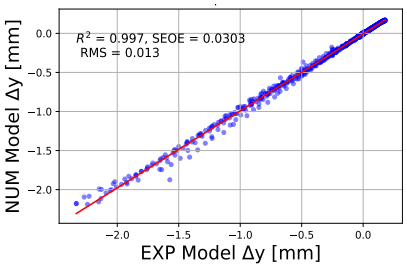

(b) Y-displacement

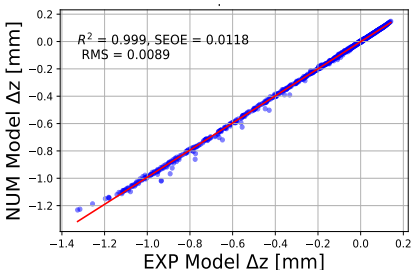

(c) Z-displacement

Figure E.12: Displacement errors, for the results with the best objective function, for the one spherical indenter, with the SLP algorithm

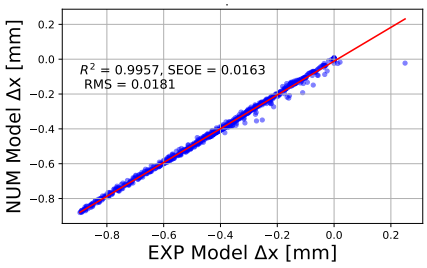

(a) X-displacement

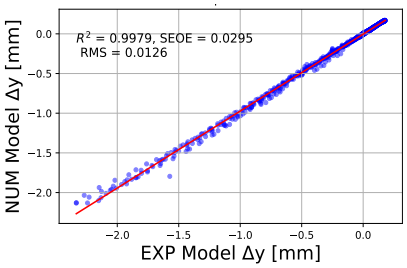

(b) Y-displacement

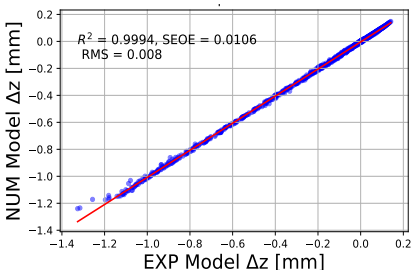

(c) Z-displacement

Figure E.13: Displacement errors, for the results with the best objective function, for the one spherical indenter, with the SQP algorithm

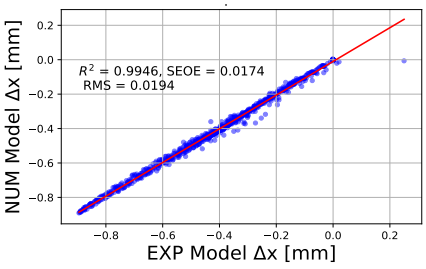

(a) X-displacement

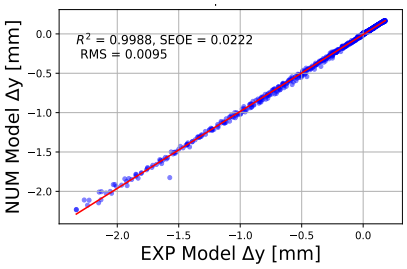

(b) Y-displacement

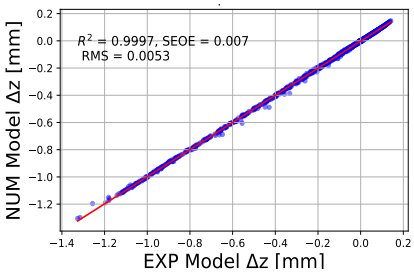

(c) Z-displacement

Figure E.14: Displacement errors, for the results with the best fitted results, for the one spherical indenter, with the SQP algorithm

E.6 Two Spherical Indenters

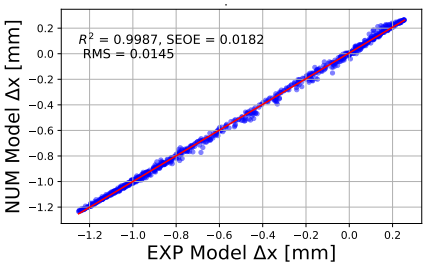

(a) X-displacement

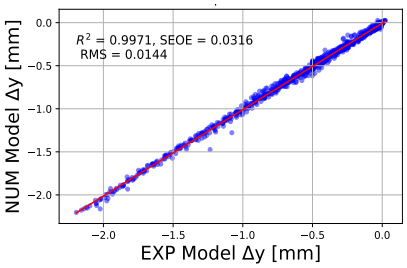

(b) Y-displacement

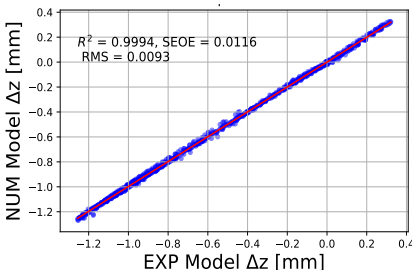

(c) Z-displacement

Figure E.15: Displacement errors, for the results with the best objective function, for the two spherical indenters, with the SLP algorithm

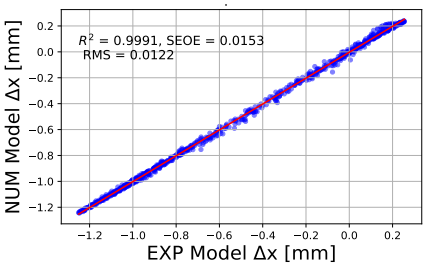

(a) X-displacement

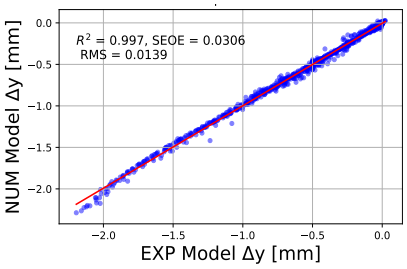

(b) Y-displacement

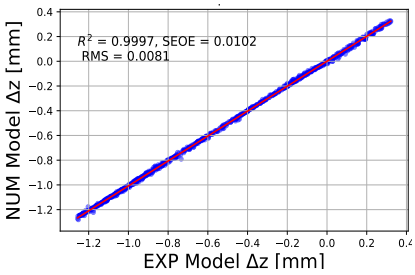

(c) Z-displacement

Figure E.16: Displacement errors, for the results with the best objective function, for the two spherical indenters, with the SQP algorithm

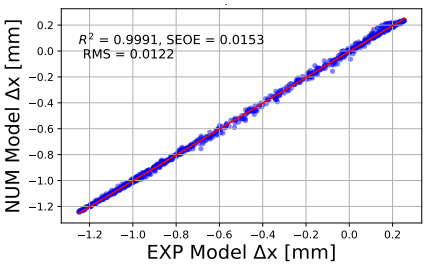

(a) X-displacement

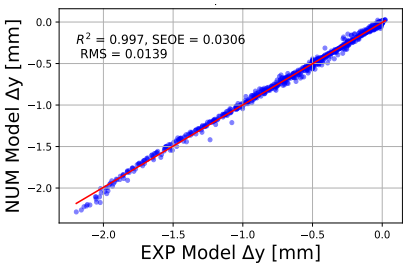

(b) Y-displacement

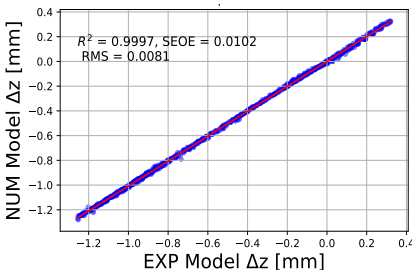

(c) Z-displacement

Figure E.17: Displacement errors, for the results with the best fitted results, for the two spherical indenters, with the SQP algorithm

List of References

Abbasi, M., Barakat, M.S., Vahidkhah, K. and Azadani, A.N. (2016). Characterization of three-dimensional anisotropic heart valve tissue mechanical properties using inverse finite element analysis. *Journal of the Mechanical Behavior of Biomedical Materials*, vol. 62, pp. 33–44. ISSN 18780180.
Available at: http://dx.doi.org/10.1016/j.jmbbm.2016.04.031

Buhmann, M. (2010). Radial basis function. *Scholarpedia*, vol. 5, no. 5, p. 9837. Revision #137035.

Buljak, V., Cocchetti, G., Cornaggia, A. and Maier, G. (2017). Estimation of residual stresses by inverse analysis based on experimental data from sample removal for âsmall punchâ tests. *Engineering Structures*, vol. 136, pp. 77–86. ISSN 18737323.
Available at: http://dx.doi.org/10.1016/j.engstruct.2016.12.062

Case, J.C., White, E.L. and Kramer, R.K. (2015). Soft material characterization for robotic applications. *Soft Robotics*, vol. 2, no. 2, pp. 80–87. ISSN 21695172.

Chai, C.K., Akyildiz, A.C., Speelman, L., Gijsen, F.J., Oomens, C.W., van Sambeek, M.R., van der Lugt, A. and Baaijens, F.P. (2014). Local anisotropic mechanical properties of human carotid atherosclerotic plaques - Characterisation by micro-indentation and inverse finite element analysis. *Journal of the Mechanical Behavior of Biomedical Materials*, vol. 43, pp. 59–68. ISSN 18780180.
Available at: http://dx.doi.org/10.1016/j.jmbbm.2014.12.004

Chai-ead, N., Aungkulanon, P. and Luangpaiboon, P. (2011). Bees and firefly algorithms for noisy non-linear optimisation problems. *IMECS 2011 - International MultiConference of Engineers and Computer Scientists 2011*, vol. 2, pp. 1449–1454. ISSN 2078-0958.

Garbowski, T., Maier, G. and Novati, G. (2012). On calibration of orthotropic elastic-plastic constitutive models for paper foils by biaxial tests and inverse analyses. *Structural and Multidisciplinary Optimization*, vol. 46, no. 1, pp. 111–128. ISSN 1615147X.

Holzapfel, G.A. (2016). Similarities between soft biological tissues and rubberlike materials. , no. March.

Holzapfel, G.A., Gasser, T.C. and Ogden, R.W. (2000). A new constitutive framework for arterial wall mechanics and a comparative study of material models. *Journal of Elasticity*, vol. 61, no. 1-3, pp. 1–48. ISSN 03743535. A:1010835316564.

Holzapfel, G.A. and Ogden, R.W. (2009). On planar biaxial tests for anisotropic nonlinearly elastic solids. A continuum mechanical framework. *Mathematics and Mechanics of Solids*, vol. 14, no. 5, pp. 474–489. ISSN 10812865.

Jan A. Snyman, D.N.W. (2005). *Practical Mathematical Optimization*. Springer, New York.

Jekel, C.F., Venter, G. and Venter, M.P. (2016). *Obtaining Non-linear Orthotropic Material Models for PVC-Coated Polyester via Inverse Bubble Inflation*. Master's thesis, Stellenbosch University.

Kim, B., Lee, S.B., Lee, J., Cho, S., Park, H., Yeom, S. and Park, S.H. (2012). A comparison among Neo-Hookean model, Mooney-Rivlin model, and Ogden model for Chloroprene rubber. *International Journal of Precision Engineering and Manufacturing*, vol. 13, no. 5, pp. 759–764. ISSN 12298557.

LaVision (2014). *Product-manual davis 8.2 software*.

Lee, A. (2013-2014). Design of experiments for python.
Available at: `https://pythonhosted.org/pyDOE/randomized.html`

Liu, K., VanLandingham, M.R. and Ovaert, T.C. (2009). Mechanical characterization of soft viscoelastic gels via indentation and optimization-based inverse finite element analysis. *Journal of the Mechanical Behavior of Biomedical Materials*, vol. 2, no. 4, pp. 355–363. ISSN 17516161.
Available at: `http://dx.doi.org/10.1016/j.jmbbm.2008.12.001`

McGinty, B. (2012). Mooney-rivlin.
Available at: `https://www.continuummechanics.org/mooneyrivlin.html`

Meunier, L., Chagnon, G., Favier, D., Orgéas, L. and Vacher, P. (2008). Mechanical experimental characterisation and numerical modelling of an unfilled silicone rubber. *Polymer Testing*, vol. 27, no. 6, pp. 765–777. ISSN 01429418.

Mooney, M. (1940). A theory of large elastic deformation. *Journal of Applied Physics*, vol. 11, no. 9, pp. 582–592.

MSC Software, C. (2017*a*). *Marc 2017, Volume A: Theory and User Information*. MSC Software Corporation, 4675 MacArthur Court, Suite 900, Newport Beach, CA.

MSC Software, C. (2017*b*). *Marc 2017, Volume B: Element Library*. MSC Software Corporation, 4675 MacArthur Court, Suite 900, Newport Beach, CA.

MSC Software, C. (2019). *Marc and Mentat Release Guide 2019*. MSC Software Corporation, 4675 MacArthur Court, Suite 900, Newport Beach, CA.

Perotti, L.E., Ponnaluri, A.V., Krishnamoorthi, S., Balzani, D., Ennis, D.B. and Klug, W.S. (2017). Method for the unique identification of hyperelastic material properties using full-field measures. Application to the passive myocardium material response. *International Journal for Numerical Methods in Biomedical Engineering*, vol. 33, no. 11, pp. 1–24. ISSN 20407947.

Rivlin, R.S. (1948). Large elastic deformations of isotropic materials. iv. further developments of the general theory. *Philosophical Transactions of the Royal Society of London. Series A, Mathematical and Physical Sciences*, vol. 241, no. 835, pp. 379–397.

Sasso, M., Palmieri, G., Chiappini, G. and Amodio, D. (2008). Characterization of hyperelastic rubber-like materials by biaxial and uniaxial stretching tests based on optical methods. *Polymer Testing*, vol. 27, no. 8, pp. 995–1004. ISSN 01429418.
Available at: http://dx.doi.org/10.1016/j.polymertesting.2008.09.001

Smooth-On (2012 March 2019). Smooth-sil series: Addition cure silicone rubber compounds.
Available at: https://www.smooth-on.com/products/smooth-sil-950/

Tobajas, R., Ibartz, E. and Gracia, L. (2016). A comparative study of hyperelastic constitutive models to characterize the behavior of a polymer used in automotive engines. *Proceedings of 2nd International Electronic Conference on Materials*, p. A002.
Available at: http://sciforum.net/conference/ecm-2/paper/3398

Vanderplaats Research Development, I. (2001). *Design Optimization Tools, User Manual*, version 5.x edn.

Vanderplaats Research & Development Inc. (2001). Design Optimization Tools Users Manual.

Vastmans, J., Fehervary, H., Verbrugghe, P., Verbelen, T., Vanderveken, E., Vander Sloten, J., Treasure, T., Rega, F. and Famaey, N. (2018). Biomechanical evaluation of a personalized external aortic root support applied in the Ross procedure. *Journal of the Mechanical Behavior of Biomedical Materials*, vol. 78, no. November 2017, pp. 164–174. ISSN 18780180.
Available at: https://doi.org/10.1016/j.jmbbm.2017.11.018

Venter, G. (2010). Review of Optimization Techniques. *Encyclopedia of Aerospace Engineering*, pp. 1–12.

Viana, F.A., Venter, G. and Balabanov, V. (2010). An algorithm for fast optimal latin hypercube design of experiments. *International Journal for Numerical Methods in Engineering*, vol. 82, no. 2, pp. 135–156. ISSN 00295981.

Viana, F.A.C. (2013). 0 th World Congress on Structural and Multidisciplinary Optimization Things you wanted to know about the Latin hypercube design and were afraid to ask. pp. 1–9.

Viljoen, D.T. (2018). *Characterising Material Models for Silicone- Rubber using an Inverse Finite Element Model Updating Method*. Master's thesis, Stellenbosch University, Stellenbosch.

Vugrin, K.E. (2005). On the effects of noise on parameter identification optimization problems.
Available at: http://scholar.lib.vt.edu/theses/available/etd-05032005-133146

Wex, C., Arndt, S., Stoll, A., Bruns, C. and Kupriyanova, Y. (2015). Isotropic incompressible hyperelastic models for modelling the mechanical behaviour of biological tissues: A review. *Biomedizinische Technik*, vol. 60, no. 6, pp. 577–592. ISSN 00135585.